submitted to *Geophys. J. Int.*

Structure and evolution of the Australian Plate and underlying upper mantle from waveform tomography with massive datasets

J.I. de Laat[1,2], S. Lebedev[3], N.L. Celli[1], R. Bonadio[1], B. Chagas de Melo[1,2], N. Rawlinson[3]

[1]*Dublin Institute for Advanced Studies, Dublin, Ireland*

[2]*Trinity College Dublin, Dublin, Ireland*

[3]*Department of Earth Sciences, University of Cambridge, Cambridge, United Kingdom*

SUMMARY

We present a new S-wave velocity tomographic model of the upper mantle beneath the Australian Plate and its boundaries that we call *Aus22*. It includes azimuthal anisotropy and was constrained by waveforms from 0.9 million vertical-component seismograms, with the densest data sampling in the hemisphere centred on the Australian continent, using all available data covering this hemisphere. Waveform inversion extracted structural information from surface waves, S- and multiple S-waves and constrained S- and P-wave speeds and S-wave azimuthal anisotropy of the crust and upper mantle, down to the 660-km discontinuity. The model was validated by resolution tests and, for particular locations in Australia with notable differences from previous models, by independent inter-station measurements of surface-wave phase velocities.

Aus22 can be used to constrain the structure and evolution of the Australian Plate and its boundaries in fine detail at the regional scale. Thick, high-velocity (and, by inference, cold) cratonic lithosphere occupies nearly all of western and central Australia but shows

substantial lateral heterogeneity. It extends up to the northern edge of the plate, where it collides with island arcs, without subducting. Diamondiferous kimberlites and lamproite deposits are underlain by cratonic lithosphere, except for the most recent diamondiferous lamproites in the King Leopold Orogen. The rugged eastern boundary of the cratonic lithosphere resolved by the model provides a lithospheric definition of the Tasman Line. Just east of the Tasman Line, an area of intermediate-thick lithosphere is observed in the southern part of the continent. The eastern part of Australia is underlain by thin, warm lithosphere, evidenced by low seismic velocities. All the sites of Cenozoic intraplate volcanism in eastern Australia are located on thin lithosphere. A low-velocity anomaly is present in the mantle transition zone (410-660 km depths) beneath the Lord Howe and Tasmanid hotspots, indicative of anomalously high temperature and consistent with a deep mantle upwelling feeding these hotspots and, possibly, also the East Australia hotspot. High seismic velocities at 200-410 km depth below New Guinea indicate the presence of slab fragments, probably linked to the subduction of the Australian Plate. High seismic velocities are observed in the transition zone below northeast Australia and indicate the presence of subducted lithospheric fragments trapped in the transition zone, possibly parts of the former northern continental margin of Australia.

Key words: Waveform Inversion; Seismic Tomography; Computational Seismology; Cratons; Hotspots; Dynamics of lithosphere and mantle, Australia.

1 INTRODUCTION

The Australian Plate comprises the continental lithosphere of Australia and western Zealandia, surrounded by the oceanic lithosphere of the Indian Ocean, Southern Ocean and Tasman and Coral Seas (Fig. 1). The plate is moving in an NNE direction at a rate of ~7 cm/yr in the hotspot reference frame (DeMets et al. 2010), bounded by the divergent boundary of the Southeast Indian Ridge in the south and various convergent boundaries in the north and east (Fig. 1). In the north, the Australian oceanic lithosphere is subducting at the Java Trench in the north-west and at the New Hebrides Trench in the north-east. At the Banda Arc and in New Guinea Australian continental lithosphere is colliding with the microplates of Southeast Asia to its north. In the east, the Pacific Plate is subducting westward below the Australian Plate at the Tonga-Kermadec-Hikurangi Trench and the Australian Plate is sub-

ducting eastward at the Puysegur Trench (Davey & Smith 1983). The dextral transpressional Alpine Fault in New Zealand acts as the transition between westward subduction to its north and eastward subduction to its south. In the west, the plate is bounded by a diffuse plate boundary with the Indian plate (e.g., Wiens et al. 1985; Gordon et al. 1990), with the two plates sometimes considered as a single, Indo-Australian Plate.

The Australian Plate has a long tectonic history. The Australian continent in its centre comprises three Archean nuclei: The Yilgarn, Pilbara and Gawler cratons. These nuclei comprise some of the oldest rocks on Earth, with dates as early as 4.3 Ga (Mojzsis et al. 2001). The Archean nuclei and the Proterozoic orogenic belts between them are generally divided into three main cratonic blocks: the West Australian Craton, South Australian Craton and North Australian Craton (Fig. 1, Myers et al. (1996); Betts et al. (2002); Fraser et al. (2010)). The cratons are believed to have sutured by 1700 Ma (Huston et al. 2012) and after the breakup of Rodinia at 780 Ma formed a unit that is the current Precambrian core of Australia (Wingate & Giddings 2000). In the Paleozoic the eastern margin of the core became an accretionary margin, with a sequence of subduction complexes on the margin of Gondwana progressively building to the east in the early Paleozoic, creating the Tasmanides (Glen (2005), Fig. 2).

The concept of the 'Tasman Line' has been used to separate the Precambrian west of the Australian continent from the Phanerozoic east. The exact definition and location of this line have varied over the years, based at first only on outcrops (Hill 1951) and in later years on faults and geophysical lineations (Shaw et al. 1995; Gunn et al. 1997; Veevers & Powel 1984; Scheibner & Veevers 2000). The definition of the line has varied from being the location of breakup of the ancient core of Australia from Rodinia to being the westernmost limit of the deformation associated with the Paleozoic fold belts of eastern Australia (Direen & Crawford 2003; Kennett et al. 2004). Direen & Crawford (2003) proposed to drop the term of the Tasman Line due to its varying definitions. Instead, a more gradual transition is proposed (e.g., Direen & Crawford 2003; Fishwick et al. 2008), supported by the presence of Precambrian cratonic fragments that are reworked in the Tasmanide Fold Belt located east of the proposed location of the Tasman Line (Glen 2013; Rosenbaum 2018).

Australia separated from Antarctica during the breakup of Gondwana 80-65 Ma (Cande & Mutter 1982; Mutter et al. 1985), moving NE-NNE as the Southeast Indian Ridge formed and the southern Indian Ocean opened. The Australian plate accelerated northward around 45 Ma and collided in the north with the complex configuration of the microplates of Southeast Asia, a process which continues to the present day. The continent of Zealandia was also attached to Australia and Antarctica as part of Gondwana and separated from Gondwana at 100-80 Ma. It got highly stretched during the two phases of rifting that resulted in the opening of the Tasman Sea (Tulloch et al. 2019). East-dipping

subduction at the New Caledonia Trench started ~60 Ma and ceased around 30 Ma (van de Lagemaat et al. 2018). Around 45-30 Ma the Tonga-Kermadec Trench formed, rolling back towards the east over time and the back-arc, the North Fiji Basin, opened around 27 Ma (van de Lagemaat et al. 2018). Subduction at the Hikurangi Trench started at ~23 Ma (Sutherland 1999) and at the New Hebrides and Puysegur Trenches at ~10 Ma (Gurnis et al. 2019; van de Lagemaat et al. 2018). The complex tectonic evolution of the Australian Plate and its boundaries are still debated, with different regional and global tectonic reconstructions showing substantial differences (Hall (2002); Schellart et al. (2006); Hall (2011); Seton et al. (2012); Metcalfe (2013); Gibbons et al. (2015); Müller et al. (2016); Matthews et al. (2016); Wu et al. (2016); Zahirovic et al. (2016); Müller et al. (2019)) .

Several hotspots are observed in and around the Australian Plate. Hotspots are characterized by anomalously high-temperature upper mantle, topographic swells, and recent (age-progressive) volcanism with isotopic signatures that are different from mid-ocean ridge or andesitic basalts (Sleep 1990; Davies 1988; Courtillot et al. 2003). Hotspots have long been interpreted to be the surface manifestation of mantle plumes (Wilson 1963; Morgan 1971). A mantle plume is defined as a buoyant mass of material rising from the core-mantle boundary to the surface (Morgan 1971). Within the Australian Plate three hotspots have been associated with clear, north-south, age-progressive volcanic tracks: the East Australia, Tasmanid and Lord Howe hotspots (Fig. 2, Wellman & McDougall (1974); Vogt & Conolly (1971); McDougall & Duncan (1988)). Around the Australian Plate the Balleny, Caroline and Samoa hotspots also have been identified by their volcanic chains and have been attributed to underlying mantle plumes (Duncan & Richards 1991; Keating et al. 1984; Koppers et al. 2008). Based on seismic tomography Montelli et al. (2004) proposed additional possible mantle plumes in and around the Australian Plate: The Indian Ocean, Cocos-Keeling and Chatham hotspots (Fig. 1). These hotspots, however, do not show any surface expression.

Non-age progressive intraplate volcanoes are scattered around the Tasman Sea and eastern Australia. These volcanoes have been linked to different processes including hot mantle upwellings and, alternatively, edge-driven convection, shear-driven upwelling and slab flux (e.g., Fishwick & Rawlinson 2012; Davies & Rawlinson 2014; Mather et al. 2020).

Seismic observations can help us to obtain a better understanding of the dynamics and evolution of the Australian Plate and its boundaries. The distribution of seismic velocities in the upper mantle depends largely on temperature, composition and pressure and thus, combined with other geological and geophysical data, can offer essential information on the structure and evolution of the plate. A number of regional tomographic models have been computed for the Australian continent using surface and body waves (Zielhuis & van der Hilst 1996; Simons et al. 1999; Debayle 1999; Debayle & Kennett 2000; Simons et al. 2002; Yoshizawa & Kennett 2004; Fishwick et al. 2005, 2008; Fishwick & Read-

ing 2008; Fichtner et al. 2010; Fishwick & Rawlinson 2012; Kennett et al. 2013; Yoshizawa 2014; Sun & Kennett 2016). They show a seismically fast (and, by inference, thick and cold) lithospheric root below the cratonic region in the west and centre of the Australian continent. The models using regional data, however, tend to lose resolution towards the plate boundaries. Global P- and S-wave models (Schaeffer & Lebedev 2013; Debayle et al. 2016; French & Romanowicz 2014; Ritsema et al. 2011; Amaru 2007; Li et al. 2008; Montelli et al. 2006; Simmons et al. 2012) include the entire Australian Plate, but these models are not optimized for this area and do not provide the highest possible resolution of the Australian lithosphere.

In this paper, we present a new upper mantle S-wave velocity model of the Australian Plate and its boundaries. The model, *Aus22*, is computed using a massive dataset of waveform fits of both global and regional seismograms, with peak data coverage in the hemisphere centred on Australia and reduced coverage elsewhere. The tomographic model reveals i) the lithosphere below Australia and Zealandia, including the fine structure and lateral extent of the Australian cratonic lithosphere, ii) the seismic structure below the hotspots within the region, iii) the subducting lithosphere at the northern and eastern boundaries of the plate and iv) the high-velocity bodies in and above the mantle transition zone (410-660 km depths) below the plate, probably related to subducted lithospheric remnants. In the following sections, we describe our dataset and waveform tomography methods, present and validate the model, compare it to published regional and global models and discuss immediate inferences on the structure, dynamics and evolution of the Australian Plate and underlying mantle.

2 METHODS

2.1 Dataset

The model *Aus22* is created using a hemisphere-focussed global dataset containing 950 thousand vertical-component seismograms, successfully fitted using the Automated Multimode Inversion (AMI) of surface and S- and multiple S-waveforms (Lebedev et al. 2005). The hemisphere is centred at the centre of the Australian continent and covers an area with a 90 degrees radius (Fig. 3). From our global dataset of over 1.7 million traces (an expansion of the data set used by Celli et al. (2020b)), only seismograms with the source, the receiver or both the source and the receiver located within the hemisphere are used to constrain the model. This, therefore, includes seismograms recorded at a station outside the hemisphere from an event within the hemisphere and vice versa. Traces recorded outside the hemisphere from an event located outside the hemisphere are excluded. The data sampling in the other, antipodal hemisphere decreases gradually from its boundaries. It is sparser than in the Australia-centred hemisphere but sufficient to resolve the structure within it accurately, albeit with a

lower resolution. This prevents the structure from one hemisphere from mapping erroneously into the other hemisphere.

The waveform fits for the 950 thousand seismograms are obtained from 26 thousand teleseismic events, recorded at ~9100 permanent and temporary broadband stations located around the world between 1982 and 2018 (Fig. 3). The broadband data were obtained from numerous online data centres, including IRIS (`http://www.iris.edu`), ORFEUS (`http://www.orfeus-eu.org`) and AusPass (urlhttp://auspass.edu.au/). For the full list of online data centres, see the Data Availability Statement (section 7). The waveforms are downloaded through the FDSN (International Federation of Digital Seismograph Networks) Web Service (`https://www.fdsn.org/`) using Obspy (Beyreuther et al. 2010). The earthquake locations and their moment tensors are obtained from the Global CMT catalogue (Dziewonski et al. 1981; Ekström et al. 2012), which contains the source mechanisms of global events with a magnitude over 4.5.

Over 650 stations are situated in and around the Australian Plate, as are over 15 thousand events (Fig. 3). The stations include the permanent ones from the Australian National Seismograph Network (ANSN, `http://www.ga.gov.au`), the Australian Seismometers in Schools, (AuSIS, Balfour et al. (2014)) and the New Zealand National Seismograph Network (GeoNet, Petersen et al. (2011)). The temporary stations include the stations from the BASS (Reading et al. 2013), BILBY (Rawlinson & Kennet 2008), CARPA (Reading & Kennett 2005), KIMBA (Kennett 1998), SKIPPY (van der Hilst et al. 1994), SOC (Fontaine & Kennet 2007) and WACRATON (Kennet 2000) experiments on the Australian continent, the STREWN (Thurber & Townend 2016) array in New Zealand and the MOANA (Collins & Sheehan 2009) array offshore New Zealand. Earthquakes in the region are mainly situated near the boundaries of the Australian Plate, with the majority at the northern and eastern convergent boundaries (Fig. 3).

The data coverage in the area is dense but uneven, both laterally and with depth. The number of paths sampling each model grid node is highest in the north and north-east of the model region and decreases towards the Indian and Southern Ocean in the south-west (Fig. 4). The greatest data sampling, estimated using the sums of the columns of the tomographic problem's sensitivity matrix, is observed around the northern boundary of the Australian Plate at lithospheric depths, decreasing to the lowest values in the Indian and Southern Ocean in the transition zone (Fig. 4). We note, however, that even the model grid nodes with the sparsest coverage are each sampled by over 10 thousand source-station paths, which ensures that the entire region of the model is well constrained.

2.1.1 Quality Checks and Preprocessing

To minimize the errors in the data, extensive quality checks have been performed on the downloaded seismograms. One of these checks involves assessing the correctness of the instrument response information provided by the data centres. The instrument response information specifies how the time series recorded in instrument counts relates to the ground displacement or velocity time series; the response should be removed before inverting the data. When a station gets recalibrated, the instrument response is regenerated. A single station can thus have numerous instrument response files, one for each period between two recalibrations. Incorrect response information can cause errors in the processed seismograms and, thus, in the resulting tomographic model. It is thus important that the correct and most up-to-date instrument response information for that period in time is attached to a downloaded seismogram.

The correctness of the instrument response files was checked by comparing the response files attached to data downloaded from different data repositories. If the response information is inconsistent, the most up-to-date response file for that period in time was used for the instrument response correction.

This method to trace and correct response files is, however, only possible for data that can be downloaded from multiple data repositories. If data from a certain station is only available through one data centre, an outdated response file will remain unnoticed. Instrument response files can also be updated back in time at the data centres. This requires ongoing checks on the most up-to-date response files for the time period in which the seismogram is recorded, of the data available through the data centres.

Before the instrument correction is applied with the most up-to-date instrument response information for the time period in which the seismogram is recorded, the seismograms are checked for fragmentation and clipping—which, if detected, cause the seismogram to be discarded. If the seismogram passes the quality checks, it is detrended and downsampled to 1 sample per second and saved as a displacement seismogram. Additionally, the horizontal components are rotated to the radial and transverse direction, relative to the event. In this study, however, only the vertical displacement seismograms are used in the tomographic inversion.

2.2 Inversion Procedure

The inversion procedure is split into three steps. The first step is the inversion of the preprocessed seismograms using AMI (Automated Multimode Inversion, Lebedev & Nolet (2003); Lebedev et al. (2005)), which fits surface, S- and multiple S-waves on the seismograms with synthetic waveforms. The output of AMI is a set of independent linear equations (Nolet 1990) that describe the 1-D average

perturbations in P- and S- wave velocities within the sensitivity volumes between the source and the receiver with respect to a 3D reference model (Lebedev & Van Der Hilst 2008). The 3D reference model assigns one of 664 types of 1D velocity profiles to every point at the surface. The reference profiles have a varying crustal structure, according to CRUST2.0 (Bassin 2000), smoothed at cell boundaries and with a depth-dependent seismic velocity correction that brings it towards the global average, and a global average profile in the mantle, according to the global tomography model of Lebedev & Van Der Hilst (2008). Both the crustal and mantle structure is inverted for. The sensitivity volumes between the source and the receiver are bounded by a $\pi/2$ Fresnel zone, computed for a frequency in the middle of the frequency band of the waveform under consideration. The approximate sensitivity volumes have a trapezoidal shape in the cross-section perpendicular to the path, with a constant weight in the middle portion and a gradual decrease to zero at the sides; the integral over a path-normal section through the kernel is constant (see Figure 6 and 7 in Lebedev & Van Der Hilst (2008)). The linear equations produced by the waveform inversion define 1-D average velocity perturbations to the 3D reference structure within the sensitivity volumes. The combined sensitivity of the different wave types provides information on the structure from the crust down to the transition zone and the shallow lower mantle below it.

The second step of the imaging process is the tomographic inversion for 3-D seismic structures. Here the equations yielded by waveform inversion of all the seismograms are combined into one large linear system. This tomographic inversion uses LSQR to solve for the 3-D distribution of P- and S-wave velocity deviations from the 3-D reference model (same as used for AMI) and azimuthal anisotropy of the S-wave velocity (Lebedev & Van Der Hilst 2008). The model is parametrised using a global triangular grid with an interknot spacing of approximately 150 km. The integration over the sensitivity volumes uses a 25 km, co-registered integration grid. Radially, the model is parametrised using a fixed set of 18 and 10 triangular basis functions for S- and P- waves, respectively, their middle points spanning from 7 to 1008 km depth. The depths of the discontinuities at 410 and 660 are fixed and seismic velocities above and below them are parametrised using two independent half triangles, above and below. The sensitivity area of each seismogram is the same as used in AMI; the radial sensitivity distribution reflects the combined sensitivities of the waves in all the time-frequency windows for which the signal was inverted for (Lebedev & Van Der Hilst 2008). To minimize the effect of non-uniform coverage, all paths are weighted, with greater weight given to less redundant information (Lebedev & Van Der Hilst 2008).

Regularization is applied by lateral Laplacian smoothing, radial gradient damping and minimal norm damping. A proper balance has to be found between the amount of detail the model exhibits and its accuracy (e.g., Backus & Gilbert 1970; Bonadio et al. 2021). When a model is too smooth,

important details are lost, whereas a model that is too rough will be dominated by errors. Limited norm damping is applied to penalize large amplitudes and stabilize the inversion. To take the variations of the data sampling with depth into account (Fig. 4), the smoothing and damping parameters vary with depth (Lebedev & Van Der Hilst 2008; Celli et al. 2020b). Although there are lateral variabilities in the data coverage, we use a constant smoothing and damping parameter laterally. At places with a denser data coverage, however, the same smoothing coefficient will result in less smoothing and a more detailed structure. Generally, the data sampling is greater at lithospheric depths than at deeper levels and, thus, the norm damping coefficients decrease with increasing depth. Perturbations in P-wave and S-wave velocities are not coupled rigidly but the difference between them is penalised (Lebedev & Van Der Hilst 2008). This amounts to flexible coupling, with differences between V_P and V_S anomalies generally small and appearing only when required by the data. As the S-wave velocity heterogeneity is constrained better than the P-wave velocity heterogeneity, we shall only focus on the S-wave velocity heterogeneity when discussing the model in this paper.

The third part of the tomographic inversion scheme is the selection of the most mutually consistent data using an automatic and manual posterior outlier analysis. The automated outlier analysis is done by comparing the synthetic data computed from a first-iteration model to the real data and discarding the seismograms with the largest misfit between the two. The subset remaining is then re-inverted to produce an updated model. With this procedure, the most mutually consistent data are selected and the data with the highest likelihood of large errors are removed. The manual outlier analysis removes data from stations or earthquakes that create patterns identified as suspicious (see section 4.3). Our final model is computed using 622 thousand most mutually consistent waveform fits.

It is important to note that although the tomographic inversion is performed globally, the new model is regional. First, we made a particular effort to ensure that the dataset includes all the available waveforms from the hemisphere around the Australian Plate. Second, the data coverage in the antipodal hemisphere is reduced, by design, to decrease the size of the problem. Third, the regularization applied is optimized specifically for the Australian Plate. Finally, the manual outlier analysis is only applied within the research area (problematic stations outside the area, for example, may not be recognised and removed). This model is thus created and optimized for the area of the Australian Plate and its surroundings, as presented in this paper.

3 THE MODEL

3.1 Model Description

Aus22 is an azimuthally anisotropic model of the upper mantle, down to 660 km depth, beneath the region that includes the Australian Plate and its boundaries. The model contains isotropic S-wave velocity anomalies relative to our reference model, which is 3-D in the crust and 1-D in the mantle (Figs 5 and 7), and S-wave azimuthal anisotropy (Fig. 8).

The crustal structure of the Australian plate is included in *Aus22*, as it has been inverted for (see section 2). Fig. 6 shows a map view of the absolute values of Vs in *Aus22* at 20 km depth. The values beneath Australia are similar to those at the same depth in the model AuSREM, which used various complementary lines of evidence (e.g. receiver functions, seismic reflection and refraction studies) on the crustal structure (Salmon et al. 2013a). Beneath Australia's boundaries and surrounding areas, *Aus22* also captures the continent-ocean transitions, thanks to its data sampling of the entire Australian Plate.

The largest S-velocity anomalies in the upper mantle ($>\mathbf{5\%}$) are observed below the cratonic part of Australia, which shows a thick cratonic root down to >200 km depth. High seismic velocities are also observed at the convergent northern and eastern boundaries of the plate, where cold lithospheric slabs are descending into the mantle. Low seismic velocities are observed beneath the Southeast Indian Ridge, volcanic arcs and back-arc basins and areas of intra-plate volcanism.

Deviations in the S-wave seismic velocity are primarily due to variations in temperature but are also affected by composition, water and partial melt (Masters et al. 2000; Karato 1993; Walsh 1969; Sobolev et al. 1996). Generally, the effect of composition is smaller (Sobolev et al. 1996), but it may be significant in a number of cases. In the uppermost mantle within the cratonic lithosphere, for example, seismic velocities are usually lower than in the deeper lithosphere, something that cannot be explained by variations in temperature, which increases with depth, but could be explained, instead, by the effects of metasomatism (Eeken et al. 2018), composition-affected phase transformations (Lebedev et al. 2009; Ravenna et al. 2018) or both. The origin of the very high seismic velocities in deeper (100-150 km) cratonic lithosphere is also debated, to the extent that the presence of substantial amounts of diamond and eclogite was proposed to account for it (Garber et al. 2018). Water and partial melt decrease seismic velocities and have a significant effect on the seismic structure below back-arc basins and possibly elsewhere (e.g., Karato & Jung 1998; Karato 2012; Chantel et al. 2016). The degree of partial melt and its effect on seismic velocities decrease, in most locations, below 90 km (Fullea et al. 2021). Overall, temperature is the dominant factor responsible for the observed seismic velocity anomalies in *Aus22* (Lebedev & Nolet 2003; Celli et al. 2020b); the high seismic velocities in *Aus22*

(blue-purple) primarily reflect lower temperatures, whereas low seismic velocities (yellow-red-black) indicate higher temperatures, with probable partial melting where the velocities are the lowest and with the likely influence of high water content in subduction zones.

3.2 Comparison with Other Tomographic Models

We compare *Aus22* to three recent regional S-wave velocity models of the Australian continent, five global S-wave models and four global P-wave models. With different techniques and different data being used to generate these models, some differences between the models are to be expected. Fig. 9 shows the velocity anomalies at 150 km depth according to the three regional models and Fig. 10 shows the velocity anomalies at 150 and 450 km depth according to the eight global models. A full comparison between the models, including maps at other depths, is given in Appendix A.

The three regional models are FR2012 (Fishwick & Rawlinson 2012), AuSREM (Kennett et al. 2013) and CSEM (Fichtner et al. 2010). FR2012 is a Rayleigh wave model where path-specific 1-D shear wave speed depth profiles are combined in a tomographic inversion to obtain a 3-D model of the velocity structure (Fishwick & Rawlinson 2012). AuSREM is an S-wave model whose mantle component is constrained by surface wave tomography and body wave data (Kennett et al. 2013). CSEM is a radially anisotropic waveform tomography model, constructed using spectral-element simulations and adjoint techniques (Fichtner et al. 2010).

The previous regional tomographic models and *Aus22* are similar in the amplitude and location of the lithospheric seismic velocity anomalies at larger scales but vary in their detailed structure. All models show high seismic velocities at lithospheric depths below the central and western parts of Australia. Beneath the eastern part of the continent, all models show negative seismic velocity anomalies. In the three previous regional models, however, the high seismic velocities decrease at the northern coast of Australia, whereas in *Aus22* the high seismic velocities extend beneath the Timor Sea and the Arafura Sea towards the northern boundary of the Australian Plate. Additionally, the transition to low seismic velocities towards the east varies in its location in different models. In *Aus22* the seismic velocities decrease further west in the south of the continent and further east in the north of the continent compared to the other three models. Finally, the amplitude of the negative seismic velocities observed along the eastern margin of the continent and in the Tasman Sea varies between the models. *Aus22* shows a number of prominent areas of negative seismic velocities at 80-110 km depth (Fig. 5), e.g. below the Bass Strait (separating Tasmania from the Australian mainland), while these are not observed by the other regional models. The greater detail in *Aus22* near the boundaries of the continent is largely thanks to its increased data sampling, given by the combination of the data from the stations in Australia and all other stations in the hemisphere around it.

The five global S-wave models are SL2013sv (Schaeffer & Lebedev 2013), 3D2016_09Sv (Debayle et al. 2016), SEMum2 (French & Romanowicz 2014), CAM2016Vsv **(Priestley et al. 2018)** and (Ritsema et al. 2011). SL2013sv is a predecessor of *Aus22*, computed using the same methodology but with fewer seismograms (750 thousand globally), only 6 stations in Australia, and a coarser grid spacing (~280 km, Schaeffer & Lebedev (2013). 3D2016_09Sv is an upper-mantle S-wave model based on global Rayleigh wave recordings (Debayle et al. 2016). SEMum2 is a global radially anisotropic S-wave velocity model (French & Romanowicz 2014). S40RTS is an isotropic, whole-mantle, S-wave velocity model constrained by Rayleigh wave phase velocities, teleseismic body-wave traveltime and normal-mode splitting function measurements (Ritsema et al. 2011).

The large-scale features seen in *Aus22* can also be observed in the global S-wave models, but their resolution is substantially lower. All models show the high velocities below the central and western parts of the Australian continent and lower velocities in the surrounding oceans, but *Aus22* resolves substantially more detail. Additionally, *Aus22* resolves high-velocity anomalies below the trenches at the Australian plate boundaries, which are absent or poorly visible in the previous S-wave models.

The four global teleseismic P-wave models are UU-P07 (Amaru 2007), MITP08 (Li et al. 2008), PRI-P05 (Montelli et al. 2006) and LLNL_G3Dv3 (Simmons et al. 2012). UU-P07 was computed using P-wave travel time data and a global surface-wave model as a reference, which gives it a more realistic lithospheric structure than most teleseismic body-wave models (Amaru 2007). UU-P07 and MITP08 (Li et al. 2008) both use short-period P-wave arrival data. PRI-P05 is a finite-frequency P-wave model based on arrival times of P-waves at two different dominant periods (1 and 20s, Montelli et al. (2006)). LLNL_G3Dv3 is a global P-wave velocity model computed with 3-D ray tracing (Simmons et al. 2012).

The global P-wave models resolve numerous fragments of subducted lithospheric slabs and are particularly interesting to compare to *Aus22* along the trenches and in the transition zone. These models have poor resolution, however, at lithospheric depths. The P-wave models show high-velocity anomalies below the subduction zones at the northern and eastern boundaries of the plate, similar to *Aus22*. In the transition zone, the resolution of the P-wave models becomes more uniform beneath the continent and surrounding oceans. Notable differences between all the models illustrate that resolving the deep upper mantle structure remains an outstanding challenge. Several prominent features, however, can be observed consistently in the transition zone in *Aus22* and in other models, including high seismic velocities below north-east Australia and low seismic velocities below the central Tasman Sea.

4 VALIDATION OF THE MODEL

Going beyond standard resolution testing, we validate the structure of selected lithospheric features of particular significance by making independent, interstation measurements of surface-wave phase velocities. We also test and validate *Aus22* using a series of resolution tests for the isotropic and anisotropic components of the model, performed with the same regularization as the inversion of real data. Further validation is provided by the close correspondence, in many cases, of deep shear-wave speed boundaries in the model with known geological and geographical features at the surface.

4.1 Spike Test

Spike tests illustrate the spreading of a narrow test anomaly, both laterally and vertically. They can help us to tune the accurate regularization of the model (e.g., Celli et al. 2020b). Spike tests use synthetic P- and S-wave anomalies at certain depth nodes in the model and the tomographic inversion of the data corresponding to these synthetic anomalies. The output is compared to the input and illustrates the resolution yielded by the data sampling at different locations and depths in the model.

Fig. 11 shows the test input and output for two spikes, at 110 and 585 km depth, one located in a well-covered area (northern Australia) and the other one located in a more sparsely sampled area (Tasman Sea, see Fig. 4 for coverage). The output of the resolution test (Fig. 11) illustrates the difference in resolution between the two depths. At 110 km depth, the output closely matches the input, with a slightly higher amplitude resolved in the area of higher coverage. At 585 km depth, the spike is broadened substantially more, both vertically and horizontally. The amplitude varies significantly between the well and poorly covered region at 585 km depth, giving a more E-W oriented low amplitude output in the Tasman Sea and a high amplitude circular output in northern Australia.

4.2 Anisotropy Test

Azimuthal anisotropy is normally a less robust component of a tomographic model compared to the isotropic average seismic velocities. Isotropic heterogeneity can leak into anisotropy and cause artefacts (e.g., Darbyshire & Lebedev 2009). The 90-degree test (e.g., Endrun et al. 2011) is an effective means of verifying whether the anisotropy in the model is robust or possibly affected by the leakage. In this test, the input test model is the actual tomographic model, with the isotropic component left as is but with the fast axis of anisotropy rotated by 90 degrees. The output of the test inversion is then compared to the input. If the fast-axis of azimuthal anisotropy does not match the 90-degree-rotated input but, instead, is changed back towards its original orientation, this implies that anisotropy in the model in this location is likely to be influenced by the leakage from the isotropic component of the

model, and is unreliable. This lack of reliability does not necessarily mean that the fast direction in the model is wrong (different from that in the Earth), but that it may be influenced by the isotropic component of the model.

We used a threshold of 25 degrees, meaning that if the fast directions in the output differed by more than 25 degrees from the input, the anisotropy was deemed unreliable. In Fig. 8 the anisotropy result that passed the 90-degree test is marked in white, while the unreliable anisotropy results are marked in grey. Note that the fast-propagation direction of anisotropy is usually difficult to determine where its amplitude is small. In many cases, the grey anisotropy markings on our maps are simply an indication of low amplitude of anisotropy, especially at shallower depth, where the recovery of anisotropy is generally good.

4.3 Testing with independent measurements: SW Kimberley Block and the station FITZ

In the southwest Kimberley block (see Fig. 2), a significant difference can be seen in seismic velocity at lithospheric depth between the various regional tomographic models of Australia (Fig. 9). FR2012 (Fishwick & Rawlinson 2012) images a region of high seismic velocities while CSEM (Fichtner et al. 2010) images significantly lower seismic velocities. We found that the seismic velocity below the southwest Kimberley block yielded by our tomographic inversions depends on whether we include or exclude the data of one particular station: FITZ. A high seismic velocity structure is present when including the station, whereas a significantly lower seismic velocity is seen when excluding the station (top figures in Fig. 12). This prompts the question of whether the high seismic velocity is an artefact caused by this station's data, possibly also responsible for the high seismic velocity seen in this area in FR2012.

To test if the high seismic velocity structure is indeed an artefact, we measured the phase-velocity below the region using an independent, interstation method. The interstation method is a classical method to calculate phase velocities between a pair of stations. The method was introduced by Sato (1955) and used widely since. The implementation of the method by Meier et al. (2004) enabled measurements in a very broad period range **(Zhang et al. 2009; El-Sharkawy et al. 2020)**, with Soomro et al. (2016) developing an automated version, and Bonadio et al. (2018) adding data-based determination of a phase-velocity reference model. For this test, we followed **Bonadio et al. (2018, 2021)** and cross-correlated the fundamental mode Rayleigh waves in teleseismic earthquake recordings **(same seismograms as used in the waveform inversion, see section 2)** to calculate the phase velocities for each pair of stations.

In this particular application, we calculated a phase-velocity curve averaging across the footprint of the array of stations surrounding the station FITZ (Fig. 12, middle). The array consists of 13 sta-

tions, and the average phase-velocity curve was computed using 266 phase-velocity curves from 26 station pairs. The result is shown as the black line in Fig. 12 (bottom). The red and green lines in the bottom frame of Fig. 12 show the phase-velocity curves obtained from our tomographic inversion at the location of station FITZ when including and excluding the data from station FITZ, respectively. The comparison of the three profiles shows that the phase-velocity curve according to the tomographic inversion when excluding the data from station FITZ closely follows the phase-velocity obtained from the interstation method, whereas the phase-velocity curve obtained when including the FITZ data is too fast. We thus conclude that the seismic anomaly near station FITZ is an artefact caused by the FITZ data and not a true seismic structure. The data from the station FITZ could be causing bias in tomographic models due to a number of possible reasons, e.g., wrong instrument response information, a timing issue or local site conditions. The data from station FITZ has thus been excluded from the tomographic inversion that yielded *Aus22*.

4.4 Testing with independent measurements: the Gulf of Carpentaria high-velocity anomaly

Around the Gulf of Carpentaria, located in the northeast of the North Australian Craton (Fig. 2), the lithospheric seismic velocities imaged by *Aus22* differ significantly from the structure in some of the previous tomographic models (Fig. 9). *Aus22* shows high velocities at 80-150 km depth characteristic of cratonic lithosphere, with a sharp transition to low seismic velocities to the east, below the Cape York Peninsula (Fig. 5). A similar structure was seen in early waveform tomography of the area (Lebedev et al. 1997), but recent tomographic models of Australia show relatively low seismic velocities at lithospheric depths beneath the Gulf of Carpentaria, with a gradual eastward decrease in seismic velocities below the Cape York Peninsula (Fig. 9).

To test if the Gulf of Carpentaria is indeed underlain by a high-velocity lithosphere, we used the independent, interstation method (see section 4.3) to measure phase velocities between a pair of stations at the boundaries of the area (COEN and WRAP, top frame of Fig. 13). Over 500 phase-velocity curves measured from single-event seismogram pairs were used to compute the average phase-velocity curve. This interstation phase-velocity curve shows high velocities that are in close agreement with the curves computed from *Aus22* at different nodes in the Gulf of Carpentaria area (Fig. 13). These phase velocities are much higher than those beneath the eastern Australia lithosphere to the east. This result confirms that the Gulf of Carpentaria is underlain by high seismic velocities, and by inference, cold, thick lithosphere.

5 DISCUSSION

5.1 The Australian Lithosphere

Aus22 presents a detailed image of the lithosphere below the Australian continent (Fig. 9), providing new insights into its structure, dynamics and evolution. *Aus22* resolves finer detail, compared to previous models, within the continent and in particular near its margins, thanks to the dense data sampling of the entire Australian Plate and the regions around it, given by our large dataset. The model is thus well suited to map accurately the lateral extent and the boundaries of the Australian cratonic lithosphere. In the following paragraphs, we discuss the structures observed below the Australian continent and their relationship to the overlying geology.

5.1.1 Cratonic Lithosphere

The seismic velocity structure of the Australian cratonic lithosphere shows significant lateral variability. At 80 km depth, the highest seismic velocities are observed roughly beneath the North, South and West Australian Cratons, with the highest seismic velocities observed below the West Australian Craton. Within the South Australian Craton, two small peaks in velocity are observed below the Gawler Craton and the Curnamona Block. Below the North Australian Craton a more uniform high-velocity anomaly is observed, continuing northward offshore, up to the northern boundary of the plate.

At 110 km depth, a single block of high seismic velocity is observed to extend from the South to the West Australian Craton to the southern boundary of the North Australian Craton, covering both the Musgrave Orogen and Amadeus Basin (Fig. 14). This high-velocity block also stands out at 150 km depth but loses clarity at 200 km depth, with a slight positive velocity peak remaining below the Musgrave Orogen down to 260 km depth. Below the Pilbara Craton, the amplitude of the S-velocity anomaly decreases already at 150 km depth. The seismic velocities of the lithosphere below parts of the North Australian Craton are lower than below the southwestern block at 110-150 km depth. The lowest velocities are imaged in the southern part of the North Australian Craton, underlying the Arunta Block, the Kimberley Block and the King Leopold Orogen. The high-velocity anomaly decreases at 200 km depth beneath most of the North Australian Craton, especially below its offshore part.

To get a better understanding of the lateral extent of the cratonic mantle lithosphere, we computed its outline (Fig. 15). Here, we define the cratonic lithosphere of the Australian Plate as any region with an S-velocity anomaly exceeding **5%** anywhere between 110 and 150 km depth (Celli et al. 2020b). **A 5% anomaly threshold isolates shear-wave velocities characteristic of cratonic lithosphere according to global tomography (Schaeffer & Lebedev 2015), to temperature estimates from samples from cratonic mantle lithosphere (McKenzie et al. 2005) and to the conversion of the**

temperatures to seismic velocities (Agius & Lebedev 2013). In order to determine whether or not the characteristically cold, thick cratonic lithosphere is present, the 5% Vs anomaly is an effective threshold. According to this seismic criterion, cratonic mantle lithosphere underlies almost all of the central and western parts of Australia. Offshore in the north, the cratonic lithosphere extends towards the Timor and the Arafura Sea and terminates at the northern plate boundary (Fig. 15), where the Australian continental lithosphere collides with the Southeast Asia-Western Pacific microplates. In the south and west of the continent, the cratonic mantle lithosphere has a boundary within the Yilgarn and Gawler Cratons, leaving the Albany-Fraser Orogen and the southern tip of the Gawler and southern and western edge of the Yilgarn craton without a cratonic mantle lithosphere. In the southeast, the cratonic lithosphere extends below the Curnamona Block. This agrees with the regional surface wave tomography model of Rawlinson et al. (2016) and supports an Archean age for this province and it possible links with the Gawler Craton, as put forward by Page et al. (2005) and Hand et al. (2008). In the northeast, the cratonic lithosphere terminates west of the Georgetown Inlier, which itself is underlain by low seismic anomalies at lithospheric depths, indicating the presence of a warm, thin lithosphere below the Inlier (Fig. 16).

The presence of cratonic lithosphere below the Gulf of Carpentaria (as verified by the interstation method, see section 4.4), supports the hypothesis of a cratonic basement offshore northern Australia (Connors & Pryer 2018). The basement underlying the Gulf of Carpentaria is known as the Arnhem Block and has been interpreted as a submerged continuation of the Arnhem Province, located east of the McArthur Basin (Fig. 2). The Arnhem Block has been interpreted as a craton, based on its magnetic and gravity response (Connors & Pryer 2018). Previous regional models of Australia (see figure 9) do not image high seismic velocities below Arnhem, putting in doubt the cratonic origin of the basement. The tomographic model of southeast Asia of Zenonos et al. (2019) agrees better with *Aus22*, showing positive V_S velocities and negative V_P/V_S velocities below the region, implying the presence of a thick, cold cratonic lithosphere below the region. With the new tomography of *Aus22* and the independent measurements of the interstation method, we can now verify the cratonic origin of the Arnhem Block, supporting the magnetic and gravity measurements of the area (Connors & Pryer 2018).

The absence of cratonic lithosphere at the southern and western margins of the continent, where crustal Archean cratonic rocks are documented at the surface (Fig. 14), may be linked to the rifting history of these margins. Rifting can cause significant cratonic erosion (Wenker & Beaumont 2018). The separation of Australia and Antarctica ~100-80 Ma (Ball et al. 2013) could be accompanied by erosion of the mantle lithosphere beneath the southern margins of the Yilgarn and Gawler cratons, and the separation of Australia and India ~150 Ma (Gibbons et al. 2012) could be responsible for the

absence of a cratonic root below the western edge of the Yilgarn Craton. Alternatively, the mantle lithosphere beneath these craton margins may have been eroded in earlier or later geodynamic events.

The absence of cratonic mantle lithosphere below the Georgetown Inlier is particularly notable. The inlier is dated at ~1710 Ma (Black et al. 2005) and is the easternmost province of the North Australian Craton (Cawood & Korsch 2008). *Aus22* shows that the Georgetown Inlier is underlain by low seismic velocities, implying a thin, warm lithosphere (Fig. 14) instead of a thick, cold, cratonic lithosphere as imaged below the rest of the North Australian Craton to its west. The absence of cratonic lithosphere below the Inlier is in general agreement with previous tomographic models (Fig. 9, (Simons et al. 1999; Fishwick et al. 2008)). In *Aus22*, however, the edge of the cratonic lithosphere is located further east than imaged previously (Fig. 9), with cratonic lithosphere underlying the Gulf of Carpentaria (verified by the interstation method, see section 4.4). Cratonic erosion has been suggested to explain the absence of cratonic lithosphere below the Georgetown Inlier (Fishwick et al. 2008). Based on previous tomography models, however, this would require a significant area of cratonic lithosphere to be eroded away. The more eastward extent of the cratonic lithosphere in *Aus22* implies that erosion of a smaller area of cratonic lithosphere is necessary to obtain the current lithospheric state.

An event that could have caused the cratonic erosion below the Georgetown Inlier is the rifting of the inlier. An episode of rifting has been proposed by Salmon et al. (2013b) based on seismic reflection data of the inlier. Similar to the southern and western boundary of Australia's cratonic lithosphere, rifting could have caused the removal of the lithospheric root below the Inlier. This explanation is supported by the similarity of the boundary of the cratonic lithosphere east of the Georgetown Inlier to that of the southern and eastern boundary of the cratonic lithosphere. These three boundaries are all characterized by a roughly vertical steep lateral velocity gradient at 110-150 km depth (Fig. 5, cross-section 2-4 in Fig. 7), while the other boundaries of the cratonic lithosphere are more gradual. Based on tomography alone, however, we cannot exclude the possibility that the cratonic boundary has been in place since the formation of the cratonic lithosphere billions of years ago.

Cratonic lithosphere is also absent below the southwestern part of the Kimberley Block and below the adjacent King Leopold Orogen. In contrast to the Georgetown Inlier, this area is still underlain by relatively thick lithosphere, but it is notably warmer and thinner, according to our tomography, than beneath the neighbouring cratonic blocks. A similar decrease in velocity is seen below this area in AuSREM (Kennett et al. 2013) and CSEM (Fichtner et al. 2010), although in those models the thinner lithosphere is located further to the southwest. By contrast, FR2012 (Fishwick & Rawlinson 2012) shows a peak in S-wave velocity anomaly at this location. Our tests, however, suggest that this may be an artefact caused by the data from the station FITZ and should not be interpreted as cratonic

lithosphere (see section 4.3). The absence of cratonic lithosphere below the Kimberley Block and King Leopold Orogen is remarkable as it hosts the most recent diamondiferous lamproites on Earth (20 Ma, McInnes et al. (2012)), generally linked to cratonic lithosphere, and will be discussed further in section 5.4.

5.1.2 The Tasman Line

The Tasman Line (Fig. 17) was defined by Hill (1951) as the "boundary line between the craton and geosyncline in early Palaeozoic times" but has also been viewed as the line of the breakup of Rodinia (e.g., Scheibner & Veevers 2000; Gunn et al. 1997) and the westernmost limit of the deformation associated with the Paleozoic fold belts of eastern Australia (e.g., Veevers & Powel 1984). While Hill (1951) only based the location of the line on geological outcrops, later studies also used fault systems, magnetic lineaments and gravity lineaments to define the location of the line (e.g., Gunn et al. 1997). A thorough comparison of the various definitions and locations of the line was presented by Direen & Crawford (2003), who then proposed to abandon the concept of the Tasman Line altogether due to the inconsistency of its definitions. Later, seismic reflection profile studies and geological models were used to refine the location of the margin between the Tasmanides in the east and the cratonic core of Australia in the west (e.g., Cayley 2011; Moresi et al. 2014).

Both regional and global tomography models display a strong contrast in seismic velocity between the high velocities of central-west Australia's cratonic lithosphere and the lower velocities of eastern Australia's lithosphere (Fig. 9). While in some models this transition is sharp, other models show a more gradual decrease. In *Aus22*, a sharp transition in seismic velocity is present, marking the eastern margin of the cratonic lithosphere (Fig. 17). This sharp velocity transition in the lithosphere can be viewed as the 'lithospheric' Tasman Line, marking the current eastern boundary of Australia's cratonic mantle lithosphere. A similar lithospheric boundary has been defined by Fishwick et al. (2008), who defined multiple steps in lithospheric thickness from west to east Australia (see section 5.1.3). The high resolution of *Aus22* results in an improved location of the lithospheric Tasman Line. This lithospheric boundary can help us better understand the tectonic makeup of the continent and may also be important for natural resource assessment and exploration (Hoggard et al. 2020).

The location of the 'lithospheric' Tasman Line, as based on the tomography of *Aus22*, is fairly similar to the geologically defined locations of the Tasman Line but shows well-resolved differences (Fig. 17). In the south of the continent, at the eastern margin of the South Australian Craton, the 'crustal' Tasman Lines closely match the eastern boundary of the cratonic lithosphere, curving around the easternmost Proterozoic outcrop of the Williyama Province. The closest match is with the line determined by Veevers & Powel (1984). We note, however, that Veevers & Powel (1984) postulate

that the Tasman Line continues south towards Tasmania, based on the surface geology of Tasmania, whereas the cratonic lithosphere does not extend beyond the southern boundary of the South Australian Craton, as shown by *Aus22*.

In the north, the eastern margin of the cratonic lithosphere is located to the west of the 'crustal' Tasman Lines, as the Georgetown Inlier, in particular, is not currently underlain by cratonic lithosphere (see section 5.1.1). Compared to previous tomographic models (Fig. 9), however, the eastern boundary of the cratonic lithosphere mapped by *Aus22* is further east and in closer proximity to the geologically defined Tasman Lines; in *Aus22* the Gulf of Carpentaria is underlain by high seismic velocities at lithospheric depths (verified by the independent interstation method, see section 4.4), while in previous models it is not. To the north of the Cape York Peninsula, where all the crustal definitions of the Tasman Lines terminate, our tomography maps image the eastern margin of the cratonic lithosphere, as it extends northward up to the Central Range orogeny of New Guinea.

The lithospheric Tasman Line as defined by *Aus22* presents a lithosphere-scale definition of this boundary that is clear and complete in terms of its north-south extent. It presents the current boundary between cratonic and non-cratonic lithosphere that stretches from New Guinea in the north to Broken Hill and Gawler Craton in the south.

5.1.3 East Australia

The eastern part of Australia can be divided into two portions based on lithospheric thickness: 1) the intermediate lithosphere, which shows intermediate seismic velocities and, by inference, intermediate lithospheric thickness and temperature and 2) the Phanerozoic lithosphere, which shows negative S-velocity anomalies in the entire lithosphere-asthenosphere depth range and is, thus, characterised by thin, warm lithosphere (Fig. 15). We define the intermediate lithosphere areas as those where the S-velocity anomaly is in the 1–**5%** range everywhere between 110 and 150 km depth and the Phanerozoic lithosphere areas as those where the S-wave velocity anomaly does not exceed 1% anywhere between 110 and 150 km depth. The transition from cratonic (dVs$>5\%$) to Phanerozoic (dVs$<1\%$) lithosphere is sharp in the north of the continent, and no intermediate lithosphere is observed between the two. In the south, the intermediate lithosphere block is the widest in the east-central part of the continent, below the Tasmanides (Fig. 1), and narrows further south (Fig. 15).

The Tasmanides is a collection of subduction-related orogens of Cambrian to Triassic age (~550-220 Ma, Glen (2005)). The Tasmanides have been seen as an accretionary orogen (Coney 1992; Cawood & Buchan 2007; Glen 2013), but their tectonic evolution is still debated, due to limited outcrop data caused by a thick sediment cover (Rosenbaum 2018). Based on evidence of reworked Proterozoic rocks in various outcrops in the Tasmanides, a Proterozoic basement has been proposed below

the northern and southwestern part of the Tasmanides(Cayley et al. 2002; Glen 2013; Rosenbaum 2018), but the basement age below most of the Tasmanides remains unknown. From *Aus22* we can infer that the current lithosphere below the Tasmanides is not cratonic (Fig. 14). This implies that if cratonic lithosphere ever existed below the Tasmanides, it has been lost due to lithospheric erosion (e.g., Menzies et al. 1993; Celli et al. 2020a).

Our mapping of the progressive lithospheric thinning towards the east is generally consistent with the stepwise eastward thinning of the lithosphere proposed by Fishwick et al. (2008), based on the tomography of Fishwick & Reading (2008), while also adding sharper regional detail. In both models, the intermediate lithosphere is absent in the north and is the broadest in the centre-east of the continent. The thin Phanerozoic lithosphere stretches north-south along the entire eastern margin of the continent in both models. Among the differences, *Aus22* shows one single block of intermediate lithosphere, compared to two blocks with different lithospheric thicknesses postulated by Fishwick et al. (2008), implying a less gradual decrease in lithospheric thickness towards the east, with only two major steps. The accuracy of *Aus22* is corroborated by independent data in the east of Australia: all Cenozoic volcanism locations are underlain by thin Phanerozoic lithosphere (Fig. 16), whereas in Fishwick et al. (2008) some of these would map, counter-intuitively, on relatively thick, intermediate lithosphere. The boundary between the cratonic and non-cratonic lithosphere defined by *Aus22* is located in closer proximity, compared to previous tomographic models, to the location of the geologically defined Tasman Line (see section 5.1.2).

5.2 Zealandia

The deep structure of the continent of Zealandia is still poorly known. Zealandia is 94% submerged below sea level and has only recently been defined as a continent, rather than a collection of continental islands, fragments and slices (Mortimer et al. 2017). The crustal thickness of the continent varies between 20 km below the Lord Howe Rise and Norfolk Ridge (Fig. 18) and 9 km thick below the New Caledonia Trough (Gallais et al. 2019; Klingelhoefer et al. 2007). The New Caledonia Trough has been interpreted as a failed rift system and the thin crust has been attributed to delamination of the underlying lithosphere during the subduction initiation at the Australian-Pacific boundary in the Eocene (Sutherland et al. 2010). Due to very limited outcrop, much of the geology and evolution of the continent remains to be discovered.

Aus22's images of the lithosphere below Zealandia are shown in Fig. 18. The continental lithosphere below Northern Zealandia (north and northwest of New Zealand) displays substantially lower seismic velocities compared to the oceanic Tasman Sea lithosphere to its southwest. The low velocities imply a thin, warm lithosphere below Northern Zealandia. This observation is consistent with the

extensive rifting and possible lithospheric delamination that has been proposed to create the current bathymetry (Sutherland et al. 2010).

In Southern Zealandia (south and southeast of New Zealand), low seismic velocities are observed at 36-56 km depths below the Campbell Plateau, in contrast with the higher seismic anomalies beneath the surrounding oceanic lithosphere. The east-central part of Southern Zealandia shows higher seismic velocities at 36-56 km depth, similar to the seismic velocities underlying the Pacific Ocean to its north and east. This implies that the lithosphere below most of the Campbell Plateau in southwestern Southern Zealandia is thinner than below the east-central part of the block, where the lithospheric structure is more similar to the surrounding oceans.

From 80 km downwards the contrast between Zealandia and the surrounding oceans is no longer present. Low velocities are observed across Zealandia and its surroundings and continue towards the eastern part of the Australian continent.

5.3 Azimuthal Anisotropy

Azimuthal anisotropy indicates fabric within the rock at depth created by its pervasive deformation. It is thus a record of the ancient deformation within the currently stable lithosphere and a record of current and recent deformation in the convecting asthenosphere below (e.g., Becker & Lebedev 2021). Given sufficiently large strains, the fast propagation direction of anisotropy indicates the direction of current or past flow in the mantle or the direction of current or past extension (Park & Levin 2002; Becker et al. 2006). For the comparison of former azimuthal anisotropy measurements to current plate motion and paleospreading directions see Becker et al. (2012, 2014); Schaeffer et al. (2016); Becker & Lebedev (2021). *Aus22* resolves the azimuthal anisotropy within and beneath the Australian Plate and offers new information on the past and present deformation and flow (Fig. 8).

Beneath the oceans, the orientation of the fast-axis of anisotropy in the upper ~100 km of the mantle indicates anisotropic fabric that is frozen within the oceanic lithosphere (e.g., Becker et al. 2014; Schaeffer et al. 2016), which, in and around the Australian Plate, is up to 180 Ma (e.g., Müller et al. 2008). In *Aus22*, the oceanic lithosphere in and around the Australian Plate shows the expected fast propagation directions parallel to the paleo-spreading directions (e.g., Becker et al. 2014; Schaeffer et al. 2016) beneath the Indian Ocean west of Australia (NW-SE fast direction), in the Coral Sea to the east (NE-SW fast direction), and in the vicinity of the Southeast Indian Ridge (SEIR) south of Australia (N-S fast direction**, figure 8**). As we move from SEIR northwards towards Australia, the N-S fast direction rotates towards E-W near the continent's southern margin. We propose that this E-W fabric was formed by deformation during the protracted, oblique early phases of the Australia-Antarctica break-up (Müller et al. 2016).

In the asthenosphere beneath oceans, the dominant pattern observed globally shows fast propagation directions parallel to the current plate motions and, near the mid-ocean ridges, to the spreading directions **(figure 8)**. This probably reflects the shearing of the asthenosphere by the motion of the plate above it. Exceptions to this global pattern are likely to indicate regional flow of the asthenosphere. *Aus22* shows a high amplitude N-S fast-propagating direction azimuthal anisotropy signal in the asthenosphere around the region of the Australian-Antarctic Discordance (AAD, Fig. 1), parallel to the spreading direction of the ridge. The high amplitude anisotropy continues northwards towards southern Australia and southwards towards northern Antarctica (Fig. 8). East of the AAD the fast-propagating direction changes from ridge-perpendicular to ridge-parallel. The ridge-parallel motion continues towards the location of the Balleny hotspot (Fig. 8). This observation suggests the presence of ridge-parallel flow below the eastern Southeast Indian Ridge, which could originate from the hot (plume) material sourcing the Balleny hotspot, spreading laterally along the ridge. The ridge-parallel flow of hot asthenospheric mantle material can also be supported by the significantly low S-wave seismic velocities observed below the ridge between the Balleny hotspot and the AAD.

Beneath continents, the fast-propagation directions observed in the lithosphere give information about the past tectonic events that have created the continental lithosphere. Beneath the Precambrian western and central parts of Australia, the lithosphere reaches 250-300 km in thickness (Haynes et al. 2020; Fullea et al. 2021), which is confirmed by our S-velocity images (Fig. 5). The fast-propagation directions in the upper 250-300 km thus provide information about fabric that is created by deformation billions of years ago. In eastern Australia, the continental lithosphere is thinner, and at least some of the anisotropic fabric within it is likely to be related to its Palaeozoic accretion to the core of the continent.

A strong variation in fast-propagation direction with depth is observed in *Aus22* within the cratonic lithosphere of Australia. This variation suggests the presence of layering of azimuthal anisotropy, frozen in by different processes throughout the formation and accretion of the cratonic lithosphere. This layering system of the Australian cratonic lithosphere has been proposed by Heintz & Kennett (2006) and observed in previous azimuthal anisotropy studies of the Australian Plate (Debayle & Kennett 2000; Simons et al. 2002). A similar layering has been observed in other cratonic roots (e.g., Yuan & Romanowicz 2010).

Former regional azimuthal anisotropy models, as well as global anisotropy models (e.g., Debayle et al. 2005; Schaeffer et al. 2016), show a N-S to NNE-SSW fast-propagation direction at 150-200 km below Australia. This observation has been interpreted as asthenospheric flow below the continent, following the N-S motion of the Australian Plate (Debayle et al. 2005; Heintz & Kennett 2006). 150-200 km depth is, however, within the deep cratonic lithosphere beneath most of the continent, rather

than in the asthenosphere, making this observation somewhat puzzling. *Aus22* shows a similar N-S fast-propagation direction in central Australia at 150-200 km depth, but no strong N-S fast-propagation direction is observed at 260-330 km depth, which is the depth range one would expect to see the N-S fast-propagation direction due to the asthenospheric flow following the plate motion, underlying a deep cratonic lithospheric root. A few possible explanations for this observation are that a) the lithosphere below Australia is thinner than observed by isotropic-average models and petrological inversions and 150-200 km is in the asthenosphere, not in the lithosphere, b) the vertical resolution of anisotropy models is imperfect, placing the N-S fabric more shallow than its actual depth, c) the cratonic lithosphere has been deformed by the recent northward motion of Australia, d) the fabric frozen from ancient time in the deep cratonic lithosphere happens to align with the current plate motion. Following the current knowledge of the lithosphere below Australia and the characteristics of cratonic roots, the latter explanation is most plausible. In *Aus22* we observe that the N-S fast-propagation direction is only present in central Australia, while west Australia shows a NE-SW fast-propagation direction. This shows there is a variety in fast-propagation direction within the cratonic lithosphere at 150-200 km depth, likely presenting lateral variation of frozen-in azimuthal anisotropy signal within the lithosphere. The lack of a strong N-S fast-propagating direction in the asthenosphere below the cratonic lithosphere could be due to the strong variation in lithospheric thickness below the continent, causing local complex flow patterns that deviate from the general N-S plate motion.

The asthenosphere in subduction zones generally shows trench-parallel fast-propagation directions (Long & Silver 2009), which we also observe in *Aus22*; along the Java Trench (WNW-ESE) and along the Tonga-Kermadec-Hikurangi trench (NNE-SSW). A bend in the fast-propagation direction is observed around the tip of the Tonga trench, in agreement with the toroidal flow around the tip of subduction zones observed in previous anisotropy studies (e.g. Zandt & Humphreys (2008); Civello & Margheriti (2004)).

5.4 Diamondiferous Deposits

The presence of diamondiferous kimberlites and lamproites is linked to the existence of thick, cold cratonic lithosphere at the time of their eruption (Faure et al. 2011; Schaeffer & Lebedev 2014). This is because the pressure-temperature conditions that are needed for diamond stability require the presence of a lithosphere of over 150 km thick (Boyd et al. 1985; Pearson et al. 2003). It has been suggested that diamond-bearing outcrops occur preferentially at the boundaries of cratonic lithosphere, which could be linked to the proximal occurrence of the deep sources of diamondiferous rocks and mechanisms for their eruption (McKenzie & Priestley 2008). Recent tomography of different continents, however, does not appear to support this theory (Celli et al. 2020a; Schaeffer & Lebedev 2014). Diamonds can

be used as a proxy for the lateral extent of cratonic lithosphere in the past. An absence of thick cratonic lithosphere beneath sites of diamondiferous kimberlites suggests erosion of the cratonic lithosphere since the time of their eruption (e.g., Menzies et al. 1993; Griffin et al. 1998; Celli et al. 2020a).

The locations of the diamondiferous deposits in Australia are plotted over the outline of the cratonic lithosphere in Fig. 16 (bottom left). Almost all the diamondiferous kimberlites and lamproites are located above thick, cratonic lithosphere, with a small minority near its boundaries. It has been proposed previously that the diamondiferous kimberlites and lamproites are located at the boundary of cratonic lithosphere in Australia (Jaques & Milligan 2004; O'Neill et al. 2005; Fishwick 2006), but evidence from *Aus22* does not support this, with most of the outcrops located well within the boundaries of the cratonic lithosphere.

One notable exception is the diamondiferous lamproites in the King Leopold Orogen, southwest of the Kimberley Craton in northwest Australia. These lamproites are the youngest diamondiferous deposits found in Australia, 20 Ma (McInnes et al. 2012), and are located above an area of lithosphere with velocities that are relatively high but lower than beneath most of the North and West Australian Cratons (see section 5.1.1).

The absence or reduced thickness of cratonic lithosphere below these lamproites could be explained by cratonic erosion since the time of their eruption. Lithospheric erosion can be caused by various mechanisms: subduction (Kusky et al. 2014), rifting (Wenker & Beaumont 2018) or the influence of an underlying plume (Sobolev et al. 2011; Celli et al. 2020a). The King Leopold area did not experience any subduction or rifting in the last 20 Ma (Tyler & Griffin 1990), making their influence unlikely. The presence of a plume has been suggested by McInnes et al. (2012), based on the age progression seen in the lamproitic eruptions around northwest Australia. Following the general NNW path of the Australian continent over the last 20 Ma, this would put the current location of the plume below the southern West Australian Craton. This area is, however, underlain by a thick lithospheric root, and no significant low-velocity anomaly is present in *Aus22* in the deeper upper mantle. Further north, below the northwestern tip of Australia, *Aus22* does show a low-velocity anomaly. If, indeed, the cratonic lithosphere was eroded by a plume, the plume must have either waned or moved laterally over time.

Alternatively, the lamproites may have erupted in the current lithospheric configuration—within an area of intermediate-thickness continental lithosphere surrounded by very thick cratonic lithosphere. The somewhat thinner lithosphere could have been just thick enough for the diamond stability field to be present within it, and it could also facilitate low-degree decompression melting near its bottom due to it smaller thickness. The melt is required for the diamond-bearing lamproites to form and reach the surface (e.g., McKenzie & Priestley 2008; Giuliani & Pearson 2019).

Diamonds have also been found in alluvial deposits in eastern Australia, above a thin, warm lithosphere. The origin of these diamonds is debated. Two types of diamonds have been identified in the alluvial deposits, one Precambrian (Group A) and the other Early Carboniferous-early Permian (Group B, Davies et al. (1999); Barron et al. (2005)). Group B shows little travel erosion, which would be consistent with a local source (Burgess et al. 1998; Griffin et al. 1998). Barron et al. (2005) proposed that these diamonds may have formed in a subduction zone setting, instead of below cratonic lithosphere, which matches the deviations in the characteristics of the diamonds compared to typical cratonic diamonds. With the age of the diamonds coinciding with the subduction processes along the eastern Australian margin, these diamonds could indeed be linked to the same processes that created eastern Australia's lithosphere, as discussed in section 5.1.3.

5.5 Intraplate Volcanism and Hotspots

5.5.1 Cenozoic Volcanism

The eastern margin of the Australian continent is scattered with numerous Cenozoic volcanoes. All of the volcanic areas are underlain by low seismic velocities at 20-200 km depths in *Aus22* (Fig. 14), indicating the presence of a warm, thin lithosphere (Fig. 16). At 80-110 km depths, peaks in the amplitudes of low velocities are observed below major volcanic regions (Fig. 14), implying the presence of a certain degree of partial melt (section 3.1). The global thermochemical model WINTERC-G (Fullea et al. 2021) has lower lateral resolution than *Aus22* but estimates 0.5-1.5% melt beneath substantial parts of the area, near 80 km depth, consistent with active or recently active intraplate volcanism. Some areas, including Tasmania and the Bass Strait in the south, however, have not experienced any volcanism for a long time ($>$ 10Ma, Johnson et al. (1989); Wellman & McDougall (1974)), implying the absence of conditions for it there.

Three types of Cenozoic volcanoes have been classified in Australia by Wellman & McDougall (1974) and are widely adopted since: 1) central volcanoes, which are predominantly basaltic but also have felsic lava flows and intrusions, 2) lava fields, which are basaltic, extensive and thin, and 3) leucitites, which are low-volume, potassium-rich leucitite bearing lavas. 40Ar-39Ar geochronological studies have identified N-S age-progressive tracks in the central volcanoes and leucitites (Cohen et al. 2008; Vasconcelos et al. 2008; Knesel et al. 2008), and these have been linked to the passage of the continent over one or more mantle plumes (Tychkov et al. 1998; Sutherland 2003; Cohen et al. 2008; Sutherland et al. 2012; Jones & Verdel 2015). The lava fields, by contrast, do not show any age progression (Fig. 14) and have been linked to various alternative processes including edge-driven convection (EDC, Demidjuk et al. (2007); Fishwick & Rawlinson (2012)), shear-driven upwelling (SDU, Davies & Rawlinson (2014); Rawlinson et al. (2017)) and slab flux (Mather et al. 2020).

Four age-progressive volcanic tracks have been identified in the central volcanoes and leucitites: 1) Comboyne, reaching from Fraser Island in Queensland (~32 Ma) to Comboyne in New South Wales (16 Ma) (Knesel et al. 2008), 2) Canobolas, reaching from Bunya (~24 Ma) in Queensland to Canobolas in New South Wales (12 Ma) (Sutherland et al. 2012), 3) Buckland, reaching from Cape Hillsborough (~34 Ma) to Buckland (27 Ma) (Cohen et al. 2013) and 4) The Leucitite Line, reaching from Bokhara River (~17 Ma) to Cosgrove (9 Ma) Cohen et al. (2008). Davies et al. (2015) linked the Buckland and the Leucitites together to form a single hotspot track, the Cosgrove Track, and explained the absence of volcanism between the two tracks by the presence of thicker lithosphere, preventing the plume material to reach the surface. Tychkov et al. (1998) and Sutherland (2003) proposed that all four chains arose from a single mantle plume, created by plume material that migrated southeast towards thinner lithosphere before ascending, or due to westward plume divergence due to plate motion trends, respectively.

The defining influence of lithospheric thickness on the locations of the Cenozoic volcanism is demonstrated clearly by *Aus22*. All Cenozoic volcanic areas are underlain by thin Phanerozoic lithosphere. The gap in volcanism between the Buckland and Leucitites is collocated with a region of thicker, intermediate lithosphere (see section 5.1.3, Figs 14 and 16). This intermediate lithosphere is not as thick as the cratonic lithosphere to the west, but, as our results indicate, is thick enough to prevent volcanism. Our steps in lithospheric thickness differ from the lithospheric thickness obtained by Davies et al. (2015), which was estimated by combining the body and surface wave tomography models of Davies & Rawlinson (2014) Rawlinson et al. (2015) and Kennett et al. (2013). Davies et al. (2015) suggest a thick lithospheric root below the southern part of the gap in the Cosgrove track and a thick (although more patchy) lithosphere in the area surrounding leucitites, whereas in *Aus22* the lithosphere below the leucitites is significantly thinner, more consistent with the presence of these volcanoes.

From Fig. 14 and 16, we can observe that the Canobolas track is located close to the eastern edge of the intermediate lithosphere. This suggests that this track could have been formed by the eastward deviation of hot upwelling material, with decompression melting and with melts rising to the surface below the thinner lithosphere. The age and location of the termination of the Canobolas and Comboyne tracks also correlate with the thinning of the lithosphere at the Cosgrove Track at the start of the Leucitite track. A single hot plume as a source for these various volcanic tracks could thus be a plausible explanation, being strongly influenced by the lithospheric thickness of the Australian continent it encounters, supporting the view of Davies et al. (2015).

The current position of the plume proposed to have created the Cosgrove track is below the Bass Strait (Davies et al. 2015). It has also been referred to as the East Australia hotspot (Montelli et al.

2006). The absence of recent (<5 Ma) intraplate volcanism and the lack of evidence for a plume in previous tomographic models (Fishwick & Rawlinson (e.g., 2012), see Fig. A1 in Appendix A1) suggested that the plume has waned (Rawlinson et al. 2015). Davies et al. (2015) and Rawlinson et al. (2017) propose that the plume was captured by a pre-existing edge-driven convection cell located around the Newer Volcanic Province at 6 Ma. They propose that this interaction triggered the onset of volcanism in the Newer Volcanic Province at 5 Ma, progressing westward since that time to create the westward younging chain of volcanoes in the area.

In *Aus22*, a wide zone of low velocity is visible below the Bass Strait at 80-110 km, continuing along the southwest coast towards the southern tip of the Canobolas and Comboyne tracks. Below 110 km, the low-velocity anomaly fades and slightly positive seismic velocity anomalies become visible from 200 km downwards (Fig. 5). A similar seismic structure was observed by Fishwick & Rawlinson (2012) and, also, in global the P- and S-wave models of Montelli et al. (2006) (PRI-P05 and PRI-S05, respectively) and in the global S-wave models SL2013v, 3D2016-09Sv and SEMum2 (Fig. A2 in Appendix A). The absence of a low-velocity seismic structure below 110 km depth below the Bass Strait suggests that the plume has indeed waned or, alternatively, that the source of the East Australian hotspot is not located below the Bass Strait. Our results suggest that it could possibly be connected to the same source feeding the Lord Howe and Tasmantid hotspot (see section 5.5.2). This is consistent with the north-eastward continuation of the low-velocity zone below the Bass Strait along the southeast coast of Australia at 80-110 km depth, connecting it to the low-velocity zone below the Lord Howe and Tasmantid hotspot in the transition zone (Fig. 7E, F).

5.5.2 Lord Howe and Tasmantid Hotspots

The Lord Howe and Tasmantid hotspots are located in the Tasman Sea and have been identified by two parallel age-progressive volcanic seamounts tracks (Fig. 2, McDougall & Duncan (1988)). The most recent seamounts age 6 and 7.2 Ma, respectively (Knesel et al. 2008), and the current location of the hotspots is inferred from the plate velocity of the Australian Plate. The absence of any seamounts at the current location of the hotspots and the decrease in the eruption volume in the seamounts over time suggest that the mantle source feeding these hotspots has waned (Seton et al. 2019).

In *Aus22* the full extent of the Tasman Sea and northern Zealandia is characterized by a negative velocity anomaly throughout at 80-200 km depth, but no peak in low velocity is observed below the current locations of the two hotspots. A similar structure is seen in global S-wave models (Fig. A2 in Appendix A2). At shallow depths, 20-56 km deep, even a slight high-velocity anomaly is observed in *Aus22* below the area of the hotspots (cross-section F in Fig. 7). These observations imply that the source once feeding the seamounts is no longer present at lithospheric depths and, consistent with

the plume responsible for the hotspots waning after 6 Ma (the youngest seamount of the two hotspot tracks), with the lithosphere growing in thickness since then.

From 260 km depth downward, a peak in low velocity becomes visible east of the Lord Howe hotspot, which moves southwest with depth towards the bottom of the transition zone. In the transition zone, this anomaly stretches from the coast of southeast New South Wales to the northern tip of New Zealand (Fig. 5). A similar peak in low velocity is observed in global P-wave models, stretching E-W from offshore southeast New South Wales to northern New Zealand, fading above the transition zone (Fig. A5 in Appendix A3). This peak in low velocity implies the presence of hot mantle material below the region and can be interpreted as the plume that sourced the Lord Howe and Tasmantid hotspot (and possibly also the East Australia hotspot, see section 5.5.1). The presence of this anomaly thus implies that although the plume has waned, hot material is still present in the transition zone and, possibly, up to 200 km depth.

Due to the low resolution and mainly E-W source-station path crossings in the transition zone below this area, the exact shape of the low-velocity anomaly is somewhat uncertain. Spike tests (similar to the tests in section 4.1, Fig. A6) have shown that a low-velocity anomaly of similar amplitude would result in a lower velocity anomaly located towards southeast Australia than below northern Zealandia. This implies that although the highest peak in low seismic velocity is located just off the east coast of Australia, this peak could be located more westward. Alternatively, two peaks could be present, averaging into a single, wide low-velocity anomaly in the transition zone in *Aus22* (see Fig. A6).

If a single plume source is present in the transition zone and has been feeding the three hotspots, this means that the plume upwelling has split into different branches in the upper mantle. One possible reason for the splitting of the plume could be the complex 3-D flow of the plume material in the upper mantle due to the variations of lithospheric thickness (Mortimer et al. 2017; Gallais et al. 2019). The thickness of the lithosphere in the area of the three hotspots is complex and varies due to the presence of an extinct ridge, subduction processes and rifted continental lithosphere (Fig. 18). The interaction of the plume material with the variations in the lithospheric thickness or other heterogeneities in the upper mantle (Mather et al. 2020) may cause the plume material to spread into fingers and cause volcanism at different locations.

5.5.3 Samoa Hotspot

The Samoa hotspot is located north of the northern tip of the Tonga Trench and, despite the lack of a clear age-progressive volcanic chain (Hawkins Jr & Natland 1975), has been linked to an underlying plume by geochemical analysis (Koppers et al. 2008) and seismic imaging (Montelli et al. 2006; Zhao 2007). The plume is known as the Samoa Plume and is proposed to originate from an Ultra-Low

Velocity Zone (ULVZ) in the large low shear-wave velocity province beneath the Pacific Plate (Thorne et al. 2013). Due to the close proximity of the Samoa Hotspot to the Tonga Trench, there is a complex interaction of the plume with the Tonga slab, entraining plume material around the subducting plate (Druken et al. 2014; Chang et al. 2016). Based on petrological-thermo-mechanical modelling Chang et al. (2016) argue that the physical barrier caused by the presence of the Tonga Slab causes the rising plume upwelling to change direction, moving parallel to the Tonga Slab and arching around its northernmost tip at lithospheric depths.Druken et al. (2014) used 3D laboratory models to show how the slab-driven flow driven by the subducting Tonga Slab could distort the flow driven by the upwelling Samoa plume.

In *Aus22* a low seismic velocity is visible north of the Tonga subduction zone from 80 km depth downwards. With increasing depth, the low-velocity zone moves eastwards, curving southwards around the tip of the Tonga slab from 110 to 260 km depth (Fig. 5). Below 260 km depth, the negative velocity anomaly is vertical and located east of the northernmost tip of the Tonga trench (Fig. 5). The amplitude of the anomaly in the model decreases with depth, but it is visible down to the bottom of the transition zone. This is consistent with the azimuthal anisotropy resolved by *Aus22* (Fig. 8, see section 4.2); the fast-propagating direction of the azimuthal anisotropy bends around the tip of the Tonga Slab at 150-56 km depth. These observations thus suggest a strong distortion of the Samoa plume by the overlying Tonga Slab, as modelled previously in the geodynamic studies of Druken et al. (2014) and Chang et al. (2016). *Aus22* implies that the plume rises vertically in the transition zone until it reaches the bottom of the Tonga Slab. The Tonga slab acts as a barrier for the uprising buoyant flow of the Samoa Plume, forcing horizontal flow of plume material towards the north. At the northern tip of the Tonga Slab, the Samoa plume can rise, bending around the tip of the slab to the west, as the trench retreats towards the east. (See Fig. 6 of Chang et al. (2016) for the illustration of this process).

5.5.4 Other Hotspots

Various other hotspots have been proposed in and around the Australian Plate, but their source is less well resolved by *Aus22*.

Below the Caroline Hotspot, only a slight peak in low velocity is visible below 660 km in *Aus22*. This observation agrees with the absence of a seismic signature in the upper mantle in other global P- and S-wave models (Fig. A2 - A5 in appendix A). The youngest volcanic island linked to the Caroline Hotspot is ~1 Ma (Keating et al. 1984). The underlying plume could thus have waned, with relatively high temperatures still present in the deeper mantle, as imaged by Montelli et al. (2006).

The Balleny Hotspot is underlain by a strong low-velocity anomaly at lithospheric depths that fades in amplitude towards the transition zone (cross-section 6 and H in Fig. 7). At lithospheric depths,

the low-velocity anomaly below the Balleny Hotspot is connected to the low velocities located below the Southeast Indian Ridge to its north. This observation, together with the anisotropy results (see section 4.2), suggests that the hot (possible plume) material underlying the Balleny hotspot interacts with the hot material below the Southeast Indian Ridge.

The Cocos-Keeling, Indian Ocean and Chatham hotspots do not have a surface expression but have been proposed by Montelli et al. (2006) as possible hotspot locations based on the presence of low-velocity anomalies in the mantle below these locations. The Cocos-Keeling hotspot is underlain by a low-velocity anomaly in the lithosphere, which fades rapidly below 200 km depth (Fig. 5 and cross-section 1 and C of Fig. 7). The absence of any low-velocity anomaly below 200 km depth could be explained by the lack of resolution below the lithosphere in the Indian Ocean. Neither the Indian Ocean nor the Chatham hotspots show any low-velocity anomalies in the upper mantle beneath them.

5.6 Subducted Lithosphere

The north and east boundaries of the Australian Plate are convergent boundaries. With the relatively cold temperature of the subducting plates, they can be identified by high seismic velocity bodies in *Aus22*. In the following paragraphs, we discuss the seismic expression of the various subducting slabs at the converging trenches and the presence of possible slab remnants of former subduction zones below the plate. The naming of the slabs in the following paragraphs will follow those of Wu et al. (2016) and Van der Meer et al. (2018).

5.6.1 Active subduction zones

The largest, continuous subduction zone bounding the Australian Plate is the Java Trench (the western part of the Java Trench is also referred to as the Sunda Trench), ranging from North Sumatra, along Java, to Sumba (Fig. 5). Here oceanic Australian plate is subducting below the Sunda Plate (also known as Sundaland), subducting seafloor ageing from 50 Ma in North Sumatra to 160 Ma near Flores, and is known as the Sunda slab. The Sunda slab has been first imaged by the P-wave model of Widiyantoro & van der Hilst (1996) and has been verified by many tomographic models since (e.g., Widiyantoro et al. 2011; Amaru 2007; Zenonos et al. 2019; Wehner et al. 2022). In *Aus22* the Sunda slab is visible by a high-velocity body that is present below the trench from 80 km downwards. Below North Sumatra, the anomaly fades below 330 km depth, while below Java and Flores it is present down to the bottom of the transition zone. This observation agrees with previous tomographic models and the distribution of earthquakes along the trench (deep earthquakes are absent below North Sumatra, while they continue to the base of the transition zone along the rest of the trench, Hutchings & Mooney (e.g., 2021)).

The Banda Arc, located east of the Java Trench, extends along the Timor Trough and bends west-

ward along the Seram Trough to the north. Spakman & Hall (2010) have shown, using seismic tomography and plate tectonic reconstructions, that the Banda Arc has formed by rollback towards the south-southeast to obtain its current configuration. Based on GPS data and geological observations it is interpreted that subduction along this trench has ceased (e.g., Tregoning et al. 1994; Kreemer et al. 2000), which has been linked to the arrival of continental lithosphere at the trench (Spakman & Hall 2010). In *Aus22*, the Banda Arc is underlain by high seismic velocities below 150 km depth (Fig. 2). This high-velocity body is higher in amplitude and wider than the velocity anomalies underlying the Java trench. The transition between the two is located east of the Island of Sumba, coinciding with the arrival of continental lithosphere at the trench (Fig. 1). This observation agrees with recent regional P-wave tomography models (Harris et al. 2020; Supendi et al. 2020). Harris et al. (2020) proposed that part of the continental lithosphere of Australia is subducted before subduction ceased and Supendi et al. (2020) argued for the presence of a forearc sliver of continental origin above the subducted oceanic lithosphere. From *Aus22* we cannot distinguish between the two possibilities. From *Aus22* we can infer that the cratonic lithosphere of Australia extends to the Timor Trough (visible at 80-110 km depth, Fig. 5 and Fig. 14). This implies that the termination of subduction at the Timor Trough is likely due to the arrival of the cratonic lithosphere at the trench and that the thick slab below the trough represents subducted non-cratonic (continental) lithosphere.

At the eastern part of the Banda Arc, the tomography of *Aus22* roughly agrees with the tomography of UU-P07 (Figs A4 and A4 in appendix A) and the regional tomography models of Zenonos et al. (2019) and Wehner et al. (2022). At 150 km depth, a curved high-velocity anomaly is visible along the full westward curvature in *Aus22*; this anomaly fades at 200 km depth below the Seram Trench, the northern part of the Banda Arc, while it is still present below the southern Banda Arc. From 260 to 410 km depth, no prominent high velocity can be observed below the Banda Arc in *Aus22*, but in the transition zone, a high-velocity body becomes visible in the middle of the arch, below the Banda Sea. Based on the tomography of UU-P07, Spakman & Hall (2010) correlate the missing high-velocity anomaly below the Seram Trench to a slab tear below the region and propose a slab flattening of the Banda Slab below the Banda Sea in the transition zone to explain the high-velocity anomaly observed here.

North of the Banda Arc *Aus22* images various other high-velocity anomalies below active subduction zones, following the areas of high seismic activity. Below the northern Moluccas and Sulawesi *Aus22* images a N-S y-shaped high-velocity body at 150-260 km depth, agreeing with the location of the interpreted double-sided Molucca Sea slab (Hafkenscheid et al. 2001). The Philippine Slab, located below the Philippines, is imaged in *Aus22* by a high-velocity body down to 330 km depth. The Pacific Slab, present below the Mariana Trench, is observed in *Aus22* by a high-velocity body which is visible

down to the base of the transition zone. These observations agree with the tomography of UU-P07 and the regional tomography models of Zenonos et al. (2019) and Wehner et al. (2022), confirming the presence and extent of these slabs.

Below the New Britain Trench, a high-velocity body is visible in *Aus22* down to the top of the transition zone. This feature has been observed in previous tomographic models and has been interpreted as the New Britain slab, where the Solomon Sea Plate is subducting below the Caroline Plate (Hall & Spakman 2002, 2003; Wu et al. 2016). A wide high-velocity area is visible around 260-330 km depth below the trench, which has not been observed by previous body-wave tomography models (Figs A2 - A5 in Appendix A). We propose a few possibilities for this difference. 1) the slab underplates below the Caroline Plate, without significant seismicity, making it hard to detect with body-wave models. 2) The wide area of the high-velocity body is an artefact of *Aus22*, smearing the high velocity of the downgoing slab into the region to its north. 3) The high-velocity zone is not part of the New Britain slab, but instead relates to a (stagnated) slab remnant of a previous subduction in the region. This last option can be supported by the presence of two peaks in high velocity at 200 km depth in *Aus22* (Fig. 5). Slab stagnation has been suggested below the overlying Ramu-Markham fault by Holm et al. (2015), supporting this possibility.

At the northeast boundary of the plate, *Aus22* shows a high-velocity body below the New Hebrides trench. Based on similar observations in previous models it has been interpreted that Australian oceanic lithosphere is subducting here below the New Hebrides Plate and the slab is known as the New Hebrides slab (Fukao et al. 2001; Hall & Spakman 2002; Wu et al. 2016). None of the P-wave models in Figs A4 and A5 in Appendix A3 is able to image this slab well, possibly due to the sparsity of deep events in the region. In *Aus22* the slab is poorly presented above 260 km depth but becomes clearer from 330 km downwards, moving steadily northeast with depth, penetrating down to the base of the transition zone (Fig. 5 and cross-section C in Fig. 7).

At the eastern boundary of the plate, Pacific oceanic lithosphere is subducting below the Australian Plate at the Tonga-Kermadec-Hikurangi subduction zone, as imaged by previous tomographic models (Fig. 10, van der Hilst (1995); Hall & Spakman (2002)). Below the Tonga Trench, the Tonga Slab can be identified in *Aus22* to the base of the transition zone as a strong high-velocity body. At 200-330 km depth a clear westwards curve can be observed at the northernmost tip of the trench, just south of the low-velocity body of the Samoa plume (section 5.5.3). In the transition zone, the high-velocity body widens southwestward but remains within the arc. Extensive slab flattening within the transition zone has been proposed by Lu et al. (2019) based on their tomography model XT2019slab, but this is not observed in *Aus22*. Instead, the slab might flatten below the transition zone, around 800-1000 km depth, as inferred by Schellart & Spakman (2015), which is below the resolution of *Aus22*.

The subducting slab below the Kermadec Trench is less well resolved in *Aus22*. The southern part of the slab, towards the Hikurangi trench, is visible down to 485 km depth, while the central part is only visible at 200-330 km depth as a thin zone of high velocity. At 150 km depth, we observe a visual gap in the slab where a low-velocity body is imaged (cross-section F in Fig. 7). As seismicity is continuous along the Kermadec slab, the slab is possibly present here, but could not be resolved by *Aus22*. A similar absence in high velocity has been detected in UU-P07. This suggests that the slab might be too thin to be detected by tomography. Also at 200-330 km depth, only a slight increase in velocity is observed at the location of the Kermadec arc, indicating that the Kermadec Slab is thinner and less prominent than the adjacent Tonga and Hikurangi slabs. Below 410 km depth, no high-velocity anomaly is observed below the Kermadec Trench. This agrees with the sparsity of seismicity below 410 km depth underneath the trench (Engdahl et al. 1998), suggesting the absence of the slab in the transition zone.

5.6.2 Slab Remnants

In addition to actively subducting slabs, *Aus22* also identifies various high-velocity anomalies in the transition zone that are not related to current subduction zones. These can be interpreted as slab remnants stagnant atop the 660-km discontinuity, which represents a partial barrier to convective flow through it. Oceanic slabs deflecting above 660 km depth have been imaged by tomography in many subduction zones around the globe (Fukao et al. 2009; Van der Meer et al. 2018) and are thought to remain in the transition zone for millions of years before descending into the lower mantle (van Mierlo et al. 2013).

The subducted mantle lithosphere can also be continental, moderately depleted in basaltic constituents and, due to its composition, lighter than oceanic lithosphere. The mantle lithosphere of non-cratonic continental margins, for example, may have sufficient negative buoyancy to subduct down to the transition zone but be too light to penetrate the 660-km discontinuity, thus stagnating for tens or even hundreds of million years (Lebedev & Nolet 2003). We suggest that the cold bodies in the transition zone beneath Australia are continental fragments that used to be located at or near the margins of the continent and were subducted as it moved North.

Below the Cendrawasih Bay in western New Guinea, a small high-velocity body is detected in *Aus22* at 200-410 km depth (Fig. 5). The anomaly is separated from the high-velocity cratonic lithosphere above, as imaged in cross-section 4 in Fig. 7. The anomaly could thus present a delaminated slab, possibly related to the northward subduction of the Australian Plate below the Caroline Plate. Northward subduction of the Australian Plate below the Caroline Plate ceased when the Australian

passive margin entered the subduction zone in the Middle Miocene causing collisional delamination around 7-4 Ma (Cloos 2005).

Below central-north New Guinea, a high-velocity anomaly is observed in close proximity to the anomaly interpreted as the New Britain slab. It is hard to identify if these are one or two slab bodies but can be related to the underthrusting of a slab remnant below the Ramu-Markham Fault, as proposed by Holm et al. (2015) (see section 5.6.1).

Various high-velocity bodies are imaged below the microplates of Southeast Asia around 150-410 km depth (figure 5). Most prominent are the high-velocity bodies below northeast Borneo and Sulawesi. The high-velocity anomaly below northeast Borneo has been observed by the recent regional tomography models of Zenonos et al. (2019) and Wehner et al. (2022) and has been interpreted as a recent slab remnant, possibly related to the northwest subducting Celebes Sea slab from mid-late Miocene (Cottam et al. 2013).

A high-velocity anomaly is imaged in the transition zone below Borneo and this anomaly can possibly present a remnant of the Proto South China Sea slab (Taylor & Hayes 1983). The Proto South China Sea Slab is proposed to have subducted south-eastwards from 45-20 Ma beneath North Borneo (Hall 1996). A similar observation can be made from the tomographic model of Tang & Zheng (2013), which images a high-velocity body below northern Borneo in the upper mantle. Hall & Spakman (2015), on the other hand, argues that the Proto-South China Sea slab is present deeper in the mantle, around 800-1100 km, based on the tomography of UU-P07 (Amaru 2007).

Below Northeast Australia, three high-velocity anomalies are imaged by *Aus22* in the transition zone. The location and depth of the anomalies roughly correlate with the proposed location of the 'Welford slab', based on a high-velocity anomaly identified in UU-P07 by Van der Meer et al. (2018). Various global S- and P-wave tomography models have observed high-velocity anomalies in this region, varying in location and amplitude (Fig. 10). The Welford slab has been related to the south-westward Trobriand subduction zone (van Ufford & Cloos 2005). The subduction zone is proposed to have formed as a far-field response to the collision of the Ontong Java Plateau with the Melanesian arc around 26-20 Ma (Knesel et al. 2008).

A high-velocity body is imaged below the southern Solomon Sea in the transition zone. The location of the anomaly correlates with the location of the 'Solomon Sea South' slab, as identified by Wu et al. (2016). The origin of this slab remnant, however, remains unknown.

6 CONCLUSIONS

Using waveform inversion of massive regional and global datasets, optimized regularization and region-specific error analysis and mitigation, *Aus22* reveals the seismic structure of the upper mantle beneath

the region including the Australian Plate and its boundaries at a new level of detail. In this study, we have made the following observations and inferences from *Aus22*.

- Thick, cratonic lithosphere underlies most of central and western Australia and extends northwards offshore beneath the Timor Sea and the Arafura Sea, up the northern boundary of the plate at the Timor Trough and Central Range orogeny of New Guinea.
- The new tomography and independent interstation surface-wave measurements both show that cratonic lithosphere underlies the Gulf of Carpentaria and the near-coastal lowlands to the south and southeast. The cratonic lithosphere is separated by a sharp boundary from the Georgetown Inlier to the east, which has a thin, warm lithosphere.
- The eastern boundary of Australia's cratonic lithosphere is mapped in detail and is close to the location of the geologically defined Tasman Line, especially in the south of Australia. The new tomography thus reconciles, to a large extent, the different lines of evidence on the deep and shallow lithospheric boundaries. Differences between the crustal and mantle-lithosphere boundaries provide important evidence of the evolution of the continent.
- A block of lithosphere with intermediate thickness is located just east of the southern part of the Tasman Line, between the thick, cratonic lithosphere to the west and the thin, Phanerozoic lithosphere to the east. The intermediate lithosphere underlies most of the Tasmanides, consistent with an early Paleozoic basement below these orogens, although the possibility of a cratonic basement that has undergone lithospheric erosion cannot be excluded.
- The largely submerged continent of Zealandia is underlain by a thin, warm lithosphere.
- Azimuthal anisotropy within the cratonic lithosphere of Australia shows lateral and vertical variations in the fast-propagation directions. The complex anisotropic structure is likely to have been formed by the multiple deformational events that formed the cratonic root.
- No clear imprint of the N-S motion of the Australian plate is seen in the azimuthal anisotropy in the asthenosphere below most of Australia. The plate-motion parallel fast directions are observed, however, to the south of the continent, below the southern Indian Ocean and the Southeast Indian Ridge.
- The most recent diamondiferous deposits in Australia, the 20 Ma diamondiferous lamproite eruptions at the King Leopold Orogen, are underlain by relatively thick but non-cratonic lithosphere, evidenced both by the tomography and by our independent, interstation surface-wave measurements. The lithospheric heterogeneity may have facilitated bringing the diamonds formed below the surrounding cratonic lithosphere to the surface.
- The Cenozoic volcanic areas in eastern Australia are located, without exception, on thin, warm lithosphere. The gap in volcanism in the Cosgrove hotspot track is underlain by intermediate, mod-

erately thick lithosphere, which probably prevented the rising hot material from reaching the surface. Instead, it appears to have been deflected eastward, to form the Comboyne and Canobolas volcanic tracks.

- Low S-wave velocities are observed at $<$110 km depth below the East Australia hotspot, but no deep plume-like seismic structure is detected. Although we cannot rule out the existence of a plume in the past, we suggest that the hot material is transported to the East Australia hotspot from the same source that feeds the Lord Howe and Tasmantid hotspots, spreading laterally westwards to the East Australian hotspot at sub-lithospheric depth.
- The Tasmantid and the Lord Howe (and possibly the East Australia) hotspots appear to have been sourced from a plume that is seen in the transition zone between New South Wales and Northern New Zealand as an area of low velocities and, by inference, anomalously high temperatures.
- The Samoa plume underlying the Samoa hotspot interacts with the Tonga slab as it ascends to the surface, curving around the northern tip of the Samoa plume at lithospheric depths.
- A high-velocity body below New Guinea is imaged at 200 km depth, indicating the presence of a detached slab fragment. The slab can be associated with subduction termination of the Australian Plate below the Caroline Plate.
- Three high-velocity anomalies are imaged in the transition zone below central-east Australia. We interpret them as fragments of continental lithosphere at the northern margin of Australia, subducted in the course of the northward movement of the continent.

7 DATA AVAILABILITY STATEMENT

The broadband data were obtained from the following online data centres: Australian Passive Seismic Server of the Australian National University (AusPass, `http://auspass.edu.au/`), Bundesanstalt für Geowissenschaften und Rohstoffe Data Centre (BGR, `https://www.bgr.bund.de`), the French Seismologic and Geodetic Network Résif (RESIF, `https://www.fdsn.org/datacenters/detail/RESIF/`), the GEOFON Global Seismic Network (`https://geofon.gfz-potsdam.de`), the Kandilli Observatory and Earthquake Research Institute Data Centre (KOERI, `http://www.koeri.boun.edu.tr`), the Instituto Nazionale di Geofisica Volcanologia Seismological Data Centre (INGV, `https://www.ingv.it`), the Institut de Physique du Globe de Paris Data centre (IPGP, `http://datacenter.ipgp.fr`) the Incorporated Research Institutions for Seismology (IRIS; `http://www.iris.edu`), Ludwig Maximilians Universität München Data Centre (LMU, `https://www.uni-muenchen.de/`), the Observatories and Research Facilities for European Seismology (ORFEUS, `http://www.orfeus-eu.org`), the National Institute for Earth Physics Data Centre (NEIP, `http://www.infp.ro/en/`), the Swiss Seismological Service of the Eidgenössische Technische Hochschule

Zürich (ETH, `http://seismo.ethz.ch`) and the Centro de Sismologia da Universidade de São Paulo (USP, `http://www.moho.iag.usp.br/`).

8 ACKNOWLEDGEMENTS

We thank two anonymous reviewers and the Editor, Huajian Yao, for their constructive comments and suggestions that have helped us to improve the manuscript. We thank Ben Mather for the discussions on the intraplate volcanism on the Australian Plate and for providing us with the locations of the intraplate volcanism. We are grateful to Alexei Gorbatov and Karol Czarnota (Geoscience Australia) for information and discussions on the quality control of the waveform data from Australia. We are grateful to Karen Connors and Lesley Wyborn for the discussions concerning the Australian cratonic lithosphere and its extent below the Arnhem Craton. We thank Tylor Storm and David Mason (USGS) for their help with the correction of the response file of station GT.BOSA. We thank the operators of the regional and global seismic networks and online seismic data centres for creating and providing the data used to generate this model. We thank the creators of the tomographic models that we compare to in this study for making them available and Submachine (`http://www.earth.ox.ac.uk/~smachine/`) for providing the interface to obtain some of these models. All figures were created using Generic Mapping Tools (Wessel & Smith 1995). This work was supported by the research grant 16/IA/4598 co-funded by the Science Foundation Ireland, the Geological Survey of Ireland and the Marine Institute.

REFERENCES

Agius, M. & Lebedev, S., 2013. Tibetan and Indian lithospheres in the upper mantle beneath Tibet: Evidence from broadband surface-wave dispersion, *Geochemistry, Geophysics, Geosystems*, **14**(10), 4260–4281.

Amaru, M. L., 2007. *Global travel time tomography with 3-D reference models*, vol. 274, Utrecht University.

Backus, G. & Gilbert, F., 1970. Uniqueness in the inversion of inaccurate gross Earth data, *Philosophical Transactions of the Royal Society of London. Series A, Mathematical and Physical Sciences*, **266**(1173), 123–192.

Balfour, N., Salmon, M., & Sambridge, M., 2014. The Australian seismometers in schools network: Education, outreach, research, and monitoring, *Seismological Research Letters*, **85**(5), 1063–1068.

Ball, P., Eagles, G., Ebinger, C., McClay, K., & Totterdell, J., 2013. The spatial and temporal evolution of strain during the separation of Australia and Antarctica, *Geochemistry, Geophysics, Geosystems*, **14**(8), 2771–2799.

Barron, B., Barron, L., & Duncan, G., 2005. Eclogitic and ultrahigh-pressure crustal garnets and their relationship to Phanerozoic subduction diamonds, Bingara area, New England Fold Belt, eastern Australia, *Economic Geology*, **100**(8), 1565–1582.

Bassin, C., 2000. The current limits of resolution for surface wave tomography in North America, *EOS Trans. AGU. 81: Fall Meet. Suppl., Abstract*.

Becker, T. & Lebedev, S., 2021. Dynamics of the upper mantle in light of seismic anisotropy, *Mantle Convection and Surface Expressions*, pp. 257–282.

Becker, T., Chevrot, S., Schulte-Pelkum, V., & Blackman, D., 2006. Statistical properties of seismic anisotropy predicted by upper mantle geodynamic models, *Journal of Geophysical Research: Solid Earth*, **111**(B8).

Becker, T., Lebedev, S., & Long, M., 2012. On the relationship between azimuthal anisotropy from shear wave splitting and surface wave tomography, *Journal of Geophysical Research: Solid Earth*, **117**(B1).

Becker, T., Conrad, C., Schaeffer, A., & Lebedev, S., 2014. Origin of azimuthal seismic anisotropy in oceanic plates and mantle, *Earth and Planetary Science Letters*, **401**, 236–250.

Betts, P., Giles, D., Lister, G., & Frick, L., 2002. Evolution of the Australian lithosphere, *Australian Journal of Earth Sciences*, **49**(4), 661–695.

Beyreuther, M., Barsch, R., Krischer, L., Megies, T., Behr, Y., & Wassermann, J., 2010. Obspy: A python toolbox for seismology, *Seismological Research Letters*, **81**(3), 530–533.

Black, L., Withnall, I., Gregory, P., Oversby*, B., & Bain, J., 2005. U–Pb zircon ages from leucogneiss in the Etheridge Group and their significance for the early history of the Georgetown region, north Queensland, *Australian Journal of Earth Sciences*, **52**(3), 385–401.

Blewett, R. S., Kennett, B., & Huston, D., 2012. Australia in time and space, *Shaping a nation: A geology of Australia*, pp. 47–117.

Bonadio, R., Geissler, W., Lebedev, S., Fullea, J., Ravenna, M., Celli, N., Jokat, W., Jegen, M., Sens-Schönfelder, C., & Baba, K., 2018. Hot upper mantle beneath the Tristan da Cunha hotspot from probabilistic Rayleigh-wave inversion and petrological modeling, *Geochemistry, Geophysics, Geosystems*, **19**(5), 1412–1428.

Bonadio, R., Lebedev, S., Meier, T., Arroucau, P., Schaeffer, A., Licciardi, A., Agius, M., Horan, C., Collins, L., O'Reilly, B., et al., 2021. Optimal resolution tomography with error tracking and the structure of the crust and upper mantle beneath Ireland and Britain, *Geophysical Journal International*, **226**(3), 2158–2188.

Boyd, F., Gurney, J., & Richardson, S., 1985. Evidence for a 150–200-km thick Archaean lithosphere from diamond inclusion thermobarometry, *Nature*, **315**(6018), 387–389.

Burgess, R., Phillips, D., Harris, J., & Robinson, D., 1998. Antarctic diamonds in south-eastern Australia? Hints from 40Ar/39Ar laser probe dating of clinopyroxene inclusions from Copeton diamonds, in *International Kimberlite Conference: Extended Abstracts*, vol. 7, pp. 119–121.

Cande, S. & Mutter, J., 1982. A revised identification of the oldest sea-floor spreading anomalies between Australia and Antarctica, *Earth and Planetary Science Letters*, **58**(2), 151–160.

Cawood, P. & Buchan, C., 2007. Linking accretionary orogenesis with supercontinent assembly, *Earth-Science Reviews*, **82**(3-4), 217–256.

Cawood, P. & Korsch, R., 2008. Assembling Australia: Proterozoic building of a continent, *Precambrian Research*, **166**(1-4), 1–35.

Cayley, R., 2011. Exotic crustal block accretion to the eastern Gondwanaland margin in the late Cambrian–Tasmania, the Selwyn Block, and implications for the Cambrian–Silurian evolution of the Ross, Delamerian, and Lachlan orogens, *Gondwana Research*, **19**(3), 628–649.

Cayley, R., Taylor, D., VandenBerg, A., & Moore, D., 2002. Proterozoic–Early Palaeozoic rocks and the Tyennan Orogeny in central victoria: the Selwyn Block and its tectonic implications, *Australian Journal of Earth Sciences*, **49**(2), 225–254.

Celli, N., Lebedev, S., Schaeffer, A., & Gaina, C., 2020a. African cratonic lithosphere carved by mantle plumes, *Nature communications*, **11**(1), 1–10.

Celli, N., Lebedev, S., Schaeffer, A., Ravenna, M., & Gaina, C., 2020b. The upper mantle beneath the South Atlantic Ocean, South America and Africa from waveform tomography with massive data sets, *Geophysical Journal International*, **221**(1), 178–204.

Chang, S.-J., Ferreira, A. M., & Faccenda, M., 2016. Upper-and mid-mantle interaction between the Samoan plume and the Tonga–Kermadec slabs, *Nature communications*, **7**(1), 1–9.

Chantel, J., Manthilake, G., Andrault, D., Novella, D., Yu, T., & Wang, Y., 2016. Experimental evidence supports mantle partial melting in the asthenosphere, *Science advances*, **2**(5), e1600246.

Civello, S. & Margheriti, L., 2004. Toroidal mantle flow around the Calabrian slab (Italy) from SKS splitting, *Geophysical Research Letters*, **31**(10).

Cloos, M., 2005. *Collisional delamination in New Guinea: The geotectonics of subducting slab breakoff*, vol. 400, Geological Society of America.

Cohen, B., Knesel, K., Vasconcelos, P., Thiede, D., & Hergt, J., 2008. 40Ar/39Ar constraints on the timing and origin of Miocene leucitite volcanism in southeastern Australia, *Australian Journal of Earth Sciences*, **55**(3), 407–418.

Cohen, B., Knesel, K., Vasconcelos, P., & Schellart, W., 2013. Tracking the Australian plate motion through the Cenozoic: Constraints from 40Ar/39Ar geochronology, *Tectonics*, **32**(5), 1371–1383.

Collins, J. & Sheehan, A., 2009. Marine observations of anisotropy near Aotearoa.

Coney, P., 1992. The Lachlan belt of eastern Australia and circum-Pacific tectonic evolution, *Tectonophysics*, **214**(1-4), 1–25.

Connors, K. & Pryer, L., 2018. Secrets from the deep: greater McArthur Basin SEEBASE study helps unravel evolution of the basin and its underlying basement.

Cottam, M., Hall, R., Sperber, C., Kohn, B., Forster, M., & Batt, G., 2013. Neogene rock uplift and erosion in northern Borneo: evidence from the Kinabalu granite, Mount Kinabalu, *Journal of the Geological Society*, **170**(5), 805–816.

Courtillot, V., Davaille, A., Besse, J., & Stock, J., 2003. Three distinct types of hotspots in the Earth's mantle, *Earth and Planetary Science Letters*, **205**(3-4), 295–308.

Darbyshire, F. & Lebedev, S., 2009. Rayleigh wave phase-velocity heterogeneity and multilayered azimuthal anisotropy of the Superior Craton, Ontario, *Geophysical Journal International*, **176**(1), 215–234.

Davey, F. & Smith, E., 1983. The tectonic setting of the Fiordland region, south-west New Zealand, *Geophys-*

ical Journal International, **72**(1), 23–38.

Davies, D., Rawlinson, N., Iaffaldano, G., & Campbell, I., 2015. Lithospheric controls on magma composition along Earth's longest continental hotspot track, *Nature*, **525**(7570), 511–514.

Davies, D. R. & Rawlinson, N., 2014. On the origin of recent intraplate volcanism in Australia, *Geology*, **42**(12), 1031–1034.

Davies, G., 1988. Ocean bathymetry and mantle convection: 1. large-scale flow and hotspots, *Journal of Geophysical Research: Solid Earth*, **93**(B9), 10467–10480.

Davies, R., O'Reilly, S., & Griffin, W., 1999. Diamonds from Wellington, NSW: insights into the origin of eastern Australian diamonds, *Mineralogical Magazine*, **63**(4), 447–471.

Debayle, E., 1999. Sv-wave azimuthal anisotropy in the Australian upper mantle: preliminary results from automated Rayleigh waveform inversion, *Geophysical Journal International*, **137**(3), 747–754.

Debayle, E. & Kennett, B., 2000. The Australian continental upper mantle: structure and deformation inferred from surface waves, *Journal of Geophysical Research: Solid Earth*, **105**(B11), 25423–25450.

Debayle, E., Kennett, B., & Priestley, K., 2005. Global azimuthal seismic anisotropy and the unique plate-motion deformation of Australia, *Nature*, **433**(7025), 509–512.

Debayle, E., Dubuffet, F., & Durand, S., 2016. An automatically updated s-wave model of the upper mantle and the depth extent of azimuthal anisotropy, *Geophysical Research Letters*, **43**(2), 674–682.

DeMets, C., Gordon, R., & Argus, D., 2010. Geologically current plate motions, *Geophysical Journal International*, **181**(1), 1–80.

Demidjuk, Z., Turner, S., Sandiford, M., George, R., Foden, J., & Etheridge, M., 2007. U-series isotope and geodynamic constraints on mantle melting processes beneath the Newer Volcanic Province in South Australia, *Earth and Planetary Science Letters*, **261**(3-4), 517–533.

Direen, N. & Crawford, A., 2003. The Tasman line: where is it, what is it, and is it Australia's Rodinian breakup boundary?, *Australian Journal of Earth Sciences*, **50**(4), 491–502.

Druken, K., Kincaid, C., Griffiths, R., Stegman, D., & Hart, S., 2014. Plume–slab interaction: the Samoa–Tonga system, *Physics of the Earth and Planetary Interiors*, **232**, 1–14.

Duncan, R. & Richards, M., 1991. Hotspots, mantle plumes, flood basalts, and true polar wander, *Reviews of Geophysics*, **29**(1), 31–50.

Dziewonski, A., Chou, T.-A., & Woodhouse, J., 1981. Determination of earthquake source parameters from waveform data for studies of global and regional seismicity, *Journal of Geophysical Research: Solid Earth*, **86**(B4), 2825–2852.

Eeken, T., Goes, S., Pedersen, H., Arndt, N., & Bouilhol, P., 2018. Seismic evidence for depth-dependent metasomatism in cratons, *Earth and Planetary Science Letters*, **491**, 148–159.

Ekström, G., Nettles, M., & Dziewoński, A., 2012. The global CMT project 2004–2010: Centroid-moment tensors for 13,017 earthquakes, *Physics of the Earth and Planetary Interiors*, **200**, 1–9.

El-Sharkawy, A., Meier, T., Lebedev, S., Behrmann, J., Hamada, M., Cristiano, L., Weidle, C., & Köhn, D., 2020. The slab puzzle of the Apine-Mediterranean region: Insights from a new, high-resolution, shear wave

velocity model of the upper mantle, *Geochemistry, Geophysics, Geosystems*, **21**(8), e2020GC008993.

Endrun, B., Lebedev, S., Meier, T., Tirel, C., & Friederich, W., 2011. Complex layered deformation within the Aegean crust and mantle revealed by seismic anisotropy, *Nature Geoscience*, **4**(3), 203–207.

Engdahl, E., van der Hilst, R., & Buland, R., 1998. Global teleseismic earthquake relocation with improved travel times and procedures for depth determination, *Bulletin of the Seismological Society of America*, **88**(3), 722–743.

Faure, S., Godey, S., Fallara, F., & Trépanier, S., 2011. Seismic architecture of the Archean North American mantle and its relationship to diamondiferous kimberlite fields, *Economic Geology*, **106**(2), 223–240.

Fichtner, A., Kennett, B., Igel, H., & Bunge, H.-P., 2010. Full waveform tomography for radially anisotropic structure: new insights into present and past states of the Australasian upper mantle, *Earth and Planetary Science Letters*, **290**(3-4), 270–280.

Fishwick, S., 2006. Gradient maps: A tool in the interpretation of tomographic images, *Physics of the earth and planetary interiors*, **156**(1-2), 152–157.

Fishwick, S. & Rawlinson, N., 2012. 3-D structure of the Australian lithosphere from evolving seismic datasets, *Australian Journal of Earth Sciences*, **59**(6), 809–826.

Fishwick, S. & Reading, A., 2008. Anomalous lithosphere beneath the Proterozoic of western and central Australia: a record of continental collision and intraplate deformation?, *Precambrian Research*, **166**(1-4), 111–121.

Fishwick, S., Kennett, B., & Reading, A., 2005. Contrasts in lithospheric structure within the Australian craton—insights from surface wave tomography, *Earth and Planetary Science Letters*, **231**(3-4), 163–176.

Fishwick, S., Heintz, M., Kennett, B., Reading, A., & Yoshizawa, K., 2008. Steps in lithospheric thickness within eastern Australia, evidence from surface wave tomography, *Tectonics*, **27**(4).

Fontaine, F. & Kennet, B., 2007. Soc - Southern Australian Craton.

Fraser, G., McAvaney, S., Neumann, N., Szpunar, M., & Reid, A., 2010. Discovery of early Mesoarchean crust in the eastern Gawler Craton, South Australia, *Precambrian Research*, **179**(1-4), 1–21.

French, S. & Romanowicz, B., 2014. Whole-mantle radially anisotropic shear velocity structure from spectral-element waveform tomography, *Geophysical Journal International*, **199**(3), 1303–1327.

Fukao, Y., Widiyantoro, S., & Obayashi, M., 2001. Stagnant slabs in the upper and lower mantle transition region, *Reviews of Geophysics*, **39**(3), 291–323.

Fukao, Y., Obayashi, M., Nakakuki, T., & Group, D. S. P., 2009. Stagnant slab: a review, *Annual Review of Earth and Planetary Sciences*, **37**, 19–46.

Fullea, J., Lebedev, S., Martinec, Z., & Celli, N., 2021. WINTERC-G: mapping the upper mantle thermo-chemical heterogeneity from coupled geophysical–petrological inversion of seismic waveforms, heat flow, surface elevation and gravity satellite data, *Geophysical Journal International*, **226**(1), 146–191.

Gallais, F., Fujie, G., Boston, B., Hackney, R., Kodaira, S., Miura, S., Nakamura, Y., & Kaiho, Y., 2019. Crustal structure across the Lord Howe Rise, Northern Zealandia, and rifting of the eastern Gondwana margin, *Journal of Geophysical Research: Solid Earth*, **124**(3), 3036–3056.

Garber, J., Maurya, S., Hernandez, J.-A., Duncan, M., Zeng, L., Zhang, H., Faul, U., McCammon, C., Montagner, J.-P., Moresi, L., et al., 2018. Multidisciplinary constraints on the abundance of diamond and eclogite in the cratonic lithosphere, *Geochemistry, Geophysics, Geosystems*, **19**(7), 2062–2086.

Gibbons, A., Barckhausen, U., Van Den Bogaard, P., Hoernle, K., Werner, R., Whittaker, J., & Müller, R., 2012. Constraining the Jurassic extent of greater India: Tectonic evolution of the West Australian margin, *Geochemistry, Geophysics, Geosystems*, **13**(5).

Gibbons, A., Zahirovic, S., Müller, R., Whittaker, J., & Yatheesh, V., 2015. A tectonic model reconciling evidence for the collisions between India, Eurasia and intra-oceanic arcs of the central-eastern Tethys, *Gondwana Research*, **28**(2), 451–492.

Giuliani, A. & Pearson, D., 2019. Kimberlites: from deep earth to diamond mines, *Elements: An International Magazine of Mineralogy, Geochemistry, and Petrology*, **15**(6), 377–380.

Glen, R., 2005. The Tasmanides of eastern Australia, *Special Publication-Geological Society of London*, **246**, 23.

Glen, R., 2013. Refining accretionary orogen models for the Tasmanides of eastern Australia, *Australian Journal of Earth Sciences*, **60**(3), 315–370.

Gordon, R., DeMets, C., & Argus, D., 1990. Kinematic constraints on distributed lithospheric deformation in the equatorial Indian Ocean from present motion between the Australian and Indian plates, *Tectonics*, **9**(3), 409–422.

Griffin, W., O'Reilly, S., & Davies, R., 1998. Subduction-related diamond deposits? Constraints, possibilities, and new data from Eastern Australia, *Reviews in Economic Geology*, **11**, 291–310.

Gunn, P., Milligan, P., Mackey, T., Liu, S., Murray, A., Maidment, D., & Haren, R., 1997. Geophysical mapping using the national airborne and gravity datasets: An example focusing on Broken Hill, *AGSO Journal of Australian Geology and Geophysics*, **17**, 127–136.

Gurnis, M., Van Avendonk, H., Gulick, S., Stock, J., Sutherland, R., Hightower, E., Shuck, B., Patel, J., Williams, E., Kardell, D., et al., 2019. Incipient subduction at the contact with stretched continental crust: The Puysegur Trench, *Earth and Planetary Science Letters*, **520**, 212–219.

Hafkenscheid, E., Buiter, S., Wortel, M., Spakman, W., & Bijwaard, H., 2001. Modelling the seismic velocity structure beneath Indonesia: a comparison with tomography, *Tectonophysics*, **333**(1-2), 35–46.

Hall, R., 1996. Reconstructing Cenozoic SE Asia, *Geological Society, London, Special Publications*, **106**(1), 153–184.

Hall, R., 2002. Cenozoic geological and plate tectonic evolution of SE Asia and the sw Pacific: computer-based reconstructions, model and animations, *Journal of Asian Earth Sciences*, **20**(4), 353–431.

Hall, R., 2011. Australia–SE Asia collision: plate tectonics and crustal flow, *Geological Society, London, Special Publications*, **355**(1), 75–109.

Hall, R. & Spakman, W., 2002. Subducted slabs beneath the eastern Indonesia–Tonga region: insights from tomography, *Earth and Planetary Science Letters*, **201**(2), 321–336.

Hall, R. & Spakman, W., 2003. Mantle structure and tectonic evolution of the region north and east of Australia,

Special Papers-Geological Society of America, pp. 361–382.

Hall, R. & Spakman, W., 2015. Mantle structure and tectonic history of SE Asia, *Tectonophysics*, **658**, 14–45.

Hand, M., Reid, A., Szpunar, M., Direen, N., Wade, B., Payne, J., & Barovich, K., 2008. Crustal architecture during the early Mesoproterozoic Hiltaba-related mineralisation event: are the Gawler Range Volcanics a foreland basin fill?, *MESA Journal*, **51**, 19–24.

Harris, C., Miller, M., Supendi, P., & Widiyantoro, S., 2020. Subducted lithospheric boundary tomographically imaged beneath arc-continent collision in Eastern Indonesia, *Journal of Geophysical Research: Solid Earth*, **125**(8), e2019JB018854.

Hawkins Jr, J. & Natland, J., 1975. Nephelinites and basanites of the Samoan linear volcanic chain: Their possible tectonic significance, *Earth and Planetary Science Letters*, **24**(3), 427–439.

Haynes, M., Czarnota, K., Gorbatov, A., Afonso, R., Fomin, I., & Salajegheh, F., 2020. *Developing Thermochemical Models of Australia's Lithosphere*, Geoscience Australia.

Heintz, M. & Kennett, B., 2006. The apparently isotropic Australian upper mantle, *Geophysical Research Letters*, **33**(15).

Hill, D., 1951. Geology in Handbook of Queensland, 13-24, *Aust. NZ Ass. Advmt Sci., Brisbane*.

Hoggard, M., Czarnota, K., Richards, F., Huston, D., Jaques, A., & Ghelichkhan, S., 2020. Global distribution of sediment-hosted metals controlled by craton edge stability, *Nature Geoscience*, **13**(7), 504–510.

Holm, R., Spandler, C., & Richards, S., 2015. Continental collision, orogenesis and arc magmatism of the Miocene Maramuni arc, Papua New Guinea, *Gondwana Research*, **28**(3), 1117–1136.

Huston, D., Blewett, R., & Champion, D., 2012. Australia through time: a summary of its tectonic and metallogenic evolution, *Episodes Journal of International Geoscience*, **35**(1), 23–43.

Hutchings, S. & Mooney, W., 2021. The seismicity of Indonesia and tectonic implications, *Geochemistry, Geophysics, Geosystems*, **22**(9), e2021GC009812.

Jaques, A. & Milligan, P., 2004. Patterns and controls on the distribution of diamondiferous intrusions in Australia, *Lithos*, **77**(1-4), 783–802.

Johnson, R., Johnson, R., Knutson, J., & Taylor, S., 1989. *Intraplate volcanism: in eastern Australia and New Zealand*, Cambridge University Press.

Jones, I. & Verdel, C., 2015. Basalt distribution and volume estimates of Cenozoic volcanism in the Bowen Basin region of eastern Australia: Implications for a waning mantle plume, *Australian Journal of Earth Sciences*, **62**(2), 255–263.

Karato, S.-I., 1993. Importance of anelasticity in the interpretation of seismic tomography, *Geophysical research letters*, **20**(15), 1623–1626.

Karato, S.-I., 2012. On the origin of the asthenosphere, *Earth and Planetary Science Letters*, **321**, 95–103.

Karato, S.-I. & Jung, H., 1998. Water, partial melting and the origin of the seismic low velocity and high attenuation zone in the upper mantle, *Earth and Planetary Science Letters*, **157**(3-4), 193–207.

Keating, B., Mattey, D., Helsley, C., Naughton, J., Epp, D., Lazarewicz, A., & Schwank, D., 1984. Evidence for a hot spot origin of the Caroline Islands, *Journal of Geophysical Research: Solid Earth*, **89**(B12), 9937–9948.

Kennet, B., 2000. West Australian Cratons.

Kennett, B., 1998. Kimba98, http://www.fdsn.org/doi/10.7914/SN/7E$_1$998.

Kennett, B. & Blewett, R., 2012. Lithospheric framework of Australia, *Episodes*, **35**(1), 9–22.

Kennett, B., Engdahl, E., & Buland, R., 1995. Constraints on seismic velocities in the Earth from traveltimes, *Geophysical Journal International*, **122**(1), 108–124.

Kennett, B., Fishwick, S., Reading, A., & Rawlinson, N., 2004. Contrasts in mantle structure beneath Australia: relation to Tasman lines?, *Australian Journal of Earth Sciences*, **51**(4), 563–569.

Kennett, B., Fichtner, A., Fishwick, S., & Yoshizawa, K., 2013. Australian seismological reference model (AuSREM): mantle component, *Geophysical Journal International*, **192**(2), 871–887.

Klingelhoefer, F., Lafoy, Y., Collot, J., Cosquer, E., Geli, L., Nouze, H., & Vially, R., 2007. Crustal structure of the basin and ridge system west of New Caledonia (southwest Pacific) from wide-angle and reflection seismic data, *Journal of Geophysical Research: Solid Earth*, **112**(B11).

Knesel, K., Cohen, B., Vasconcelos, P., & Thiede, D., 2008. Rapid change in drift of the Australian plate records collision with Ontong Java plateau, *Nature*, **454**(7205), 754–757.

Koppers, A., Russell, J., Jackson, M., Konter, J., Staudigel, H., & Hart, S., 2008. Samoa reinstated as a primary hotspot trail, *Geology*, **36**(6), 435–438.

Kreemer, C., Holt, W., Goes, S., & Govers, R., 2000. Active deformation in eastern Indonesia and the Philippines from GPS and seismicity data, *Journal of Geophysical Research: Solid Earth*, **105**(B1), 663–680.

Kusky, T., Windley, B., Wang, L., Wang, Z., Li, X., & Zhu, P., 2014. Flat slab subduction, trench suction, and craton destruction: Comparison of the North China, Wyoming, and Brazilian cratons, *Tectonophysics*, **630**, 208–221.

Lebedev, S. & Nolet, G., 2003. Upper mantle beneath Southeast Asia from S velocity tomography, *Journal of Geophysical Research: Solid Earth*, **108**(B1).

Lebedev, S. & Van Der Hilst, R., 2008. Global upper-mantle tomography with the automated multimode inversion of surface and S-wave forms, *Geophysical Journal International*, **173**(2), 505–518.

Lebedev, S., Nolet, G., & Van Der Hilst, R., 1997. The upper mantle beneath the Philippine Sea region from waveform inversions, *Geophysical research letters*, **24**(15), 1851–1854.

Lebedev, S., Nolet, G., Meier, T., & Van Der Hilst, R., 2005. Automated multimode inversion of surface and S waveforms, *Geophysical Journal International*, **162**(3), 951–964.

Lebedev, S., Boonen, J., & Trampert, J., 2009. Seismic structure of Precambrian lithosphere: new constraints from broad-band surface-wave dispersion, *Lithos*, **109**(1-2), 96–111.

Li, C., van der Hilst, R., Engdahl, E., & Burdick, S., 2008. A new global model for P wave speed variations in Earth's mantle, *Geochemistry, Geophysics, Geosystems*, **9**(5).

Long, M. & Silver, P., 2009. Mantle flow in subduction systems: The subslab flow field and implications for mantle dynamics, *Journal of Geophysical Research: Solid Earth*, **114**(B10).

Lu, C., Grand, S., Lai, H., & Garnero, E., 2019. TX2019slab: A new P and S tomography model incorporating subducting slabs, *Journal of Geophysical Research: Solid Earth*, **124**(11), 11549–11567.

Masters, G., Laske, G., Bolton, H., & Dziewonski, A., 2000. The relative behavior of shear velocity, bulk sound speed, and compressional velocity in the mantle: Implications for chemical and thermal structure, *Washington DC American Geophysical Union Geophysical Monograph Series*, **117**, 63–87.

Mather, B., Müller, R., Seton, M., Ruttor, S., Nebel, O., & Mortimer, N., 2020. Intraplate volcanism triggered by bursts in slab flux, *Science Advances*, **6**(51).

Matthews, K., Maloney, K., Zahirovic, S., Williams, S., Seton, M., & Mueller, R., 2016. Global plate boundary evolution and kinematics since the late Paleozoic, *Global and Planetary Change*, **146**, 226–250.

McDougall, I. & Duncan, R., 1988. Age progressive volcanism in the Tasmantid Seamounts, *Earth and Planetary Science Letters*, **89**(2), 207–220.

McInnes, B., Evans, N., Jourdan, F., Mcdonald, B., Danišík, M., Gorter, J., & Mayers, C., 2012. Zircon U-Th-Pb-He double-dating of north Australian diamond fields: Ellendale (WA), Seppelt (WA) and Merlin (NT), in *International Kimberlite Conference: Extended Abstracts*, vol. 10.

McKenzie, D. & Priestley, K., 2008. The influence of lithospheric thickness variations on continental evolution, *Lithos*, **102**(1-2), 1–11.

McKenzie, D., Jackson, J., & Priestley, K., 2005. Thermal structure of oceanic and continental lithosphere, *Earth and Planetary Science Letters*, **233**(3-4), 337–349.

Meier, T., Dietrich, K., Stöckhert, B., & Harjes, H.-P., 2004. One-dimensional models of shear wave velocity for the eastern Mediterranean obtained from the inversion of Rayleigh wave phase velocities and tectonic implications, *Geophysical Journal International*, **156**(1), 45–58.

Menzies, M., Fan, W., & Zhang, M., 1993. Palaeozoic and Cenozoic lithoprobes and the loss of¿ 120 km of Archaean lithosphere, Sino-Korean craton, China, *Geological Society, London, Special Publications*, **76**(1), 71–81.

Metcalfe, I., 2013. Gondwana dispersion and Asian accretion: Tectonic and palaeogeographic evolution of eastern Tethys, *Journal of Asian Earth Sciences*, **66**, 1–33.

Mojzsis, S., Harrison, T., & Pidgeon, R., 2001. Oxygen-isotope evidence from ancient zircons for liquid water at the Earth's surface 4,300 Myr ago, *Nature*, **409**(6817), 178–181.

Montelli, R., Nolet, G., Dahlen, F., Masters, G., Engdahl, E., & Hung, S.-H., 2004. Finite-frequency tomography reveals a variety of plumes in the mantle, *Science*, **303**(5656), 338–343.

Montelli, R., Nolet, G., Dahlen, F., & Masters, G., 2006. A catalogue of deep mantle plumes: New results from finite-frequency tomography, *Geochemistry, Geophysics, Geosystems*, **7**(11).

Moresi, L., Betts, P., Miller, M., & Cayley, R., 2014. Dynamics of continental accretion, *Nature*, **508**(7495), 245–248.

Morgan, W., 1971. Convection plumes in the lower mantle, *Nature*, **230**(5288), 42–43.

Mortimer, N., Campbell, H., Tulloch, A., King, P., Stagpoole, V. M., Wood, R., Rattenbury, M., Sutherland, R., Adams, C., Collot, J., et al., 2017. Zealandia: Earth's hidden continent, *GSA today*, **27**(3), 27–35.

Müller, R., Sdrolias, M., Gaina, C., & Roest, W., 2008. Age, spreading rates, and spreading asymmetry of the world's ocean crust, *Geochemistry, Geophysics, Geosystems*, **9**(4).

Müller, R., Seton, M., Zahirovic, S., Williams, S., Matthews, K., Wright, N., Shephard, G., Maloney, K., Barnett-Moore, N., Hosseinpour, M., et al., 2016. Ocean basin evolution and global-scale plate reorganization events since Pangea breakup, *Annual Review of Earth and Planetary Sciences*, **44**, 107–138.

Müller, R., Zahirovic, S., Williams, S., Cannon, J., Seton, M., Bower, D., Tetley, M., Heine, C., Le Breton, E., Liu, S., et al., 2019. A global plate model including lithospheric deformation along major rifts and orogens since the Triassic, *Tectonics*, **38**(6), 1884–1907.

Mutter, J., Hegarty, K., Cande, S., & Weissel, J., 1985. Breakup between Australia and Antarctica: a brief review in the light of new data, *Tectonophysics*, **114**(1-4), 255–279.

Myers, J., Shaw, R., & Tyler, I., 1996. Tectonic evolution of proterozoic Australia, *Tectonics*, **15**(6), 1431–1446.

Nolet, G., 1990. Partitioned waveform inversion and two-dimensional structure under the network of autonomously recording seismographs, *Journal of Geophysical Research: Solid Earth*, **95**(B6), 8499–8512.

O'Neill, C., Moresi, L., & Jaques, A., 2005. Geodynamic controls on diamond deposits: implications for Australian occurrences, *Tectonophysics*, **404**(3-4), 217–236.

Page, R., Conor, C., Stevens, B., Gibson, G., Preiss, W., & Southgate, P., 2005. Correlation of Olary and Broken Hill domains, Curnamona Province: Possible relationship to Mount Isa and other North Australian Pb-Zn-Ag-bearing successions, *Economic Geology*, **100**(4), 663–676.

Park, J. & Levin, V., 2002. Seismic anisotropy: tracing plate dynamics in the mantle, *Science*, **296**(5567), 485–489.

Pearson, D., Canil, D., & Shirey, S., 2003. Mantle samples included in volcanic rocks: xenoliths and diamonds, *Treatise on geochemistry*, **2**, 568.

Petersen, T., Gledhill, K., Chadwick, M., Gale, N., & Ristau, J., 2011. The New Zealand national seismograph network, *Seismological Research Letters*, **82**(1), 9–20.

Pirajno, F. & Bagas, L., 2008. A review of Australia's Proterozoic mineral systems and genetic models, *Precambrian Research*, **166**(1-4), 54–80.

Priestley, K., McKenzie, D., & Ho, T., 2018. A lithosphere–asthenosphere boundary—A global model derived from multimode surface-wave tomography and petrology, *Lithospheric discontinuities*, pp. 111–123.

Ravenna, M., Lebedev, S., Fullea, J., & Adam, J.-C., 2018. Shear-wave velocity structure of Southern Africa's lithosphere: Variations in the thickness and composition of cratons and their effect on topography, *Geochemistry, Geophysics, Geosystems*, **19**(5), 1499–1518.

Rawlinson, N., Kennett, B., Salmon, M., & Glen, R., 2015. Origin of lateral heterogeneities in the upper mantle beneath south-east Australia from seismic tomography, in *The Earth's Heterogeneous Mantle*, pp. 47–78, Springer.

Rawlinson, N., Pilia, S., Young, M., Salmon, M., & Yang, Y., 2016. Crust and upper mantle structure beneath southeast Australia from ambient noise and teleseismic tomography, *Tectonophysics*, **689**, 143–156.

Rawlinson, N., Davies, D., & Pilia, S., 2017. The mechanisms underpinning Cenozoic intraplate volcanism in eastern Australia: insights from seismic tomography and geodynamic modeling, *Geophysical Research Letters*, **44**(19), 9681–9690.

Rawlinson, S. & Kennet, B., 2008. Bilby - Australian Cratonic lithosphere.

Reading, A. & Kennett, B., 2005. Capra - linkage.

Reading, A., Rawlinson, N., et al., 2013. Bass: Seismic deployments across the Bass Strait from 2011 to 2013.

Ritsema, J., Deuss, A., Van Heijst, H., & Woodhouse, J., 2011. S40RTS: a degree-40 shear-velocity model for the mantle from new Rayleigh wave dispersion, teleseismic traveltime and normal-mode splitting function measurements, *Geophysical Journal International*, **184**(3), 1223–1236.

Rosenbaum, G., 2018. The Tasmanides: Phanerozoic tectonic evolution of eastern Australia, *Annual Review of Earth and Planetary Sciences*, **46**, 291–325.

Salmon, M., Kennett, B., & Saygin, E., 2013a. Australian seismological reference model (AuSREM): crustal component, *Geophysical Journal International*, **192**(1), 190–206.

Salmon, M., Kennett, B., Stern, T., & Aitken, A., 2013b. The moho in Australia and New Zealand, *Tectonophysics*, **609**, 288–298.

Sato, Y., 1955. Analysis of dispersed surface waves by means of Fourier transform i, *Bull. Earthq. Res. Inst*, **33**, 33–48.

Schaeffer, A. & Lebedev, S., 2013. Global shear speed structure of the upper mantle and transition zone, *Geophysical Journal International*, **194**(1), 417–449.

Schaeffer, A. & Lebedev, S., 2014. Imaging the North American continent using waveform inversion of global and USArray data, *Earth and Planetary Science Letters*, **402**, 26–41.

Schaeffer, A. & Lebedev, S., 2015. Global heterogeneity of the lithosphere and underlying mantle: A seismological appraisal based on multimode surface-wave dispersion analysis, shear-velocity tomography, and tectonic regionalization, *The earth's heterogeneous mantle: A geophysical, geodynamical, and geochemical perspective*, pp. 3–46.

Schaeffer, A., Lebedev, S., & Becker, T., 2016. Azimuthal seismic anisotropy in the Earth's upper mantle and the thickness of tectonic plates, *Geophysical Supplements to the Monthly Notices of the Royal Astronomical Society*, **207**(2), 901–933.

Scheibner, E. & Veevers, J., 2000. Tasman fold belt system, in *Billion-year earth history of Australia and neighbours in Gondwanaland*, pp. 154–234, Gemoc Press.

Schellart, W. & Spakman, W., 2015. Australian plate motion and topography linked to fossil New Guinea slab below Lake Eyre, *Earth and Planetary Science Letters*, **421**, 107–116.

Schellart, W., Lister, G., & Toy, V., 2006. A late cretaceous and Cenozoic reconstruction of the Southwest Pacific region: Tectonics controlled by subduction and slab rollback processes, *Earth-Science Reviews*, **76**(3-4), 191–233.

Seton, M., Müller, R., Zahirovic, S., Gaina, C., Torsvik, T., Shephard, G., Talsma, A., Gurnis, M., Turner, M., Maus, S., et al., 2012. Global continental and ocean basin reconstructions since 200 Ma, *Earth-Science Reviews*, **113**(3-4), 212–270.

Seton, M., Williams, S., Mortimer, N., Meffre, S., Micklethwaite, S., & Zahirovic, S., 2019. Magma production along the Lord Howe Seamount Chain, northern Zealandia, *Geological Magazine*, **156**(9), 1605–1617.

Shaw, R., Wellman, P., Gunn, P., Whitaker, A., Tarlowski, C., & Morse, M., 1995. Australian crustal elements map, *AGSO Res. Newslett*, **23**, 1–3.

Simmons, N., Myers, S., Johannesson, G., & Matzel, E., 2012. LLNL-G3Dv3: Global P wave tomography model for improved regional and teleseismic travel time prediction, *Journal of Geophysical Research: Solid Earth*, **117**(B10).

Simons, F., Zielhuis, A., & Van Der Hilst, R., 1999. The deep structure of the Australian continent from surface wave tomography, in *Developments in Geotectonics*, vol. 24, pp. 17–43, Elsevier.

Simons, F., Van Der Hilst, R., Montagner, J.-P., & Zielhuis, A., 2002. Multimode Rayleigh wave inversion for heterogeneity and azimuthal anisotropy of the Australian upper mantle, *Geophysical Journal International*, **151**(3), 738–754.

Sleep, N., 1990. Hotspots and mantle plumes: Some phenomenology, *Journal of Geophysical Research: Solid Earth*, **95**(B5), 6715–6736.

Sobolev, S., Zeyen, H., Stoll, G., Werling, F., Altherr, R., & Fuchs, K., 1996. Upper mantle temperatures from teleseismic tomography of french Massif Central including effects of composition, mineral reactions, anharmonicity, anelasticity and partial melt, *Earth and Planetary Science Letters*, **139**(1-2), 147–163.

Sobolev, S., Sobolev, A., Kuzmin, D., Krivolutskaya, N., Petrunin, A., Arndt, N., Radko, V., & Vasiliev, Y., 2011. Linking mantle plumes, large igneous provinces and environmental catastrophes, *Nature*, **477**(7364), 312–316.

Soomro, R., Weidle, C., Cristiano, L., Lebedev, S., Meier, T., & Group, P. W., 2016. Phase velocities of Rayleigh and Love waves in central and northern Europe from automated, broad-band, interstation measurements, *Geophysical Journal International*, **204**(1), 517–534.

Spakman, W. & Hall, R., 2010. Surface deformation and slab–mantle interaction during Banda arc subduction rollback, *Nature Geoscience*, **3**(8), 562–566.

Sun, W. & Kennett, B., 2016. Uppermost mantle structure of the Australian continent from pn traveltime tomography, *Journal of Geophysical Research: solid earth*, **121**(3), 2004–2019.

Supendi, P., Nugraha, A., Widiyantoro, S., Abdullah, C., Rawlinson, N., Cummins, P., Harris, C., Roosmawati, N., & Miller, M., 2020. Fate of forearc lithosphere at arc-continent collision zones: Evidence from local earthquake tomography of the Sunda-Banda arc transition, Indonesia, *Geophysical Research Letters*, **47**(6), e2019GL086472.

Sutherland, F., 2003. eastern Australian rift margins and the Indian-Pacific mantle boundary, *Evolution and dynamics of the Australian Plate*, **372**, 203.

Sutherland, F., Graham, I., Meffre, S., Zwingmann, H., & Pogson, R., 2012. Passive-margin prolonged volcanism, East Australian plate: outbursts, progressions, plate controls and suggested causes, *Australian Journal of Earth Sciences*, **59**(7), 983–1005.

Sutherland, R., 1999. Basement geology and tectonic development of the greater New Zealand region: an interpretation from regional magnetic data, *Tectonophysics*, **308**(3), 341–362.

Sutherland, R., Collot, J., Lafoy, Y., Logan, G., Hackney, R., Stagpoole, V., Uruski, C., Hashimoto, T., Higgins, K., Herzer, R., et al., 2010. Lithosphere delamination with foundering of lower crust and mantle caused perma-

nent subsidence of New Caledonia Trough and transient uplift of Lord Howe Rise during Eocene and Oligocene initiation of Tonga-Kermadec subduction, western Pacific, *Tectonics*, **29**(2).

Tang, Q. & Zheng, C., 2013. Crust and upper mantle structure and its tectonic implications in the South China Sea and adjacent regions, *Journal of Asian Earth Sciences*, **62**, 510–525.

Taylor, B. & Hayes, D., 1983. Origin and history of the South China Sea basin, *Washington DC American Geophysical Union Geophysical Monograph Series*, **27**, 23–56.

Thorne, M., Garnero, E., Jahnke, G., Igel, H., & McNamara, A., 2013. Mega ultra low velocity zone and mantle flow, *Earth and Planetary Science Letters*, **364**, 59–67.

Thurber, C. & Townend, J., 2016. Seismic triggering response for Earthquakes around Wellington NZ.

Tregoning, P., Brunner, F., Bock, Y., Puntodewo, S., McCaffrey, R., Genrich, J., Calais, E., Rais, J., & Subarya, C., 1994. First geodetic measurement of convergence across the Java Trench, *Geophysical Research Letters*, **21**(19), 2135–2138.

Tulloch, A., Mortimer, N., Ireland, T., Waight, T., Maas, R., Palin, J., Sahoo, T., Seebeck, H., Sagar, M., Barrier, A., et al., 2019. Reconnaissance basement geology and tectonics of South Zealandia, *Tectonics*, **38**(2), 516–551.

Tychkov, S., Rychkova, E., & Vasilevskii, A., 1998. Interaction between a plume and thermal convection in the continental upper mantle, *RUSSIAN GEOLOGY AND GEOPHYSICS C/C OF GEOLOGIIA I GEOFIZIKA*, **39**, 423–434.

Tyler, I. & Griffin, T., 1990. Structural development of the King Leopold Orogen, Kimberly region, Western Australia, *Journal of Structural Geology*, **12**(5-6), 703–714.

van de Lagemaat, S., Van Hinsbergen, D., Boschman, L., Kamp, P., & Spakman, W., 2018. Southwest Pacific absolute plate kinematic reconstruction reveals major Cenozoic Tonga-Kermadec slab dragging, *Tectonics*, **37**(8), 2647–2674.

van der Hilst, R., 1995. Complex morphology of subducted lithosphere in the mantle beneath the Tonga trench, *Nature*, **374**(6518), 154–157.

van der Hilst, R., Kennett, B., Christie, D., & Grant, J., 1994. Project skippy explores lithosphere and mantle beneath Australia, *EOS, Transactions American Geophysical Union*, **75**(15), 177–181.

Van der Meer, D., Van Hinsbergen, D., & Spakman, W., 2018. Atlas of the underworld: Slab remnants in the mantle, their sinking history, and a new outlook on lower mantle viscosity, *Tectonophysics*, **723**, 309–448.

van Mierlo, W., Langenhorst, F., Frost, D., & Rubie, D., 2013. Stagnation of subducting slabs in the transition zone due to slow diffusion in majoritic garnet, *Nature Geoscience*, **6**(5), 400–403.

van Ufford, A. & Cloos, M., 2005. Cenozoic tectonics of New Guinea, *AAPG bulletin*, **89**(1), 119–140.

Vasconcelos, P., Knesel, K., Cohen, B., & Heim, J., 2008. Geochronology of the Australian Cenozoic: a history of tectonic and igneous activity, weathering, erosion, and sedimentation, *Australian Journal of Earth Sciences*, **55**(6-7), 865–914.

Veevers, J. & Powel, C. M., 1984. Epi-Adelaidean: regional shear. in: Veevers j. j. ed. Phanerozoic Earth history of Australia, p. 278–284.

Vogt, P. & Conolly, J., 1971. Tasmantid Guyots, the age of the Tasman Basin, and motion between the Australia

plate and the mantle, *Geological Society of America Bulletin*, **82**(9), 2577–2584.

Walsh, J., 1969. New analysis of attenuation in partially melted rock, *Journal of Geophysical Research*, **74**(17), 4333–4337.

Wehner, D., Blom, N., Rawlinson, N., Böhm, C., Miller, M., Supendi, P., & Widiyantoro, S., 2022. SASSY21: A 3-D seismic structural model of the lithosphere and underlying mantle beneath Southeast Asia from multi-scale adjoint waveform tomography, *Journal of Geophysical Research: Solid Earth*, p. e2021JB022930.

Wellman, P. & McDougall, I., 1974. Cainozoic igneous activity in eastern Australia, *Tectonophysics*, **23**(1-2), 49–65.

Wenker, S. & Beaumont, C., 2018. Can metasomatic weakening result in the rifting of cratons?, *Tectonophysics*, **746**, 3–21.

Wessel, P. & Smith, W., 1995. New version of the generic mapping tools, *Eos, Transactions American Geophysical Union*, **76**(33), 329–329.

Whittaker, J., Afonso, J., Masterton, S., Müller, R., Wessel, P., Williams, S., & Seton, M., 2015. Long-term interaction between mid-ocean ridges and mantle plumes, *Nature Geoscience*, **8**(6), 479–483.

Widiyantoro, S. & van der Hilst, R., 1996. Structure and evolution of lithospheric slab beneath the Sunda arc, Indonesia, *Science*, **271**(5255), 1566–1570.

Widiyantoro, S., Pesicek, J., & Thurber, C., 2011. Subducting slab structure below the eastern Sunda arc inferred from non-linear seismic tomographic imaging, *Geological Society, London, Special Publications*, **355**(1), 139–155.

Wiens, D., DeMets, C., Gordon, R., Stein, S., Argus, D., Engeln, J., Lundgren, P., Quible, D., Stein, C., Weinstein, S., et al., 1985. A diffuse plate boundary model for Indian Ocean tectonics, *Geophysical Research Letters*, **12**(7), 429–432.

Wilson, J., 1963. A possible origin of the Hawaiian Islands, *Canadian Journal of Physics*, **41**(6), 863–870.

Wingate, M. & Giddings, J., 2000. Age and palaeomagnetism of the Mundine Well dyke swarm, Western Australia: implications for an Australia–Laurentia connection at 755 Ma, *Precambrian Research*, **100**(1-3), 335–357.

Wu, J., Suppe, J., Lu, R., & Kanda, R., 2016. Philippine Sea and East Asian plate tectonics since 52 Ma constrained by new subducted slab reconstruction methods, *Journal of Geophysical Research: Solid Earth*, **121**(6), 4670–4741.

Yoshizawa, K., 2014. Radially anisotropic 3-D shear wave structure of the Australian lithosphere and asthenosphere from multi-mode surface waves, *Physics of the Earth and Planetary Interiors*, **235**, 33–48.

Yoshizawa, K. & Kennett, B., 2004. Multimode surface wave tomography for the Australian region using a three-stage approach incorporating finite frequency effects, *Journal of Geophysical Research: Solid Earth*, **109**(B2).

Yuan, H. & Romanowicz, B., 2010. Lithospheric layering in the North American craton, *Nature*, **466**(7310), 1063–1068.

Zahirovic, S., Matthews, K., Flament, N., Müller, R., Hill, K., Seton, M., & Gurnis, M., 2016. Tectonic evolution and deep mantle structure of the eastern Tethys since the latest Jurassic, *Earth-Science Reviews*, **162**, 293–337.

Zandt, G. & Humphreys, E., 2008. Toroidal mantle flow through the western US slab window, *Geology*, **36**(4), 295–298.

Zenonos, A., De Siena, L., Widiyantoro, S., & Rawlinson, N., 2019. P and S wave travel time tomography of the SE Asia-Australia collision zone, *Physics of the Earth and Planetary Interiors*, **293**, 106267.

Zhang, X., Paulssen, H., Lebedev, S., & Meier, T., 2009. 3D shear velocity structure beneath the Gulf of California from Rayleigh wave dispersion, *Earth and Planetary Science Letters*, **279**(3-4), 255–262.

Zhao, D., 2007. Seismic images under 60 hotspots: search for mantle plumes, *Gondwana Research*, **12**(4), 335–355.

Zielhuis, A. & van der Hilst, R., 1996. Upper-mantle shear velocity beneath eastern Australia from inversion of waveforms from skippy portable arrays, *Geophysical Journal International*, **127**(1), 1–16.

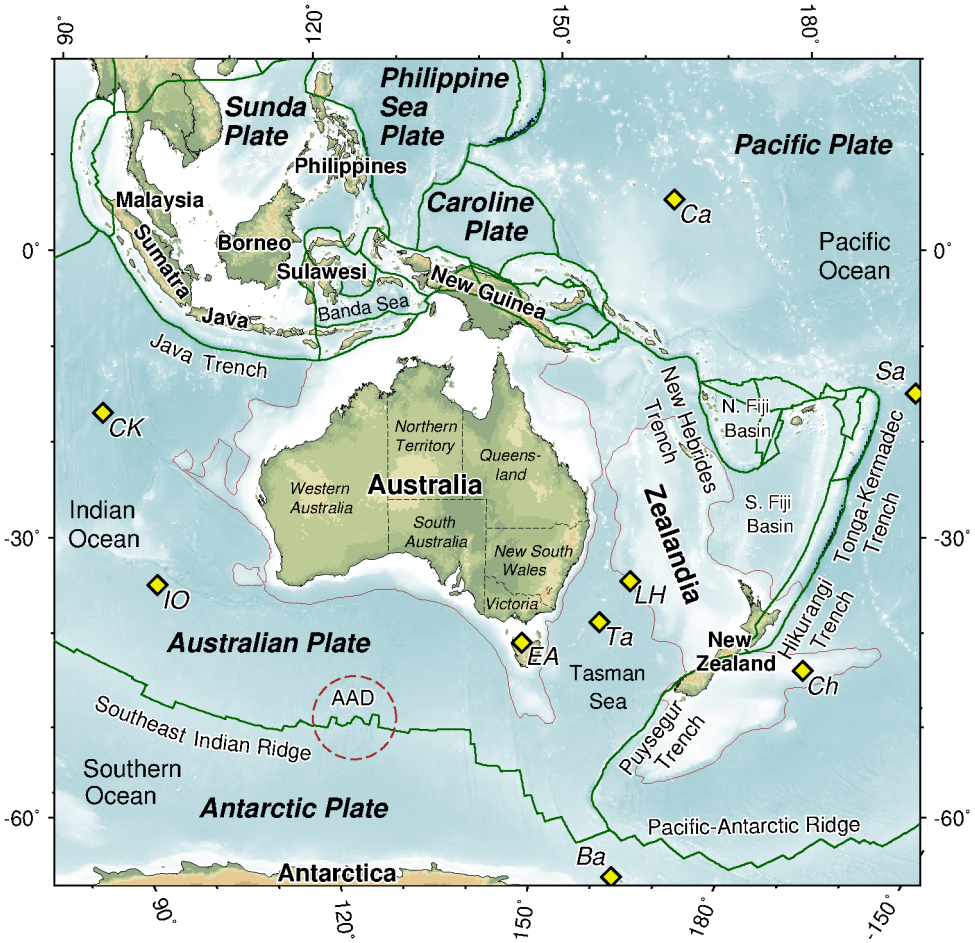

Figure 1. The Australian Plate and surrounding areas. Plate boundaries are plotted in green, and the continental crust boundary in brown (based on bathymetry). AAD = Antarctic-Australian Discordance. Hotspot as identified by Whittaker et al. (2015) are plotted as yellow diamonds. Ba= Balleny, C1 & C2 = Caroline 1 & 2, CK=Cocos-Keeling, Ch = Chatam, EA = East Australia, IO = Indian Ocean, LH = Lord Howe, Sa = Samoa, Ta = Tasmantid.

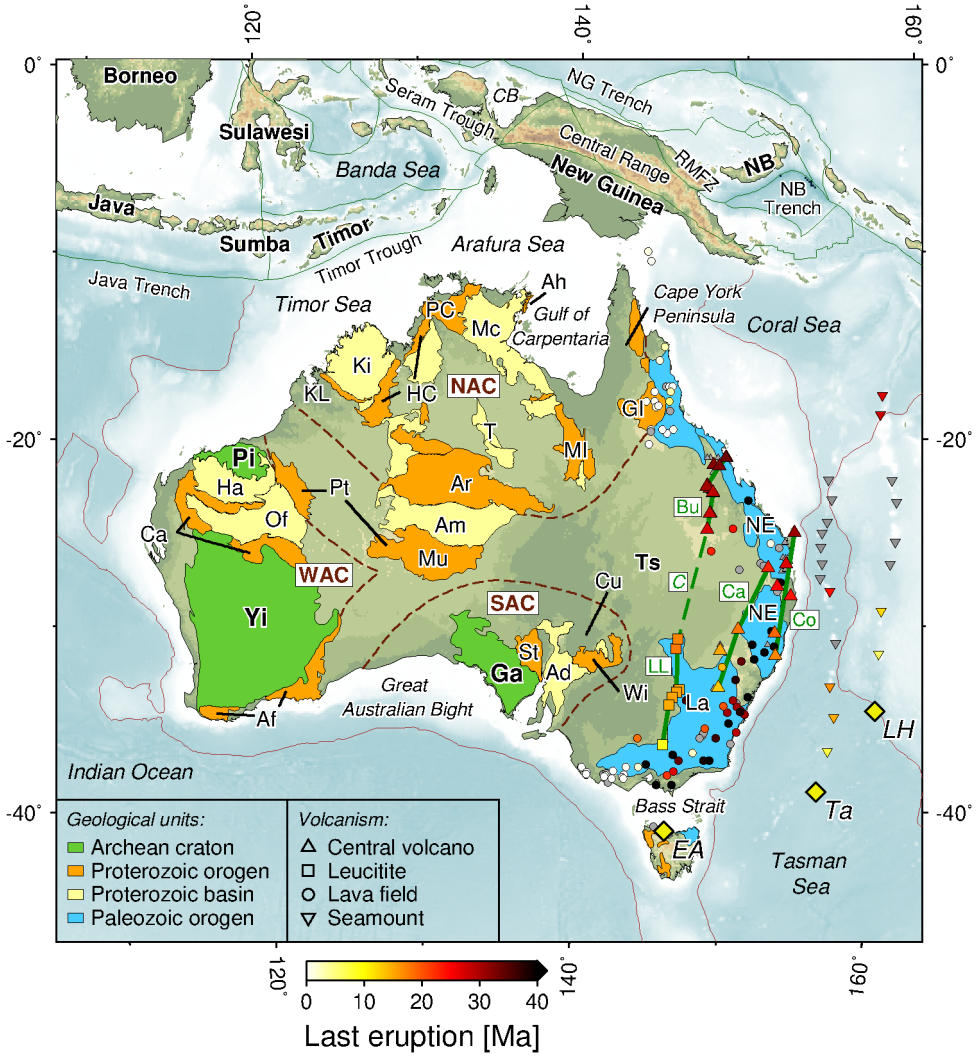

Figure 2. Tectonic map of the Australian continent. The dotted lines show the boundaries of the main cratonic provinces in Australia as defined by Blewett et al. (2012). NAC= North Australian Craton, WAC = West Australian Craton, SAC= South Australian Craton. The geological units are plotted based on the outlines of Kennett & Blewett (2012) and Pirajno & Bagas (2008). Ad=Adelaide Basin, Af=Albany-Fraser Orogen, Am=Amadeus Basin, Ah=Arnhem Province, Ar=Arunta Block, Ca=Canning Basin, Cu=Curnamona Craton, Ga=Gawler Craton, GI=Georgetown Inlier, Ha=Hamerley Basin, HC=Halls Creek Orogen, Ki=Kimberley Block, KL=King Leopold Orogen, La=Lachlan Orogen, Mc=MacArthur Basin, MI=Mt Isa Inlier, Mu=Musgrave Orogen, NE=New England Orogen, Of=Officer Basin, PC=Pince Creek Inlier, Pi=Pilbara Craton, Pt=Paterson Orogen, St=Stuart Orogen, T=Tennant Creek Inlier, Ts=Tasmanides, Wi=Willyama Orogen, Yi=Yilgarn Craton. Green lines give the age-progressive volcanic tracks, following Knesel et al. (2008); Sutherland et al. (2012); Cohen et al. (2013). Bu = Buckland, Ca = Canobolas, Co = Comboyne, LL = Leucitite Line. C = Cosgrove (combines the Buckland track and Leucitite Line, Davies et al. (2015)). CB = Cendrawasih Basin, NB = New Britain.

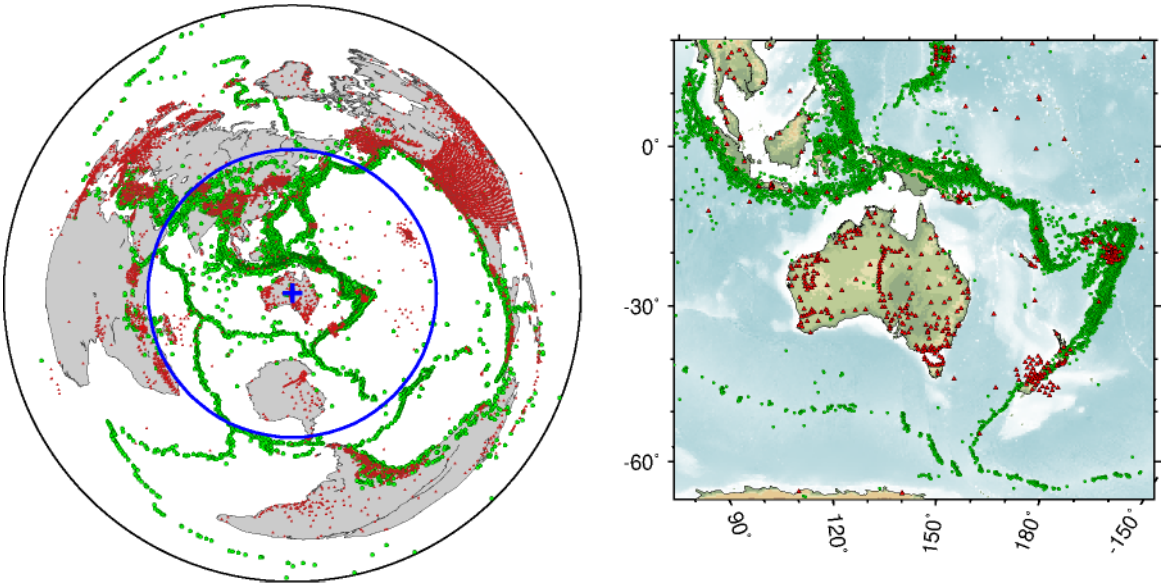

Figure 3. Global map showing all the stations (red triangles) and events (green circles) that produced the seismograms in our hemisphere-focussed global dataset. The hemisphere is centred at the centre of the Australian continent (blue cross) and covers an area with a 90 degree radius (blue circle). Only seismograms with the source, the receiver or both the source and the receiver located within the hemisphere are used to constrain the model. Right: stations and events in our dataset situated in the Australian Plate and surrounding areas. In total, the dataset includes over 9 thousand stations and over 26 thousand events from 1994 to 2018. Only the stations and events that produced successful AMI waveform fits are plotted.

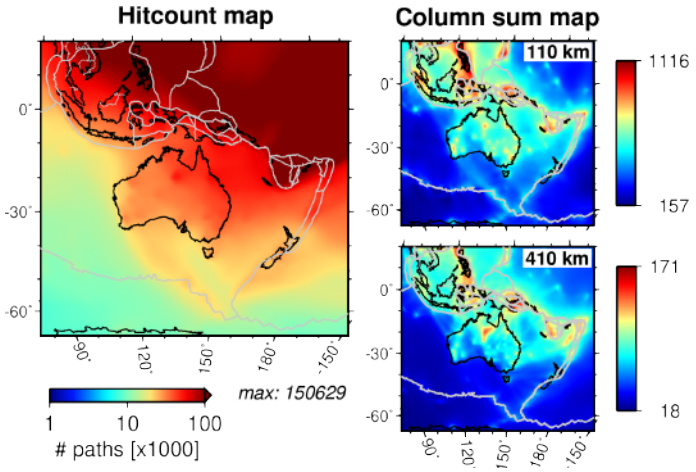

Figure 4. Density of the data sampling of the region computed as the hit count at every model-grid node of the model (left) and as the sum of the columns of the sensitivity matrix at every model-grid node, at two different depths (right).

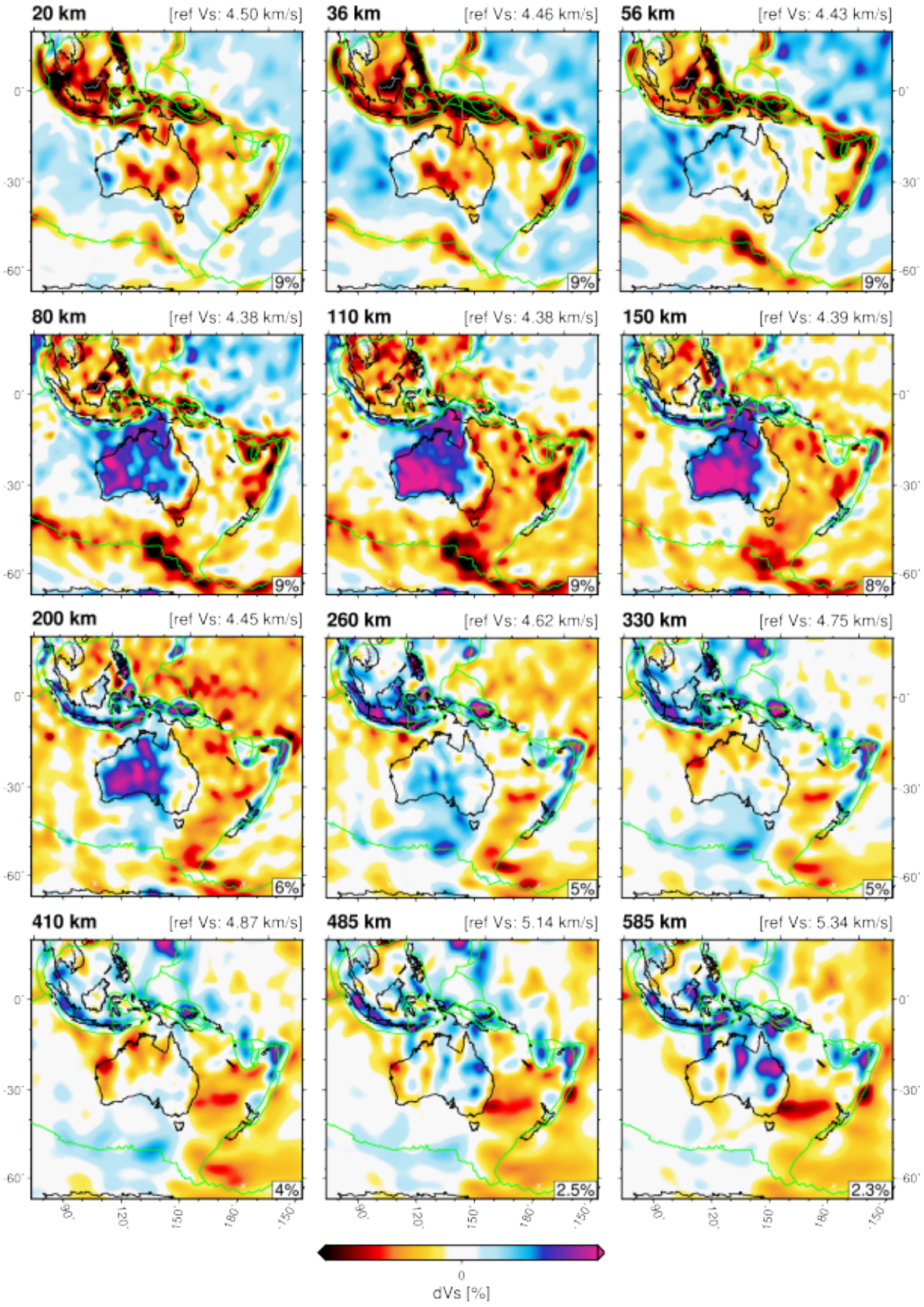

Figure 5. Map view of *Aus22* S-wave velocity anomalies at 12 different depths. The velocity anomalies are plotted relative to the reference value at each depth, taken from the reference model of the tomographic inversion and indicated above each frame. The colour scale limit varies with depth and is given at the bottom right in each frame. Plate boundaries are shown with green lines.

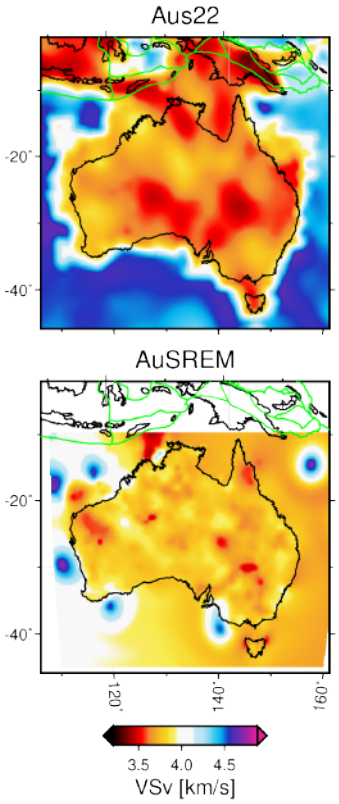

Figure 6. Absolute S-wave velocity at 20 km depth according to *Aus22* (top) and to AuSREM (bottom, Kennett et al. (2013)).

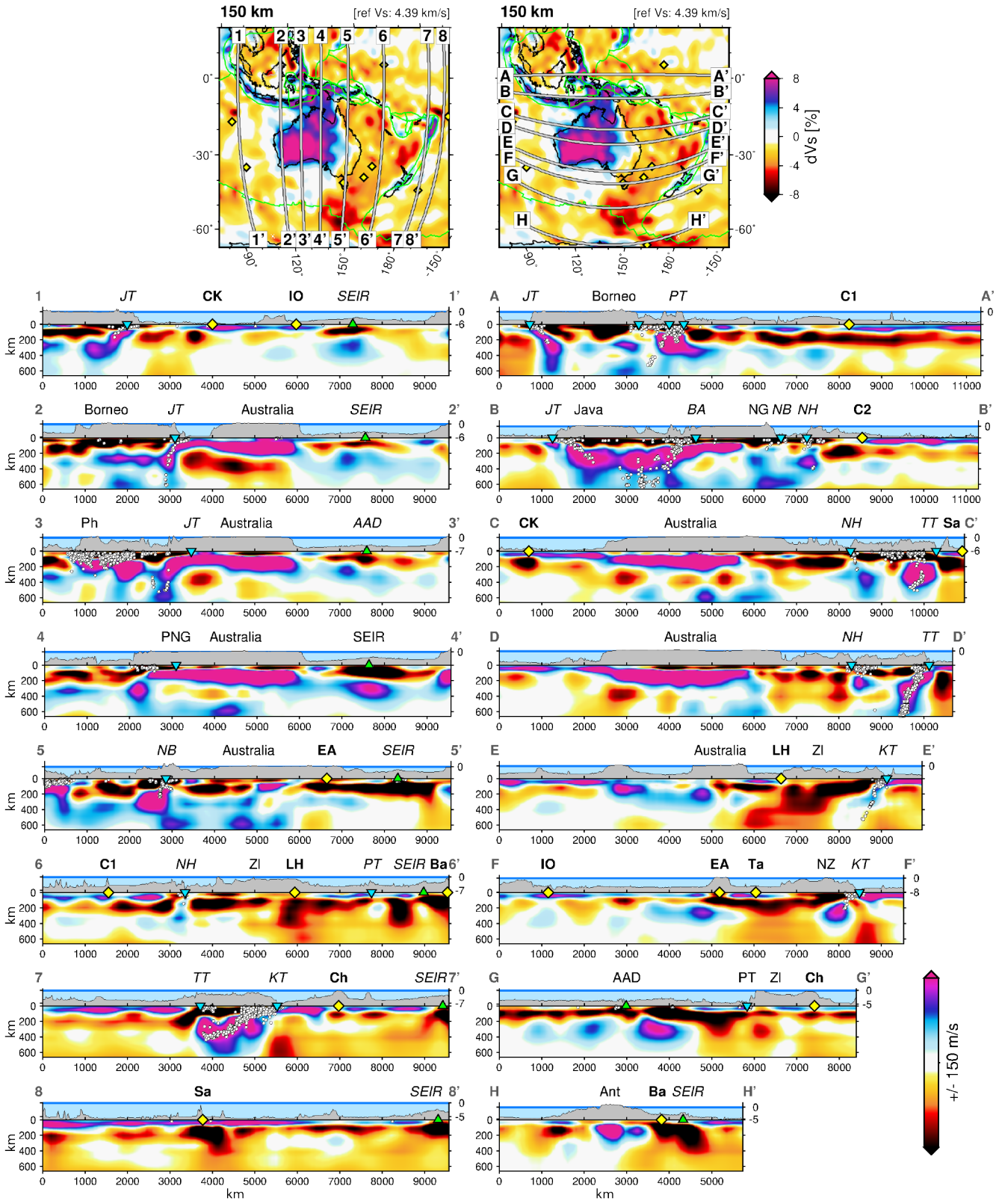

Figure 7. North-south (1-7) and east-west (A-G) cross-sections through the model. Hotspots are shown as yellow diamonds on both the map views and the cross-sections. Blue inverted triangles indicate trench locations and green upright triangles mid-ocean ridge locations in the cross-sections. Hotspot name abbreviations (bold text) are as in Fig. 1. AAD= Australian-Antarctic Discordance, JT= Java Trench, KT=Kermadec Trench, NB= New Britain Trench, NG = New Guinea, NH= New Hybrides Trench, PT=Puysegur Trench, SEIR= Southeast Indian Ridge, TT= Tonga Trench. Continents (plain): Ant = Antarctica, NZ=New Zealand, Ph=Philippines, Zl= Zealandia.

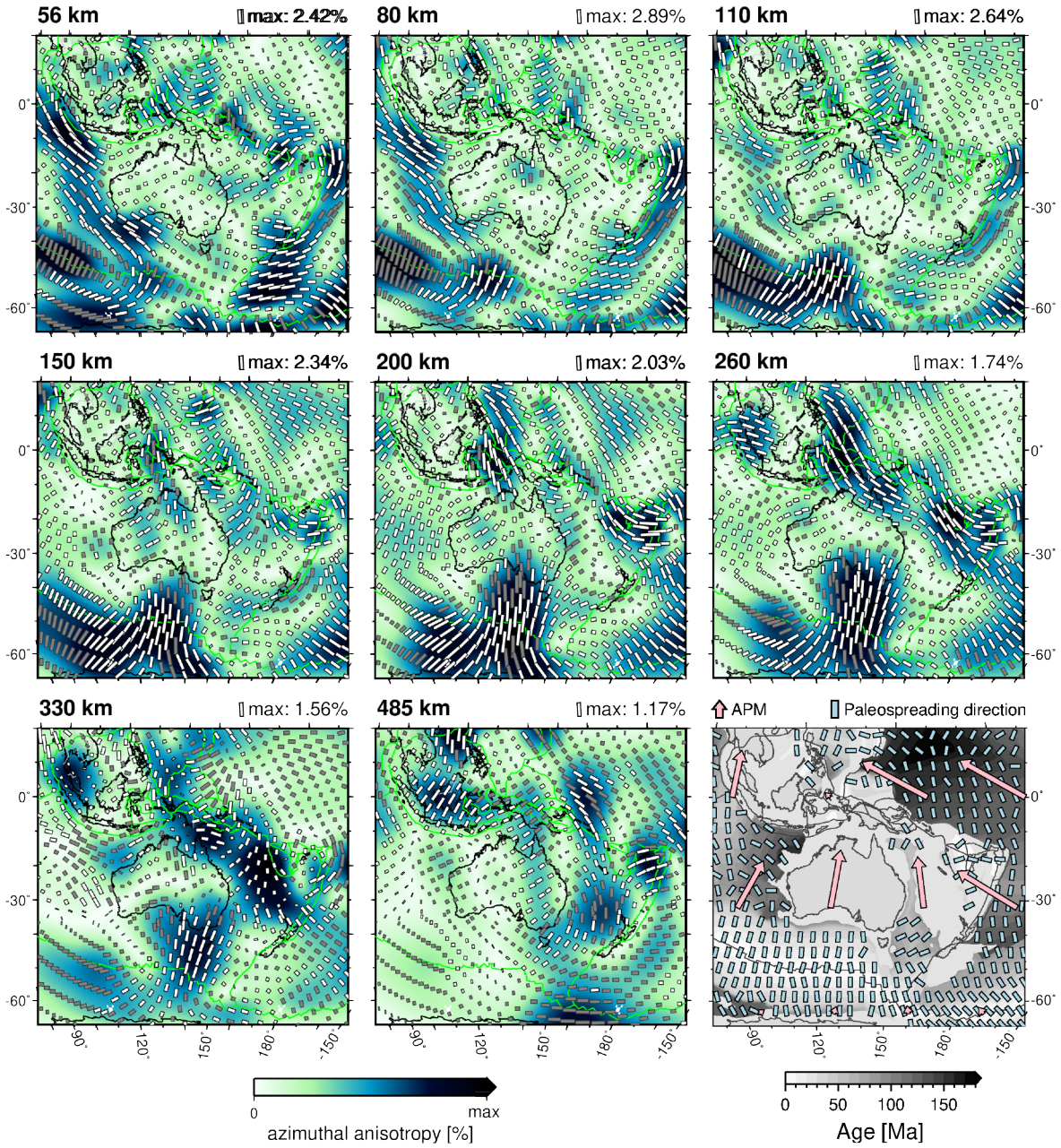

Figure 8. Azimuthal anisotropy according to *Aus22* at 8 different depth slices. The colour scale shows anisotropy amplitude, the orientation of the sticks indicates the fast-propagating direction, and the stick length is proportional to the anisotropy amplitude. The maximum anisotropy at each depth is indicated above each frame. The robust, well-resolved anisotropy, based on the 90-degree resolution tests (Section 4.2), is plotted using white sticks, the unreliable anisotropy is plotted using grey sticks. The input and output fast direction azimuths in these tests are required to be within 25 degrees to be robust. **Bottom right: Seafloor age overlain by the current absolute plate motion (APM) and the paleospreading directions, following Müller et al. (2008).**

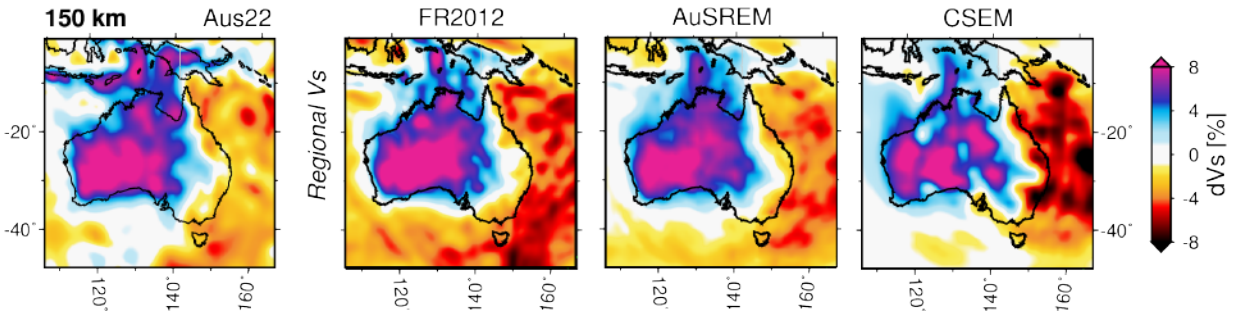

Figure 9. Comparison of *Aus22* to three regional S-wave models of Australia at 150 km depth: FR2012 (Fishwick & Rawlinson 2012), AuSREM (Kennett et al. 2013) and CSEM (Fichtner et al. 2010).

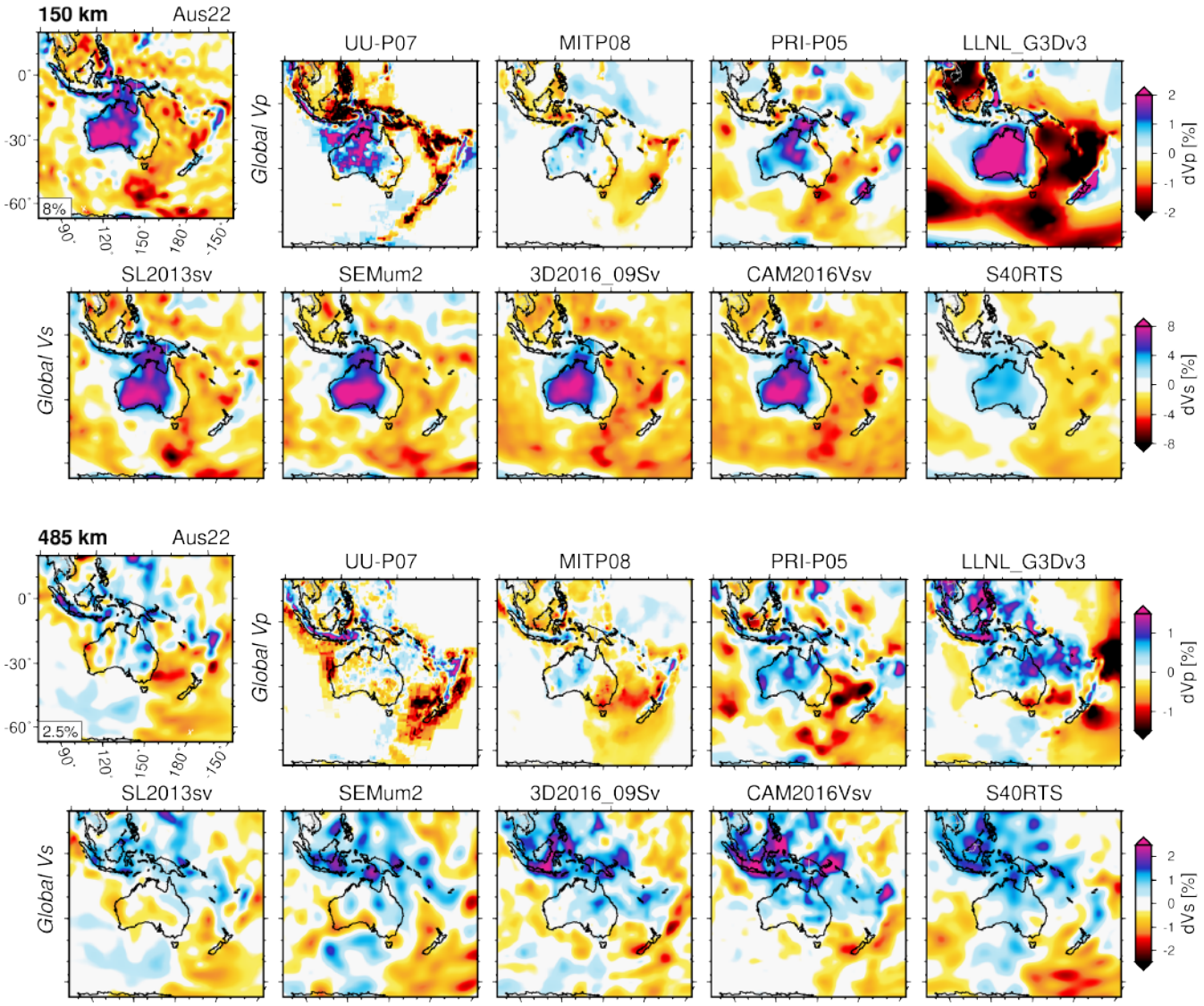

Figure 10. Comparison of *Aus22* to four global S- and 4 global P-wave models at 150 and 485 km depth: SL2013sv (Schaeffer & Lebedev 2013), 3D2016_09Sv (Debayle et al. 2016), SEMum2 (French & Romanowicz 2014), S40RTS (Ritsema et al. 2011), UU-P07 (Amaru 2007), MITP08 (Li et al. 2008), PRI-P05 (Montelli et al. 2006) and LLNL_G3Dv3 (Simmons et al. 2012).

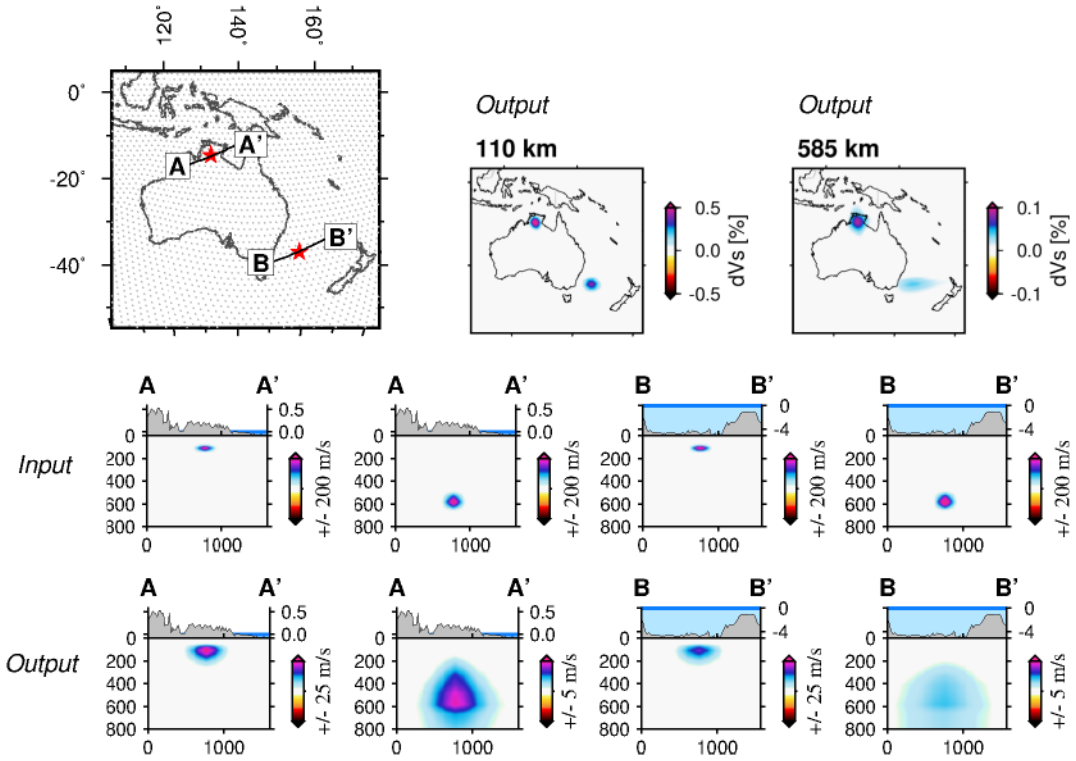

Figure 11. Two spike resolution tests at different depths, with two spike anomalies in each. Top left: the positions of spikes (triangles) on the inversion grid (grey dots). The locations of the cross-sections are indicated. Top middle, top right: the output of the spike tests at the depths of the input, 110 and 585 km. Top row of the cross-sections: the input anomalies; bottom row: the output anomalies. Note the variations in the colour scale limits.

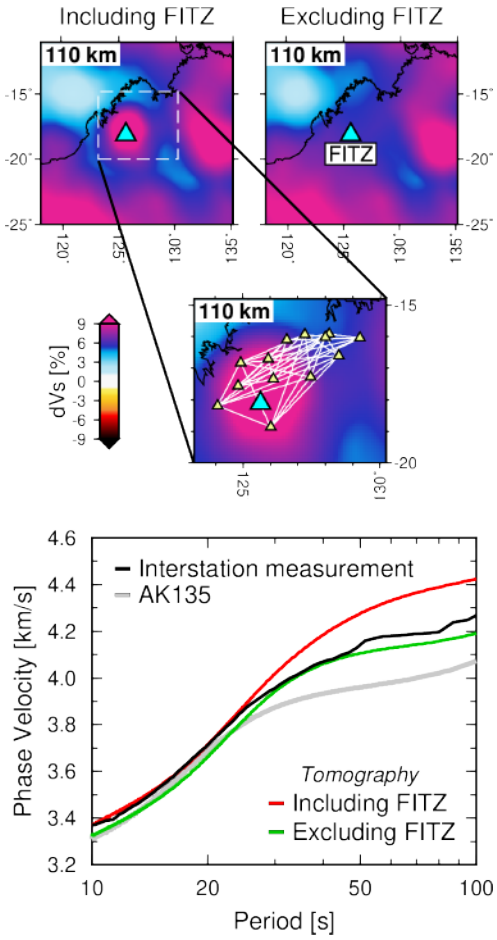

Figure 12. Tests with independent measurements that confirm the intermediate thickness of the lithosphere beneath the Kimberley Craton and demonstrate that the data from the station FITZ cause bias and need to be removed from the dataset. Top: versions of the tomographic model at 110 km depth when including (left) and excluding (right) the data from the station FITZ (blue triangle). The zoom-in map (middle) shows the stations used in the interstation measurements (yellow triangles) and the inter-station paths (white lines). Bottom: the phase-velocity curve yielded by the array measurements (black) is consistent with the curve obtained from the tomographic model computed without the data from the station FITZ (green) and inconsistent with the model computed with the FITZ data (red). Grey line: the phase-velocity curve computed for the reference model AK135 (Kennett et al. 1995).

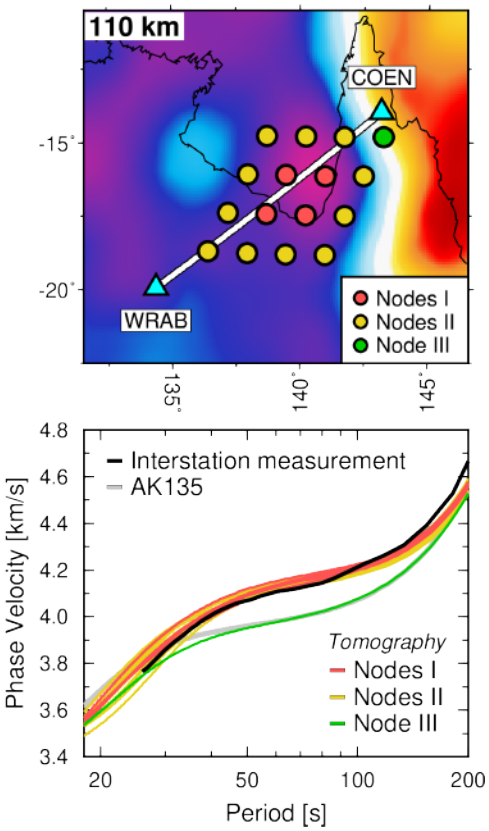

Figure 13. Tests with independent measurements that confirm the presence of high-velocity, cratonic lithosphere beneath the Gulf of Carpentaria area. Top: Our tomography model at 110 km depth below NE Australia. Light blue triangles show the locations of the stations COEN and WRAB, the white line the interstation path, and the coloured circles the grid-knot locations where phase-velocity curves were calculated from our tomographic model. Bottom: The mean phase velocity curve computed using COEN-WRAB interstation measurements (black) is consistent with and confirms the high phase velocities across the Gulf of Carpentaria area. Grey line: the phase-velocity curve computed for the reference model AK135 (Kennett et al. 1995).

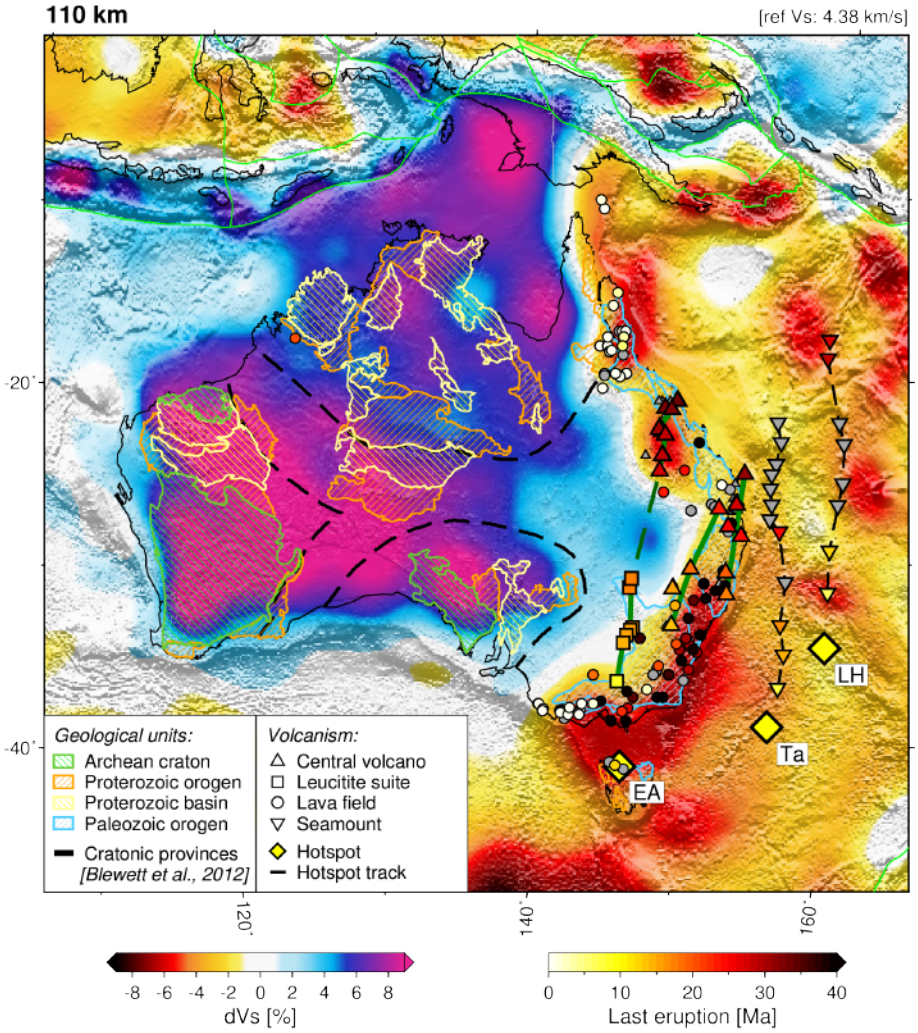

Figure 14. *Aus22* at 110 km depth, overlain by the main geological provinces of the Australian continent, proposed hotspot locations (yellow diamonds) and Cenozoic volcanism locations. Volcanic ages are compiled from the GEOROC and PETLAB databases (Cohen et al. 2008; Knesel et al. 2008; Sutherland et al. 2012). Proposed hotspot tracks are marked with dashed lines, including the Cosgrove Track (Davies et al. 2015) and two shorter tracks within eastern Australia, as proposed by Sutherland et al. (2012). Central volcanoes are marked with triangles, leucitite suits with squares, lava fields with circles and offshore seamounts with inverted triangles. The Cenozoic volcanism age is that of the last eruption. Undated volcanic areas are plotted in grey. Tectonic boundaries as in Fig. 2 are plotted in green, yellow and orange.

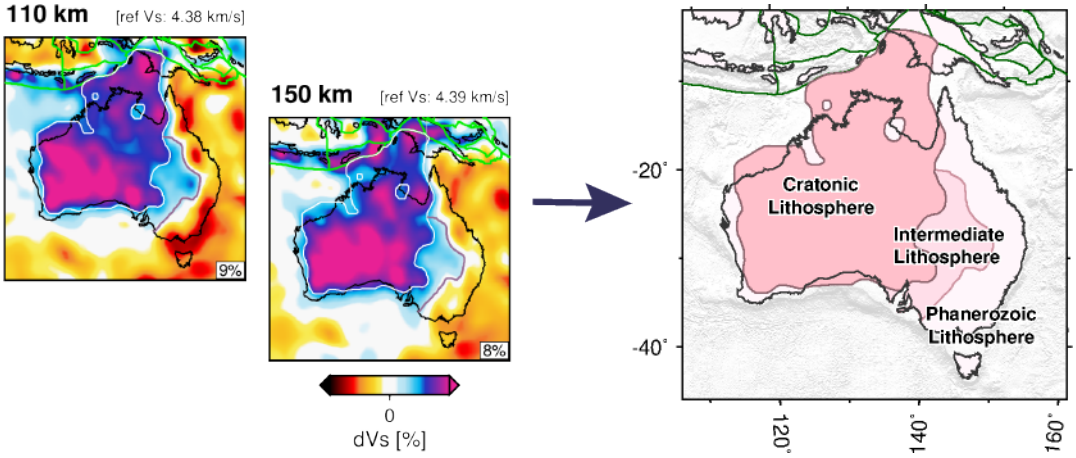

Figure 15. The lateral extent of the Australian cratonic lithosphere. Left: *Aus22* at 110 and 150 km depth. Right: Boundaries of the three types of lithosphere below Australia, mapped using the new tomography (Section 5.1.1): cratonic, intermediate, and Phanerozoic lithosphere. These same boundaries are also plotted on the tomography map views (left).

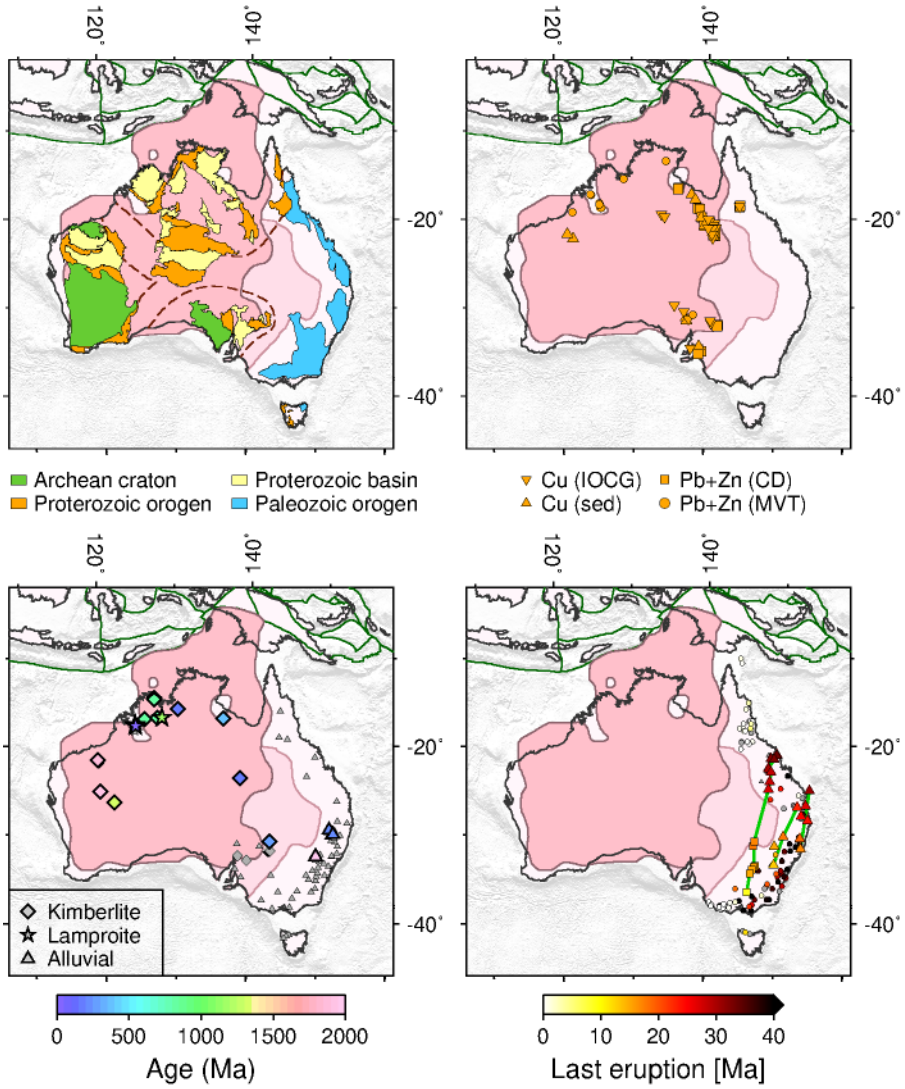

Figure 16. Maps of the three types of the lithosphere of Australia compared with other data. Top left: the main recognised Archean, Proterozoic and Paleozoic crustal blocks (Fig. 2). Top right: sediment-hosted metal deposits (Hoggard et al. 2020). Bottom right: intraplate basaltic volcanism. Bottom left: diamondiferous kimberlites. Diamondiferous kimberlites with an unknown age are plotted in grey.

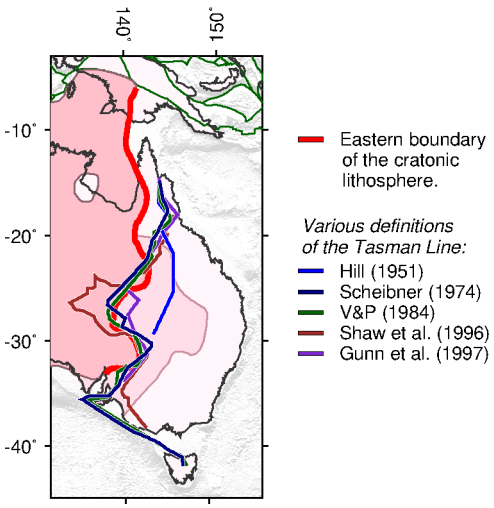

Figure 17. The deep-lithospheric definition of the Tasman Line given by *Aus22* (red), compared with previous definitions based on geological and geophysical data. V & P: Veevers & Powel (1984).

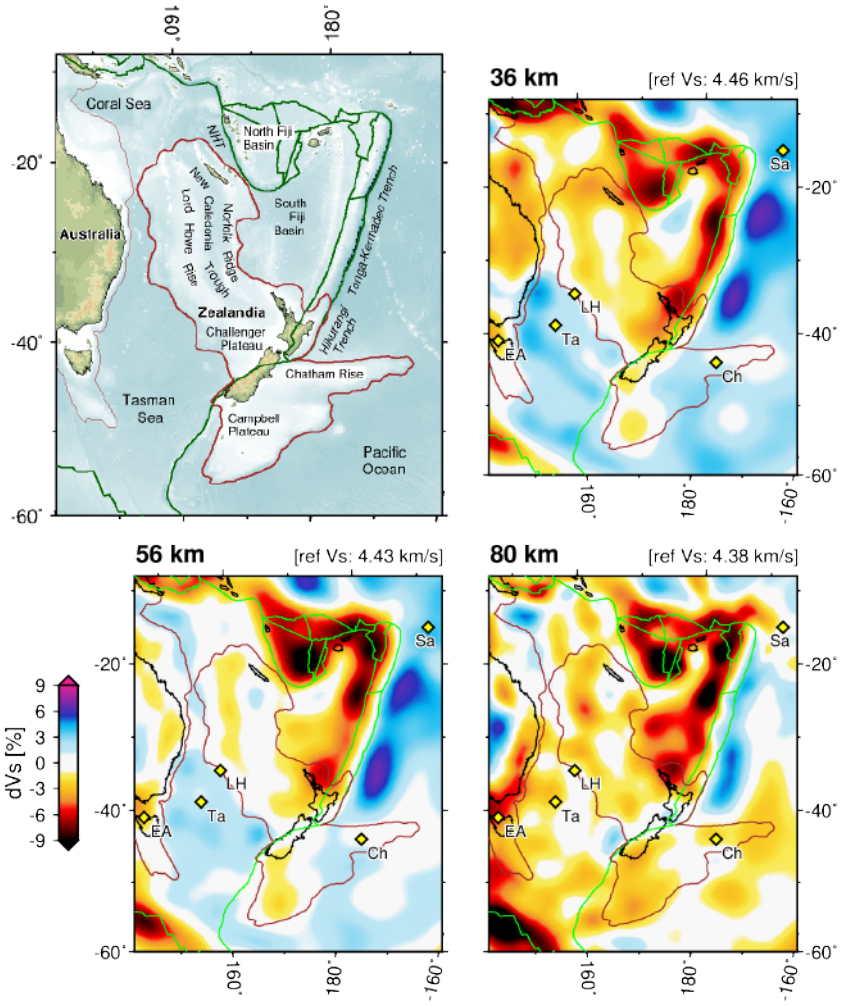

Figure 18. The lithosphere of the continent Zealandia. The outline of Zealandia with bathymetry and the names of the main geological features (top left) and *Aus22* at 36-80 km depth. NHT = New Hebrides Trench. Hotspots are labelled as: EA = East Australia, Ch = Chatam, LH = Lord Howe, S = Samoa, Ta = Tasmantid

APPENDIX A: COMPARISON TO PREVIOUS TOMOGRAPHIC MODELS

A1 Regional models

Figure A1 compares the tomography of *Aus22* with three regional models of Australia at 50-350 km depths: FR2012 (Fishwick & Rawlinson 2012), AuSREM (Kennett et al. 2013) and CSEM (Fichtner et al. 2010).

A2 Global S-Models

Figure A2 and A3 compare the tomography of *Aus22* (top row) with five global S-wave models at 50-250 km and 300-550 km depths, respectively: SL2013sv (Schaeffer & Lebedev 2013), 3D2016_09Sv (Debayle et al. 2016), CAM2016Vsv **(Priestley et al. 2018)**, SEMum2 (French & Romanowicz 2014), S40RTS (Ritsema et al. 2011).

A3 Global P-Models

Figure A4 and A5 compare the tomography of *Aus22* (top row) with four global P-wave models at 50-250 km and 300-550 km depths, respectively: UU-P07 (Amaru 2007), MITP08 (Li et al. 2008), PRI-P05 (Montelli et al. 2006) and LLNL_G3Dv3 (Simmons et al. 2012).

APPENDIX B: SPIKE TEST TRANSITION ZONE TASMAN SEA

Figure A6 shows the result of two spike resolution tests at 585 km depth. See section 4.1 for the method of the spike test.

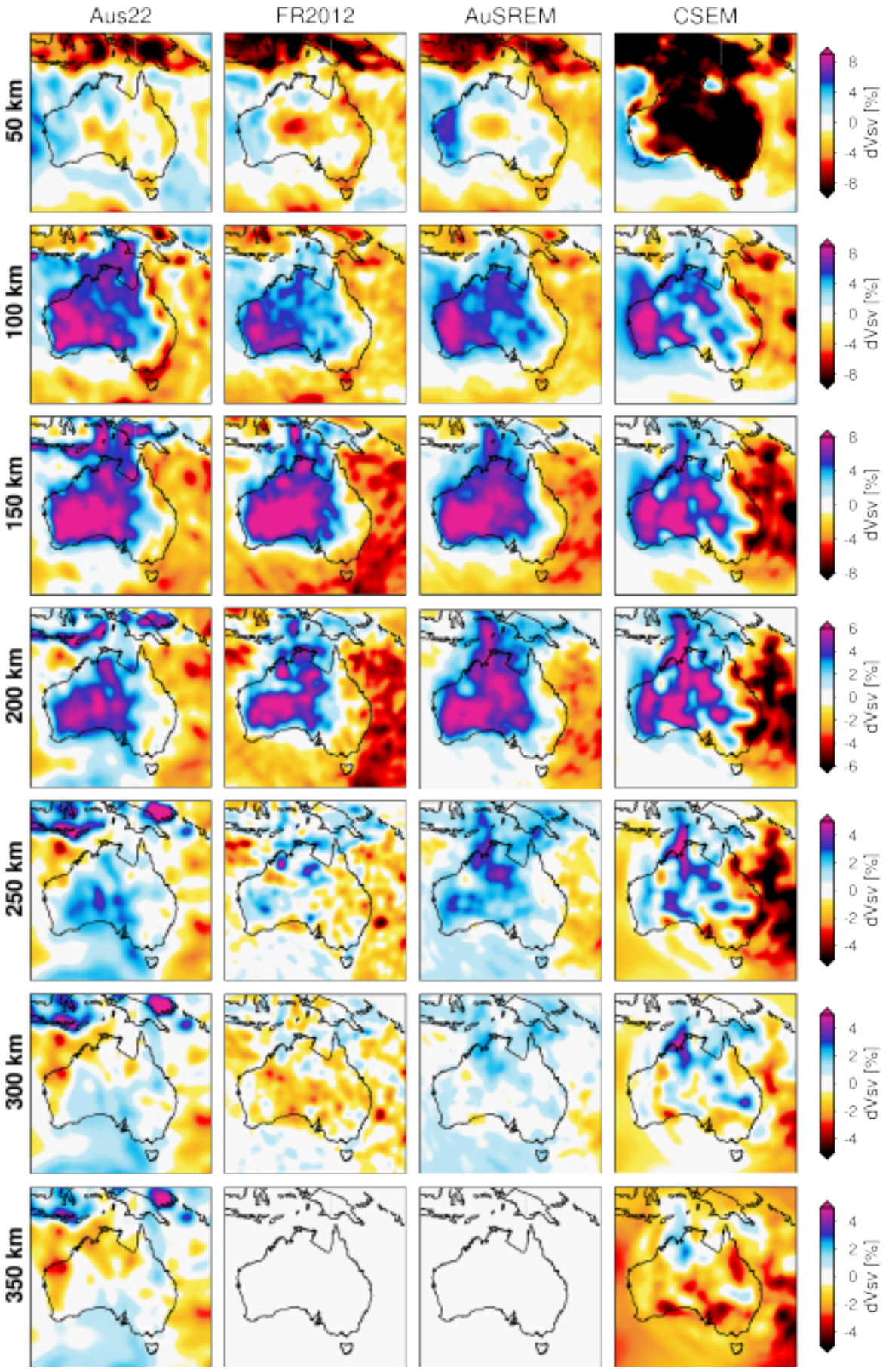

Figure A1. Comparison of *Aus22* with three regional models of Australia at 50-350 km depths: FR2012 (Fishwick & Rawlinson 2012), AuSREM (Kennett et al. 2013) and CSEM (Fichtner et al. 2010).

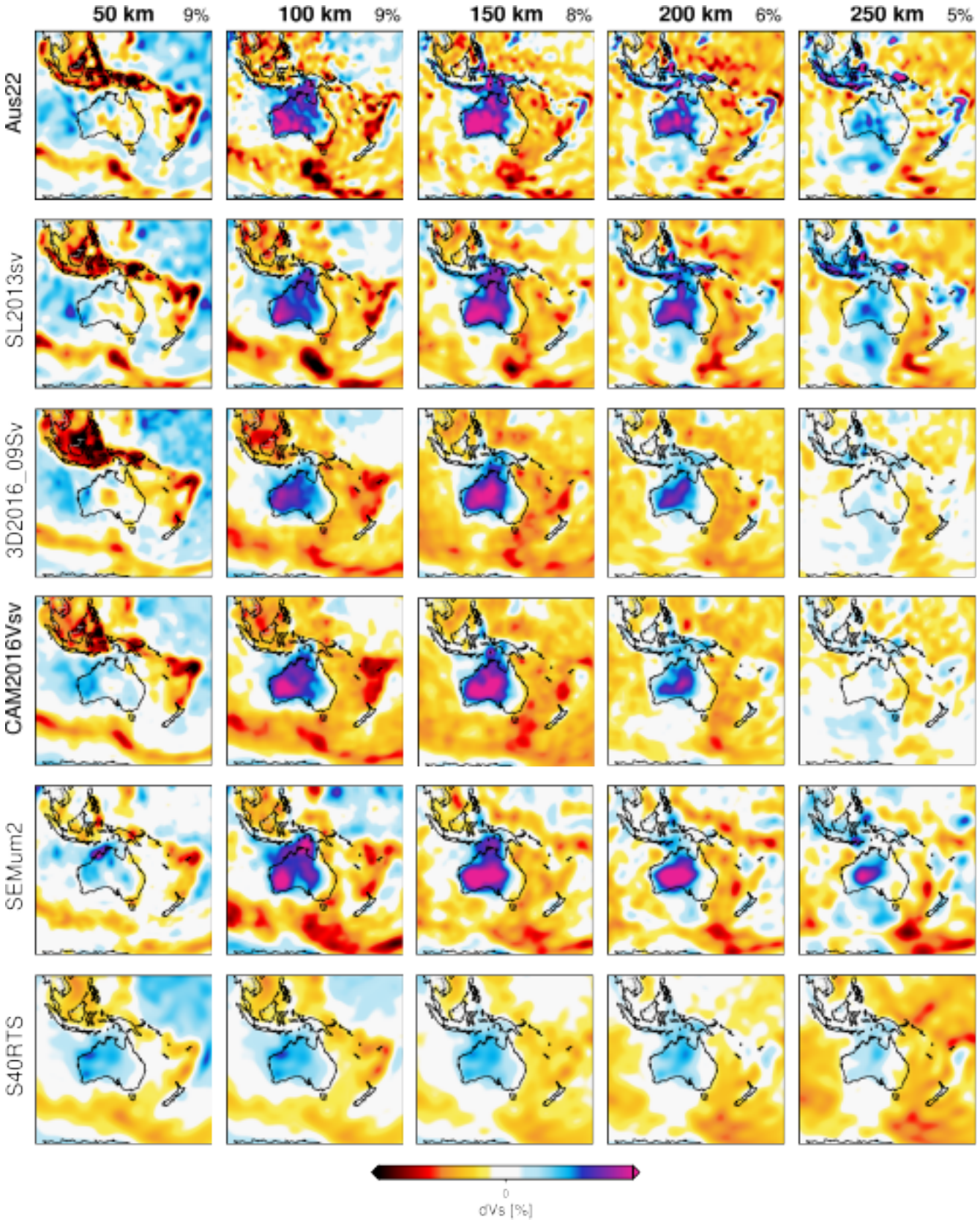

Figure A2. Comparison of *Aus22* (top row) with five global S-wave models at 50-250 km depths: SL2013sv (Schaeffer & Lebedev 2013), 3D2016_09Sv (Debayle et al. 2016), CAM2016Vsv (Priestley et al. 2018), SEMum2 (French & Romanowicz 2014), S40RTS (Ritsema et al. 2011). The colour scale limits change with depth and are specified at the top right corner of each column

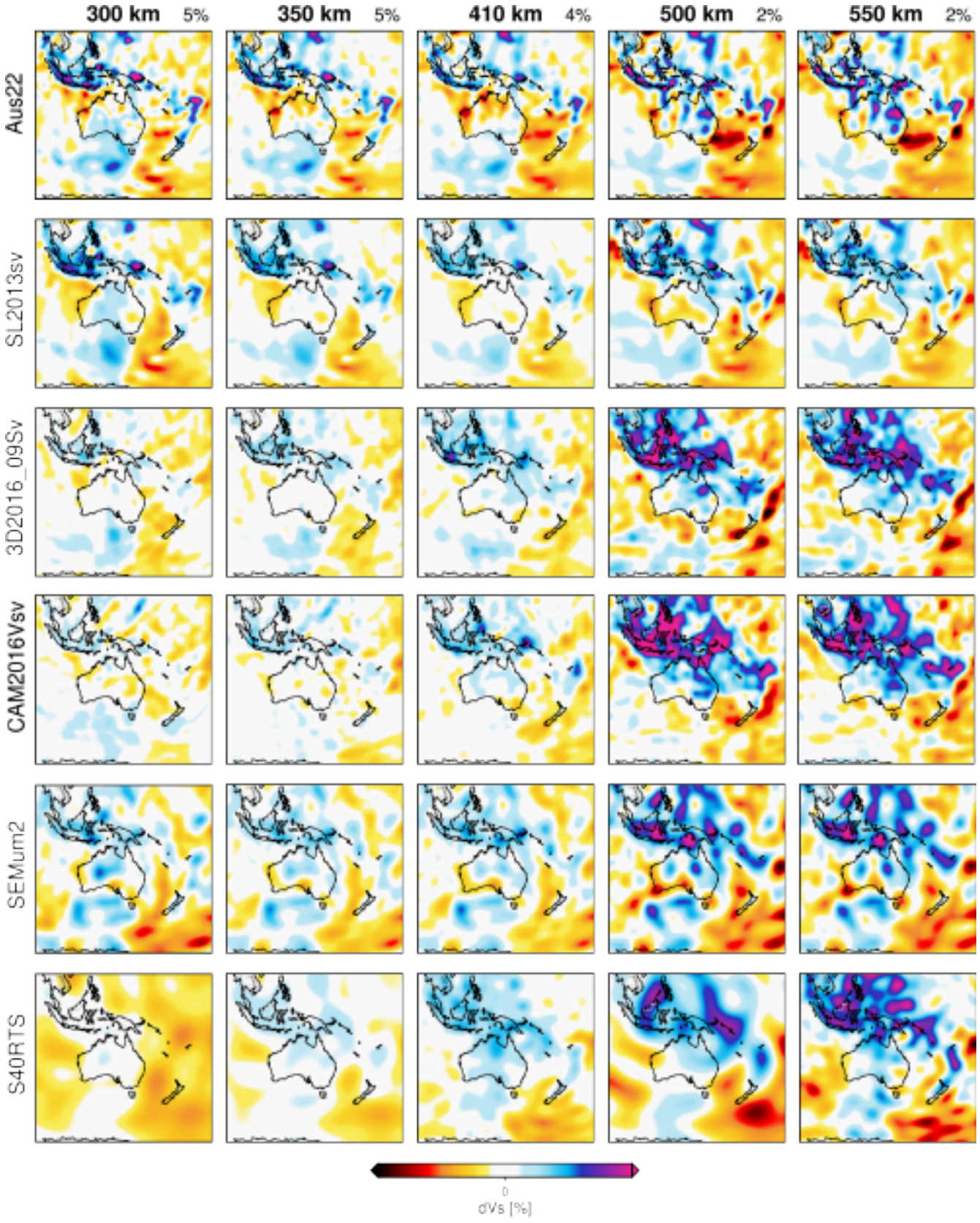

Figure A3. Comparison of *Aus22* (top row) with five global S-wave models at 300-550 km depths: SL2013sv (Schaeffer & Lebedev 2013), 3D2016_09Sv (Debayle et al. 2016), CAM2016Vsv **(Priestley et al. 2018)**, SEMum2 (French & Romanowicz 2014), S40RTS (Ritsema et al. 2011).]The colour scale limits change with depth and are specified at the top right corner of each column.

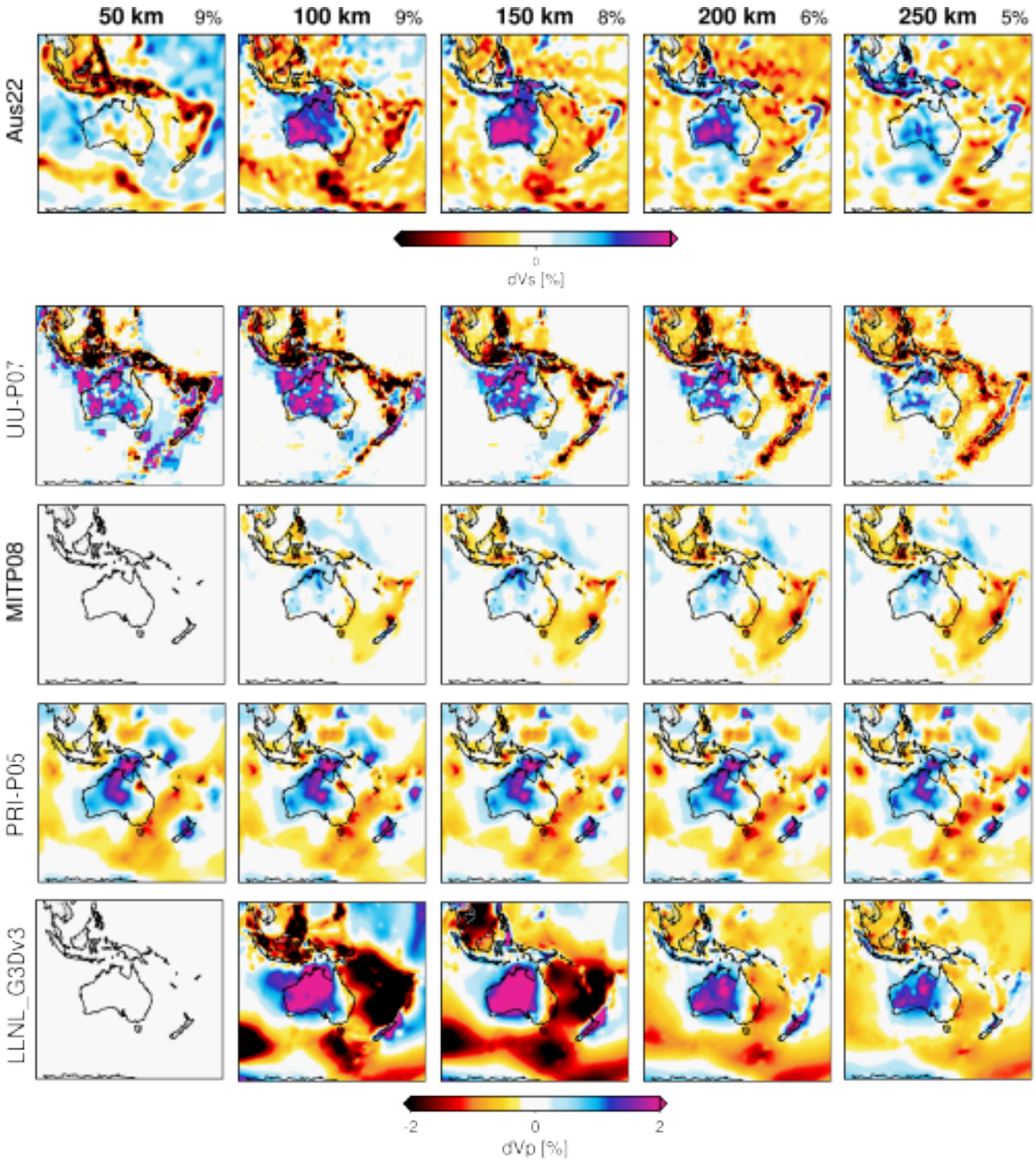

Figure A4. Comparison of *Aus22* (top row) with four global P-wave models at 50-250 km depths: UU-P07 (Amaru 2007), MITP08 (Li et al. 2008), PRI-P05 (Montelli et al. 2006) and LLNL_G3Dv3 (Simmons et al. 2012). The colour scale limits for *Aus22* change with depth and are specified at the top right corner of each frame.

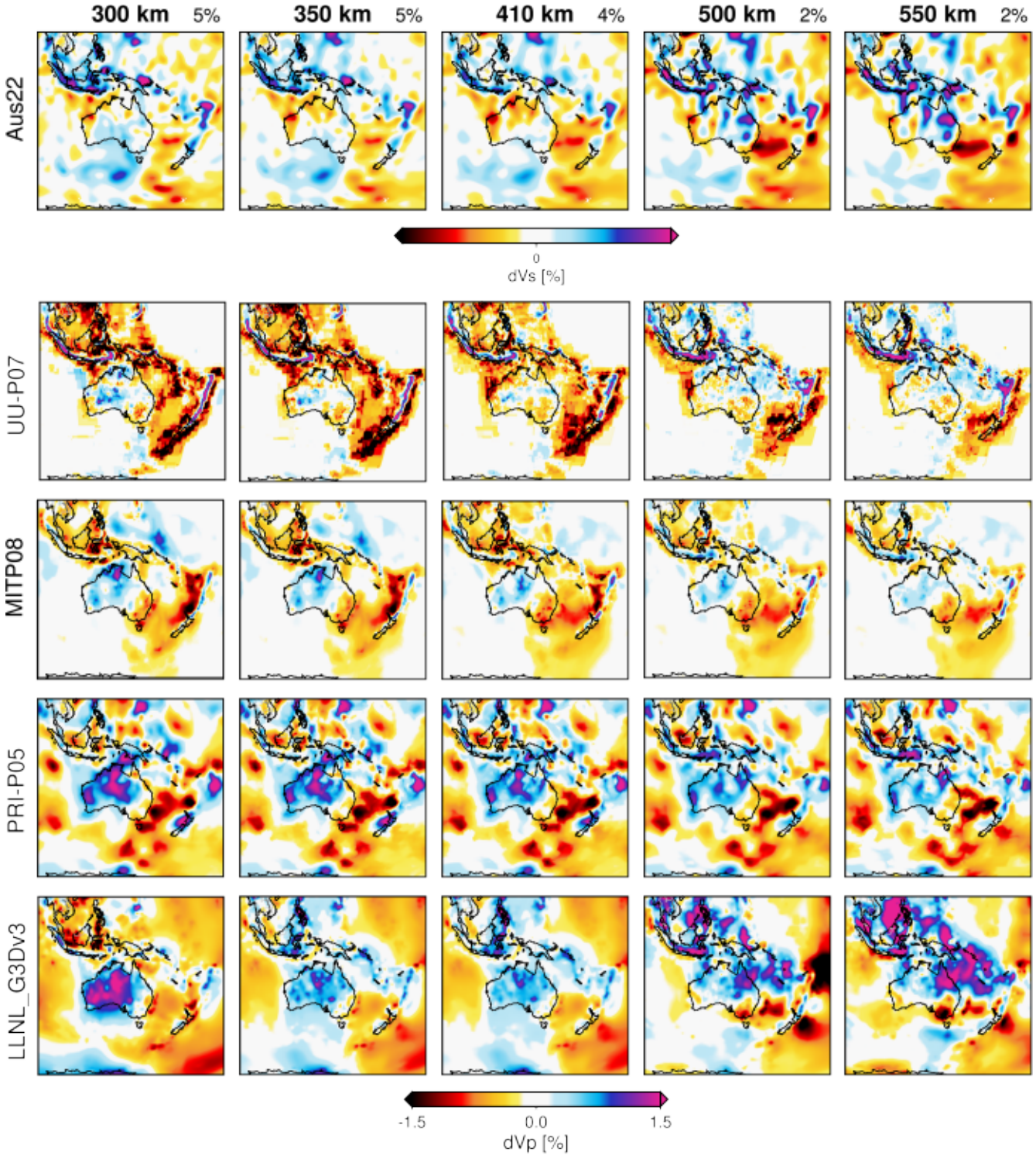

Figure A5. Comparison of *Aus22* (top row) with four global P-wave models at 300-550 km depths: UU-P07 (Amaru 2007), MITP08 (Li et al. 2008), PRI-P05 (Montelli et al. 2006) and LLNL_G3Dv3 (Simmons et al. 2012). The colour scale limits for *Aus22* change with depth and are specified at the top right corner of each frame.

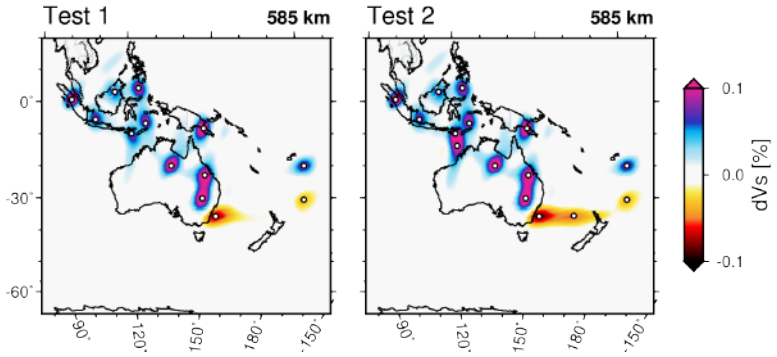

Figure A6. Two spike resolution tests at 585km depth. White dots: location of input spikes with S-velocity anomaly of $\pm$ 300 m/s. S-wave velocity anomalies that are the output of the spike tests are plotted behind the white dots. The positive and negative velocity anomalies are the result of a positive and negative S-velocity input spike, respectively. Test 2 (right) includes two more spikes than Test 1 (left). The details of the method of the spike test are given in section 4.1. Note the variation in amplitude and smearing of the seismic velocity anomaly in the output of the spike test per location.